

Elastic Properties of Carbon Nanomembranes and Graphene: Theory and Experiment

Dissertation

**Faculty of Physics
Bielefeld University**

**submitted by
Florian Paneff**

Bielefeld, September 7, 2021

Committee

**Prof. Dr. Armin Gölzhäuser
Prof. Dr. Jürgen Schnack**

Contents

1. Introduction	5
2. Carbon Nanomembranes (CNMs)	7
2.1. Self Assembled Monolayers (SAMs)	7
2.2. Electron Induced Cross Linking and CNMs	7
3. Theory of Bulge Test and Nanoindentation	11
3.1. Elastic Testing of 2D Materials	11
3.2. Stress and Strain	12
3.3. Bulge Test and Nanoindentation	14
3.4. Bulge Test Theory	17
3.4.1. Overview of Common Descriptions of a Pressurized Membrane	18
3.4.2. Small and Large Deflection Limit of a Uniformly Pressurized Membrane	20
3.4.3. Beams's Model to Describe the Bulge Test	21
3.4.4. Hencky's Solution for the Large Deflection Limit	23
3.4.5. Behavior of a Membrane with Initial Tension in the Intermediate Regime	27
3.4.6. Impact of the Assumption of a Uniformly Lateral Load	33
3.4.7. The Influence of Finite Strains	35
3.4.8. The Influence of Bending Stiffness	37
3.4.9. Conclusions	38

3.5. Nanoindentation Theory	41
3.5.1. Large Deflection Limit	43
3.5.2. Small Deflection Limit	47
3.5.3. Intermediate Range	48
3.5.4. Conclusions	49
3.6. 2D modulus	52
4. Methods	55
4.1. Atomic Force Microscopy (AFM)	55
4.1.1. Force Curve	57
4.1.2. AFM Bulge Test and Nanoindentation	57
4.2. Helium Ion Microscopy (HIM)	57
4.3. X-ray Photoelectron Spectroscopy (XPS)	59
4.4. Sader Method for the Determination of the Spring Constant of the Cantilever	60
5. Experimental	63
5.1. Sample Preparation	63
5.1.1. SAM Preparation	63
5.1.2. Electron Irradiation	63
5.1.3. Sample Transfer	64
5.1.4. Critical Point Drying	65
5.1.5. CVD Graphene	65
5.2. Execution of Bulge Test and Nanoindentation	67
5.2.1. Cantilever Choice	67
5.2.2. Substrate and Optimal Membrane Diameter	68
5.2.3. Experimental Setup	69
5.2.4. Determination of the Central Point of the Membrane	69
5.2.5. Execution of the Bulge Test Experiment	71
5.2.6. Execution of the Nanoindentation Experiment	73

5.2.7. Data Analysis	75
6. Results	79
6.1. Determination of the AFM Tip Radius	79
6.1.1. Calibration Measurements on CVD Graphene	81
6.1.2. Quantitative Analysis and Discussion	85
6.2. 2D Modulus and Young's Modulus of Different CNMs	88
6.2.1. TPT	88
6.2.2. ODT	91
6.2.3. Pyrolyzed TPT	97
6.2.4. PVBP and Pyrolyzed PVBP	99
6.3. Initial Tension	101
6.4. Uncertainty Estimation	105
6.4.1. Bulge Test	105
6.4.2. Nanoindentation	108
6.5. Summary of all Materials	110
7. Conclusions of the Thesis	115
8. Bibliography	119
Declaration of academic honesty	129
A. Mathematica Source Code for the Bulge Test Theory	I

Table 0.1.: List of abbreviations

AFM	Atomic Force Microscope
BPT	1,1'-Biphenyl-4-thiol
CNM	Carbon Nanomembrane
CVD	Chemical Vapor Deposition
DMF	N,N-dimethylformamide
HIM	Helium Ion Microscopy
ODT	1-Octadecanethiol
PDMS	Polydimethylsiloxane
PMMA	Polymethyl methacrylate
PVBP	Polyvinylbiphenyl
SAM	Self Assembled Monolayer
SPM	Scanning Probe Microscopy
STIM	Scanning Transmission Ion Microscopy
TPT	1,1',4',1''-Terphenyl-4-thiol
UHV	Ultra High Vacuum
XPS	X-ray Photoelectron Spectroscopy

Table 0.2.: List of symbols

Pressure	p
Force	F
Membrane radius	r
Membrane thinckness	t
Deflection height	h
Stress (general)	σ_{ij}
Normal stress	$\sigma_i := \sigma_{ii}$
Shear stress	τ_{ij}
Strain	ϵ_{ij}
Young's modulus	E
Initial tension	σ_0
2D Young's modulus	E_{2D}
2D initial tension	σ_{2D}^0
Poisson's ratio	ν
Bulge Test constants	C_1, C_2
Hencky's constant	$K(\nu) = C_2/(1 - \nu)$
Reformulated pressure	$k = \frac{1}{4} (Ep^2(r/t)^2)^{1/3}$
Dimensionless loading parameter	$q = pr/(Et)$
Dimensionless force	$\tilde{F} = E^{1/2}F / (\sigma_0^{3/2}tr)$
Dimensionless deflection	$\tilde{\delta} = h/r \cdot (E/\sigma_0)^{1/2}$
Indenter radius	r_{indenter}
Relative indenter size	$\rho_{\text{in}} = r_{\text{indenter}}/r$
Nanoindentation prefactor	$\alpha(\nu) = 0.867 + 0.2773\nu + 0.805\nu^2$
Tip correction factor	$\alpha_{\text{tip}} = (1 - \rho_{\text{in}}^{2/3})^{-3}$

1. Introduction

The discovery of graphene [1] by K. S. Novoselov and A. K. Geim in 2004 caused a great interest in the relatively new area of 2D materials, i.e. materials which consist of only one molecular layer. By now, a variety of different 2D materials can be routinely fabricated, for example hexagonal boron nitride (hBN) [2] or carbon nanomembranes (CNMs) [3]. Each of these materials possesses an individual structure and therefore exhibits unique properties. However, the most remarkable property of all these materials is the high stability despite the thickness of only one molecular layer. This enables their use in many possible applications such as filtration processes [4, 5] or capacitors [6, 7].

The existence of these new 2D materials raises the question of their mechanical properties and in particular their elastic properties [8]. These characteristics are crucial for the understanding of the material but also for applications for example in the construction of devices. The most prominent elastic property of a material is its Young's modulus. It describes the relationship of stress and strain within the material and has a broad range of applications. For example, the knowledge of the Young's modulus is needed to calculate how much an antenna or a membrane bends when exposed to an outer force. Therefore, the determination of the Young's modulus is a very important task. However, it is not easy to conduct experiments which precisely determine the Young's modulus. This is even more challenging when it comes to 2D materials such as CNMs or graphene since they cannot easily be stretched or compressed. Nevertheless, by now there are well known techniques to investigate the elastic properties of 2D materials.

This thesis is dedicated to the determination of the elastic properties of various kinds of CNMs with two of these methods, Bulge Test [9] and nanoindentation [10]. The focus of the work is twofold. On the one hand, the Young's modulus of the CNMs and its dependence on their different properties are of interest. On the other hand, the two methods, Bulge Test and nanoindentation, shall be objects of research as well. This applies to their theoretical description as well as their experimental conduction.

The thesis divided into two main parts. After a brief introduction of CNMs, the theoretical part of the thesis in chapter 3 covers the mathematical description of Bulge Test and nanoindentation. An analytic model of the Bulge Test is derived which is based on works of H. Hencky [11] and R. J. Hohlfelder [12] and the accuracy of the model is estimated. The nanoindentation experiment is described following D. Vella and B. Davidovitch [13]. The accuracy of the model under the conditions of the experiments in the present work is estimated.

The experimental part of the thesis covers the conduction and the results of the experiments. In chapter 5, a procedure how Bulge Test and nanoindentation can be executed consecutively in one experiment is described. This approach allows to gather and to compare the results of both experiments in a time-saving manner. Since the determination of the elastic properties of a material has to deal with significant uncertainties, the comparison of the two different methods provides valuable additional information. In chapter 6, the results of the experiments are presented. Different kinds of CNMs were investigated, for instance the new materials ODT and PVBP as well as nanocrystalline graphene.

The conclusions of the thesis are given in chapter 7.

2. Carbon Nanomembranes (CNMs)

2.1. Self Assembled Monolayers (SAMs)

Self-assembly is the spontaneous organization of individual molecules into a highly ordered structure [14]. The molecules which form the SAM are called precursor molecules, which consist of a ligand and a spacer. The chemical properties of the SAM are defined by the terminal functional group. The SAM is formed on the surface of a substrate, for instance a metal. The choice of the substrate may influence the structure of the SAM. SAMs for the formation of CNMs are usually grown on a gold substrate. The standard precursor molecules are aromatic thiols, i.e. the spacer consists of phenyl rings and the ligand is a sulfur atom since the Au-S binding energy is very high, approximately 50 kcal/mol [15]. SAMs are formed through adsorption on the substrate. This adsorption may be either from solution or from gas phase. A schematic diagram of an idealized SAM is shown in figure 2.1.

2.2. Electron Induced Cross Linking and CNMs

SAMs with aromatic precursor molecules can be cross-linked to form a connected network by irradiation with low energy electrons (usually 100eV). This effect was already utilized in 2000, when Götzhäuser et al. reported that SAMs from aromatic and aliphatic thiols can be used as a negative respectively positive electron beam resist [16]. The connected network is mechanically stable and can be transferred onto a holey substrate in order to form a freestand-

2. Carbon Nanomembranes (CNMs)

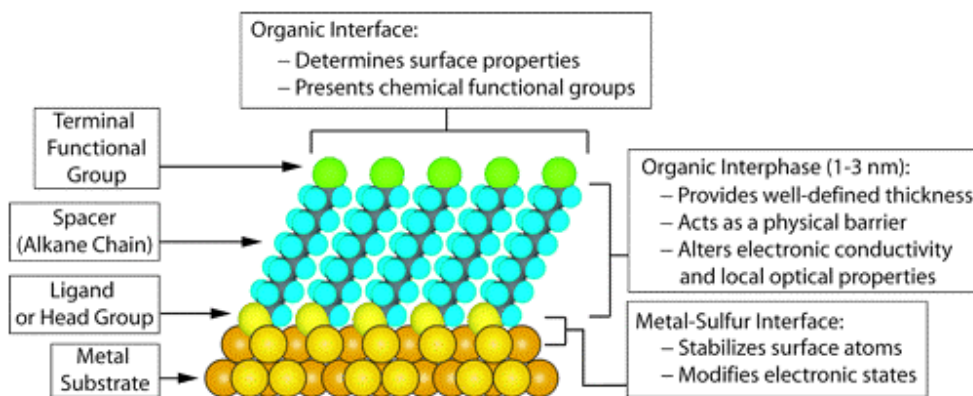


Figure 2.1.: Schematic diagram of an aliphatic SAM on Au(111) [15]. Reproduced with permission.

ing membrane which is called Carbon Nanomembrane (CNM) [17, 18]. The fabrication process of a CNM is schematically shown in figure 2.2.

CNMs can be formed from various precursor molecules [3]. Frequently used precursor molecules are for instance 1,1'-Biphenyl-4-thiol (BPT) and 1,1',4',1''-Terphenyl-4-thiol (TPT). The molecular structure of BPT and TPT is shown in

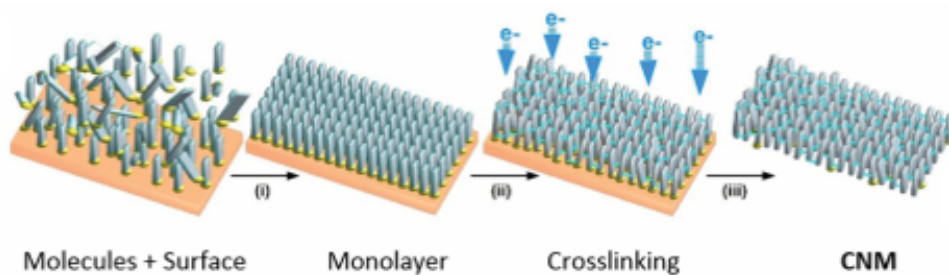


Figure 2.2.: Schematic diagram of the fabrication of a CNM [3]. Reproduced with permission.

figure 2.3. The precursor molecule defines the properties of the CNM. Through the choice of the functional end group, CNMs can be chemically functionalized [19].

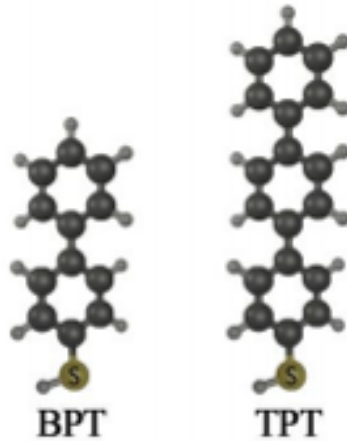


Figure 2.3.: Molecular structure of BPT and TPT. Carbon atoms are black, hydrogen atoms are grey and sulfur is displayed in yellow [20]. Reproduced with permission.

CNMs have a high potential for possible applications. They can serve as a molecular sieve for water and gas separation processes [4, 21, 22]. Moreover, through annealing, CNMs can be transformed into nanocrystalline graphene [23] which can be used for capacitors that exclusively consist of carbon [7].

More details about the properties of CNMs and their applications can be found in the review papers by A. Turchanin and A. Götzhäuser [3, 24].

3. Theory of Bulge Test and Nanoindentation

3.1. Elastic Testing of 2D Materials

There are various methods for the investigation of the elastic properties of thin films. Some of these techniques require a supported membrane, for instance the classical nanoindentation with a nanoindenter [25]. Others require a freestanding membrane, for example the Bulge Test [26] or nanoindentation on freestanding membranes which is sometimes referred to as point deflection method [27]. When it comes to the examination of 2D materials, experiments with a supported specimen face the difficulty that due to the molecular thinness of the membrane, an interaction with the supporting substrate is hard to avoid. Therefore, experiments on freestanding membranes are favorable.

A typical technique for the investigation of 2D materials is to subject the membrane to a force that acts out-of-plane, i.e. perpendicular to the membrane. This out-of-plane force leads to a vertical deflection of the freestanding membrane which in turn causes an in-plane stretching of the membrane. This technique is the working principle of Bulge Test as well as nanoindentation¹.

In this chapter, the concepts of the mechanics of an elastic body which are needed for the description of Bulge Test and nanoindentation are introduced. Subsequently, the pressure-deflection relationship of the Bulge Test and the

¹For the sake of brevity, nanoindentation on a freestanding membrane shall be referred to as nanoindentation in the present work.

force deflection relationship of the nanoindentation experiment which are used to evaluate the experiments in this work are derived.

3.2. Stress and Strain

The concepts of mechanical stress and strain play a very important role in continuum mechanics. Stress is the measure of a force which applies to a cross sectional area of an object. The notion of stress is used in two different contexts [28]. Firstly, it is used to describe an external load which deforms the object. Such kind of force is usually referred to as a "Surface Force". Secondly, it describes the internal forces which appear in an object as a reaction to an external load, usually referred to as a "Body Force". The distribution of the stress within the object does not need to be uniform [29]. For a general description of the stress, the object is imagined to be divided into infinitesimal volume elements. Each of the volume elements has its own stress tensor, since each surface of the volume element is subjected to its individual force. Therefore, in its general form, stress is a tensor-valued function across the object. It is usually denoted by the Greek letter σ and defined as

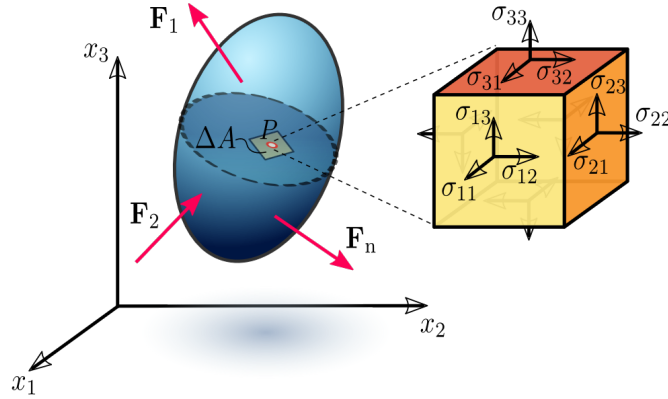


Figure 3.1.: Illustration of the stress in a three dimensional object [30]. Reproduced with permission.

$$\sigma_{ij} = \frac{F_j}{A_i}, \quad (3.1)$$

where the indices i and j denote the spatial directions, as illustrated in figure 3.1. When $i = j$, the stress is called "normal stress". In the case of $i \neq j$, the stress is called "shear stress". In order to distinguish the two kinds of stresses, the shear stress is often denoted by the Greek letter γ instead of σ .

Since external stress causes the deformation of an object, it leads to strain. Strain is the measure of the mechanical deformation. For an object which is only deformed in one dimension, the strain ϵ is defined as

$$\epsilon = \frac{\Delta L}{L}, \quad (3.2)$$

where L is the length of the object and ΔL is the change in length due to the deformation. For a general definition of the strain, the so-called displacement field $u(x)$ is needed.

$$u(x) = x' - x, \quad (3.3)$$

where x is the position of an arbitrary point of the object before the deformation and x' is the position of the same point in the deformed object. Like stress, strain is a tensor-valued function, defined by

$$\epsilon_{ij}(x) = \frac{1}{2} \left(\frac{\partial u_i}{\partial x_j} + \frac{\partial u_j}{\partial x_i} \right). \quad (3.4)$$

For $i = j$, the strain $\epsilon_{ii} = \frac{\partial u_i}{\partial x_i}$ is called normal strain while for $i \neq j$, the strain is called shear strain. The stress tensor as well as the strain tensor are symmetric, i.e.

$$\sigma_{ij}(x) = \sigma_{ji}(x) \text{ and } \epsilon_{ij}(x) = \epsilon_{ji}(x). \quad (3.5)$$

3. Theory of Bulge Test and Nanoindentation

In elastic deformations, the relationship between stress and strain is linear. This relationship is called Hooke's law. The slope of the stress versus strain curve is a material property and is called Young's modulus

$$E = \frac{\sigma}{\epsilon}. \quad (3.6)$$

It shall be noted that the Young's modulus is only defined for uniaxial stresses. Furthermore, it is possible that a material which is not isotropic has different Young's moduli for different directions. Graphite for example has a higher Young's modulus parallel to its layers than perpendicular to the layers. Since it relates stress and strain of an object, the Young's modulus is a very important material property.

When an object is stretched or compressed in x-direction, its size in y- and z-direction is subjected to a change as well. This change is described by the Poisson's ratio ν which is defined as

$$\nu = -\frac{\epsilon_{\text{transversal}}}{\epsilon_{\text{lateral}}} \quad (3.7)$$

The Poisson's ratio of isotropic materials can range from $\nu = -1$ to $\nu = 0.5$. Rubbers exhibit a Poisson's ratio of $\nu = 0.5$ which implies that the material is incompressible. Negative Poisson's ratios seem counterintuitive, but have been demonstrated in the case of foams [31]. The Poisson's ratio of the most common materials such as organics or metals is usually in the range of $\nu = 0.1$ to $\nu = 0.5$ [32, 33].

3.3. Bulge Test and Nanoindentation

In this work, the Young's modulus of thin elastic films is determined independently by Bulge Test and nanoindentation. In the Bulge Test, the membrane is subjected to a pressure difference which causes a deflection of the membrane. In the nanoindentation experiment, the membrane is deflected by a sharp tip, for

example the tip of an atomic force microscope (AFM). AFM-nanoindentation received a lot of attention when it was successfully employed for the experimental determination of the Young's modulus of graphene [34]. Since then, it is the most frequently used method for the determination of the Young's modulus. A schematic diagram of Bulge Test and nanoindentation is shown in figure 3.2.

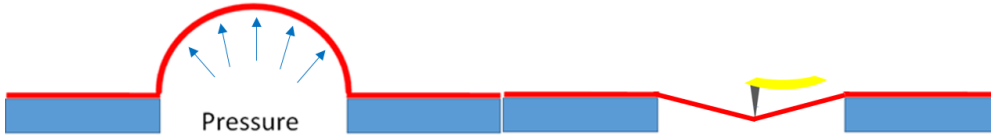


Figure 3.2.: Schematic diagram of a Bulge Test experiment (left) and a nanoindentation experiment (right).

Bulge Test as well as nanoindentation are too complex to be described entirely analytically. Hence there are two ways of gaining theoretical knowledge about these methods. Firstly, with simplifying assumptions which enable an analytic solution and secondly, with the help of finite element simulations. The advantage of the analytic solutions is that they give more insight into the behavior of the system and the influence of single parameters. Simulations on the other hand are able to describe the system more accurately, provided that the experiment is modeled exactly. For a good understanding of the Bulge Test and the nanoindentation, it is therefore helpful to combine both methods and to compare their results. In order to achieve the theoretical results, the following assumptions are needed [35].

Firstly, the membrane is assumed to be homogeneous and isotropic in the x-y-plane. Due to their amorphous state, this assumption is not exactly satisfied for CNMs. However, since the membranes examined in the present work have a radius of several μm and the irregularities occur on a molecular scale, the membrane can be treated as homogeneous. In the case of graphene, the assumption is satisfied.

3. Theory of Bulge Test and Nanoindentation

Secondly, the strain in the pressurized membrane is assumed to be infinitesimal. This assumption states that the physical properties of the membrane, i.e. its Young's modulus, Poisson's ratio and density distribution remain unchanged. However, this assumption is only needed for analytical theories. In simulations, finite strains can be used which allows to quantify the impact of this assumption, as it was done in [36] where the Bulge Test is simulated.

Furthermore, two different causes of stress occur when a membrane is deflected. One is the stress due to the bending of the membrane and the other is the stress due to its stretching. The force or pressure which is needed to overcome the bending stiffness is proportional to the third power of the thickness t^3 of the membrane while the force or pressure which is needed to stretch the membrane is directly proportional to the thickness t . Therefore, depending on the thickness of the membrane, usually one of the two contributions is dominant. When the bending contribution can be neglected, samples are usually referred to be in the so called membrane regime. When the stretching contribution can be neglected, they are referred to be in the so called plate regime. A detailed analysis of conditions under which membrane or plate regime are applicable is provided in [37].

Since the materials which are examined in this work are all much thinner than the deflection which was achieved during the Bulge Test or nanoindentation experiment, the bending stress can be neglected. Therefore, the theory developed for the membrane regime is applicable for all materials in this work. Moreover, this work is focused on circular membranes. It shall be noted that historically, most of Bulge Test experiments were performed on rectangular membranes due to their easier fabrication. For the theoretical description of Bulge Tests on rectangular membranes, it shall be referred to [38].

3.4. Bulge Test Theory

The Bulge Test technique was developed by J.W. Beams in 1959 [26]. For the evaluation of the experiment, he gave a simple but very practical model. Since the experimental uncertainties which occur in Bulge Test experiments are much higher than the error that is induced due to the simple evaluation, this model is sufficient for the evaluation of Bulge Test experiments. Therefore this model is still used when it comes to the analysis of Bulge Tests performed on circular membranes [9, 39, 40]. Nevertheless, it is of course desirable to describe the behavior of a membrane subjected to a uniform pressure as accurately as possible.

There are numerous descriptions of pressurized membranes under different experimental conditions and by different methods, analytic² as well as by finite element simulations. The best available analytic model to describe Bulge Test experiments was established by R. J. Hohlfelder in 1999 [12]. In this model, the pressure-deflection relationship of a pressurized membrane is expressed as the sum of two limiting cases, the limit of small and large deflections. Therefore, this method shall be called the "sum of the limits approach"³. The advantage of this method is that it allows a data analysis of Bulge Test experiments which is as simple as the Beams's equation but yet more precise. In order to derive the sum of the limits equation, four assumptions are needed. The aim of this section is to quantify the error which is caused by these assumptions. To this end, the sum of the limits method is presented in detail. After that, the impact of each assumption is quantified individually through comparison to other works where this specific assumption is not needed. The total error of

²Strictly speaking, some of the analytically derived equations require a numerical determination of their roots. Hence, technically speaking, the theories are not analytic. However, in this work, they shall be referred to as analytic methods in order to point out the contrast to finite element simulations.

³This terminology is already common in the context of the nanoindentation experiment. In the case of the Bulge Test, to the knowledge of the author, it has not been used so far.

the sum of the limits method is estimated by the sum of each individual error. To conclude, the sum of the limits method is compared to other methods which were used to evaluate Bulge Test experiments.

3.4.1. Overview of Common Descriptions of a Pressurized Membrane

In a recent paper by J. B. Messaoud et al. [41], Bulge Test experiments were evaluated through analysis with the five most common methods and taking the average of these five results. All of these methods propose a pressure-deflection relationship of the following form.

$$p(h) = C_1 \frac{t\sigma_0}{r^2} h + C_2 \frac{Et}{(1-\nu)r^4} h^3, \quad (3.8)$$

where p is the pressure, h is the membrane deflection, r the membrane radius and σ_0 the initial stress of the membrane. Moreover, the constant C_1 is determined to be $C_1 = 4$ in all models. The difference of the five descriptions lies in their methods and in the value of C_2 . A summary of these works is given in table 3.1.

Table 3.1.: Summary of different Bulge Test models

	Method	C_2
Beams [26]	Equilibrium of forces (simplified model)	$8/3$
Hohlfelder [12]	Equilibrium of forces	$(8/3) \cdot (1.015 - 0.247\nu)$
Lin [42]	Energy minimization	$(7 - \nu)/3$
Small [43]	Finite element simulation	$(8/3) \cdot (1 - 0.241\nu)$
Pan [44]	Finite element simulation	$(8/3)/(1.026 + 0.233\nu)$

It can be seen that three different approaches were used, two analytic methods and finite element simulations.

Energy minimization is a useful technique which takes advantage of the fact that in equilibrium, the total energy stored in the system is at a minimum. The total energy is composed of the strain energy and the work performed by the applied pressure. In order to minimize the energy, certain assumptions about the membrane geometry, i.e. the shape of the deflection function are made. For example, the membrane may have a spherical cap geometry or a polynomial shape of order k . The description of the shape includes a set of unknowns and the energy is minimized with respect to these unknowns. A comprehensive introduction into the principle of energy minimization methods can be found in [45]. However, the assumptions about the shape of the deformed membrane are somewhat arbitrary. Depending on the assumed shape different results are obtained. Therefore, unless the exact shape of the deformed membrane is known, there is some uncertainty in the results obtained by energy minimization. For this reason, the present work shall be focused on the sum of the limits approach, which is based on the equilibrium of forces. The equilibrium conditions of an elastic body are derived in [35]. To this end, the body is divided in infinitesimal spatial elements. In order to be at equilibrium, the net force applied to every spatial element has to add to zero. This leads to the following condition.

$$\begin{aligned}
\frac{\partial \sigma_x}{\partial x} + \frac{\partial \tau_{yx}}{\partial y} + \frac{\partial \tau_{zx}}{\partial z} + F_x &= 0 \\
\frac{\partial \sigma_y}{\partial y} + \frac{\partial \tau_{zy}}{\partial z} + \frac{\partial \tau_{xy}}{\partial x} + F_y &= 0 \\
\frac{\partial \sigma_z}{\partial z} + \frac{\partial \tau_{xz}}{\partial x} + \frac{\partial \tau_{yz}}{\partial y} + F_z &= 0
\end{aligned} \tag{3.9}$$

at every spatial element of the membrane, where F_i denotes the external force applied to the element in direction i normalized by the volume of the spatial element.

Besides the equilibrium conditions, only two more properties are needed. Firstly Hooke's law and secondly the kinematic conditions of the system, i.e. its geometric properties and the boundary conditions. The general version of Hooke's law is

$$\epsilon_{ij} = \frac{1}{E} [(1 + \nu)\sigma_{ij} - \nu\delta_{ij}(\sigma_{xx} + \sigma_{yy} + \sigma_{zz})], \quad (3.10)$$

where δ_{ij} is the Kronecker Delta. From these principles the force-deflection relationships are derived.

3.4.2. Small and Large Deflection Limit of a Uniformly Pressurized Membrane

In Bulge Test experiments, the membrane is subjected to a uniform pressure p . The pressure $p(h)$ required to achieve a certain deflection h is based on two contributions. Firstly, the membrane is deflected against the resistance of its initial tension σ_0 , and secondly, the membrane is stretched. Both contributions describe a limit of conditions. The first contribution is achieved in the limits of small deflections $h \rightarrow 0$ or high initial stresses $\sigma_0 \rightarrow \infty$. The second contribution is achieved in the limit of large deflections $h \rightarrow \infty$ or at $\sigma_0 = 0$. The pressure-deflection relationships of the two limits are well known. Since the two contributions to the pressure are relatively independent of each other, it is natural to assume that the general case can be approximated by the sum of both contributions. This is the sum of the limits approach.

The small deflection limit can be easily derived. For example, it is obtained as a by product of Beams's model. The large deflections limit, i.e. $\sigma_0 = 0$ is main component needed to derive the sum of the limits equation. This problem was solved by H. Hencky already in 1915 [11]. Both Beams's and Hencky's solution shall be presented in the following. After that, in order to estimate the accuracy of the sum of the limits equation, works by J. D. Campbell [46],

W.B. Fichter [47] and R. Bouzidi et al. [36] are needed. Together, they give a good picture of the error which is made by the assumptions on which the sum of the limits approach is based.

3.4.3. Beams's Model to Describe the Bulge Test

As stated above, Beams gave an easy model to derive the force-deflection relationship $p(h)$. The simplicity of Beams's method is a result of three assumptions. However, usually only two of these assumptions are justified. Beams assumes the membrane to adopt a spherical cap geometry with an unknown radius R . Moreover, he assumes that the deflection is much smaller than the membrane radius, i.e. $h \ll r$. Furthermore, it is assumed that the stress σ is constant throughout the whole membrane. This assumption is critical, because as it is shown in [11], the stress in the center of the membrane is significantly higher than the stress at its edge. However, the assumption of a constant stress together with the spherical cap approach simplify the application of the equilibrium condition significantly since instead of the point wise evaluation of (3.9), the equilibrium condition simplifies to the equilibrium of forces in a spherical pressure vessel which is illustrated in figure 3.3.

$$p \cdot \pi R^2 = \sigma \cdot 2\pi R \cdot t. \quad (3.11)$$

Application of Pythagoras law $(R-h)^2 + r^2 = R^2$ and the assumption $h \ll r$ and hence $R \approx r^2/2h$ yields

$$\sigma = \frac{pR}{2t} \approx \frac{pr^2}{4ht}. \quad (3.12)$$

Since the strain of the membrane induced by the pressure is given by

$$\epsilon = \frac{\Delta l}{l} = \frac{2h^2}{3r^2}, \quad (3.13)$$

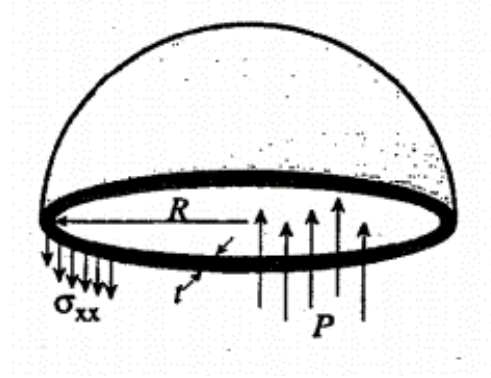


Figure 3.3.: Schematic diagram of a pressurized hemisphere [12].

the stress σ can be expressed as

$$\sigma = \frac{E}{1-\nu}(\epsilon + \epsilon_0) = \frac{E}{1-\nu} \cdot \frac{2h^2}{3r^2} + \sigma_0 \quad (3.14)$$

by using Hooke's law twice. ϵ_0 denotes the initial strain, i.e. the strain which is caused by the initial tension σ_0 . As a result of the equations (3.12) and (3.14), the pressure-deflection relationship becomes

$$p_{\text{Beams}}(h) = \frac{4t\sigma_0}{r^2}h + \frac{8Et}{3(1-\nu)r^4}h^3. \quad (3.15)$$

The first term can be understood as the pressure required to overcome the initial tension of the membrane, while the second term accounts for the stretching of the membrane which is caused by the deflection. In this sense, equation (3.15) is also a sum of two limiting cases. As it will be shown, it is indeed very similar to the sum of the limits equation. For the first limit, the case of a membrane with initial tension σ_0 subjected to an infinitesimal deflection h , the exact solution can even be derived in the same way. Since the deflection h is infinitesimal, the stress σ in the membrane can be approximated by $\sigma = \sigma_0$.

Since the stress only consists of the initial tension, in this case the assumption of a constant stress becomes accurate. Therefore it can be concluded as above $\sigma_0 = \sigma = \frac{pr^2}{4ht}$ and due to $\epsilon \approx 0$ the pressure-deflection relationship becomes

$$p_{\text{small}}(h) = \frac{4t\sigma_0}{r^2}h. \quad (3.16)$$

Of course equation (3.16) is only exact in the case of an infinitesimal deflection. Its error for a finite deflection h is computed in [46]. To this end, the dimensionless pressure P is defined as

$$P = \frac{pr}{Et} \left(\frac{\sigma}{E} \right)^{-3/2} \quad (3.17)$$

It is shown that for $P < 1$, the relative error of the central deflection h obtained by equation (3.16) is less than 5%. The limit of large deflections is reached within the same accuracy when $P > 100$. This criterion is often fulfilled when it comes to the examination of graphene membranes, for example in [48] and [49].

3.4.4. Hencky's Solution for the Large Deflection Limit

Hencky's solution for a pressurized membrane is based on the exact equilibrium condition (3.9). The assumption $\sigma_0 = 0$ significantly facilitates the numerical evaluation of the resulting system of differential equations.

Moreover, it is assumed that the loading of the membrane is uniformly lateral, i.e. the force which applies to every point of the membrane is always in z-direction only. Under a uniform pressure, this is not exactly given since the pressure applies perpendicular to the membrane. Hence, for every point of the membrane which has a non zero slope, besides the z-component, the force also consists of a radial component. This radial component is neglected in Hencky's analysis. A schematic diagram of the two kinds of load is shown in figure 3.4. However, the effect of this assumption is only relevant for very large pressures

3. Theory of Bulge Test and Nanoindentation

as is it shown in [47], where the same problem is solved with the exact force caused by the uniform pressure.

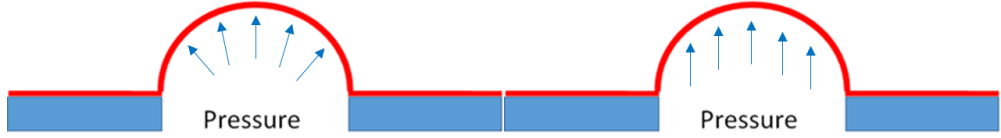


Figure 3.4.: Schematic diagram of a uniformly pressurized membrane (left) and a membrane subjected to a uniform lateral load (right).

Hencky's approach is to express the radial and tangential stresses σ_r and σ_t as well as the deflection as a function of the radial position $\rho = x/r$ on the membrane, where $0 \leq x \leq r$. This function is represented as a power series where the stress in the center of the membrane is determined by the coefficient B_0 . By using the governing equilibrium equations and Hooke's law, B_0 can be calculated as the root of the equation

$$\begin{aligned}
 B_0(1 - \nu) & - (3 - \nu)\frac{1}{B_0^2} - (5 - \nu)\frac{2}{3B_0^5} - (7 - \nu)\frac{13}{18B_0^8} - (9 - \nu)\frac{17}{18B_0^{11}} \\
 & - (11 - \nu)\frac{37}{27B_0^{14}} - (13 - \nu)\frac{1205}{567B_0^{17}} - \dots = 0. \quad (3.18)
 \end{aligned}$$

It can be seen that as a result of the exact treatment, there is no general result such as equation (3.15). Instead, equation (3.18) has to be solved for every ν . However, due to the fast convergence of the series it is sufficient to consider the given summands for the numerical evaluation. For $\nu = 0.3$ the value of B_0 was already calculated by Hencky. In order to solve equation (3.18) for arbitrary values of ν , a mathematica 10.0 notebook was written (see Appendix A for the corresponding source code). The results for various values of ν are shown in table 3.2. It has to be noted that there is an algebraic error in Hencky's paper [11], where the last coefficient $1205/567$ is not given correctly,

see for example reference [46]. However, the relative error of B_0 in Hencky's results is less than 1% for all ν .

Table 3.2.: B_0 as a function of ν

ν	0	0.05	0.1	0.15	0.165	0.2
B_0	1.619	1.6327	1.6477	1.664	1.6692	1.682
ν	0.25	0.3	0.35	0.4	0.45	0.5
B_0	1.7018	1.7239	1.7486	1.7765	1.8084	1.8451

The central deflection of the membrane in Hencky's model is given by

$$h = \left(\frac{pr^4}{Et} \right)^{1/3} \left(\frac{1}{B_0} + \frac{1}{2B_0^4} + \frac{5}{9B_0^7} + \frac{55}{72B_0^{10}} + \frac{7}{6B_0^{13}} + \frac{205}{108B_0^{16}} + \dots \right). \quad (3.19)$$

Since B_0 only depends on the Poisson's ratio ν , it is useful to define $A_{h_0}(\nu)$ as

$$A_{h_0}(\nu) = \left(\frac{1}{B_0} + \frac{1}{2B_0^4} + \frac{5}{9B_0^7} + \frac{55}{72B_0^{10}} + \frac{7}{6B_0^{13}} + \frac{205}{108B_0^{16}} + \dots \right). \quad (3.20)$$

and $K(\nu)$ as

$$K(\nu) = (A_{h_0}(\nu))^{-3}. \quad (3.21)$$

With these definitions, equation (3.19) becomes

$$h = \left(\frac{pr^4}{Et} \right)^{1/3} A_{h_0}(\nu) \quad (3.22)$$

3. Theory of Bulge Test and Nanoindentation

and hence the pressure-deflection relationship is

$$p_{\text{large}}(h) = K(\nu) \frac{Et}{r^4} h^3. \quad (3.23)$$

Hencky's results shall now be used to establish the sum of the limits equation. To this end, the most common values of $K(\nu)$ were calculated with the values from table 3.2 and the definitions (3.20) and (3.21). The results are shown in table 3.3.

Table 3.3.: $K(\nu)$ for selected values of ν

ν	0	0.05	0.1	0.15	0.165	0.2
$K(\nu)$	2.709	2.818	2.94	3.075	3.118	3.227
ν	0.25	0.3	0.35	0.4	0.45	0.5
$K(\nu)$	3.397	3.593	3.817	4.078	4.387	4.756

In order to facilitate the evaluation of experimental data for all other values of ν , it is useful to give an explicit expression of the function $K(\nu)$. To this end, $K(\nu)$ was fit with a function of the form $K(\nu) = (a - b\nu)/(1 - \nu)$:

$$K(\nu) = \frac{2.713 - 0.666\nu}{1 - \nu}. \quad (3.24)$$

The fit is based on table 3.3 and approximates $K(\nu)$ with an accuracy of 0.1%. The coefficients are slightly different from the coefficients obtained in [12], where the problem was treated in a similar way. The explicit formulation of equation (3.23) becomes

$$p_{\text{large}}(h) = \frac{(2.713 - 0.666\nu)Et}{(1 - \nu)r^4} h^3. \quad (3.25)$$

This is the pressure-deflection relationship of a membrane with $\sigma_0 = 0$. It is also the formula which describes the limit of large deflections and hence the

second of the two summands of the sum of the limits equation. Adding the two summands yields the complete equation.

$$p_{\text{sum}}(h) = \frac{4t\sigma_0}{r^2}h + K(\nu)\frac{Et}{r^4}h^3. \quad (3.26)$$

At this point, it is useful to recapitulate the assumptions which were needed for the derivation of the sum of the limits equation. Four assumptions were used.

(1) The pressure in the intermediate regime between small deflection limit and large deflection limit is correctly captured by the superposition of the two limits.

(2) The load caused by the pressure is uniformly lateral.

(3) The strains in the pressurized membrane are infinitesimal.

(4) The bending stress can be neglected.

In the next sections, the effect of each of these assumptions shall be investigated.

3.4.5. Behavior of a Membrane with Initial Tension in the Intermediate Regime

In order to estimate the error of equation (3.26), it shall be compared to the exact solution of a membrane with initial tension σ_0 subjected to a uniform lateral load [46]. In this work, Campbell shows that Hencky's method can be modified to include initial tension. Again using the assumptions (1), (2) and (3), it is shown that a more general version of equation (3.18) is

$$\begin{aligned}
 (1 - \nu)B_0 &= (3 - \nu)\frac{1}{B_0^2} - (5 - \nu)\frac{2}{3B_0^5} - (7 - \nu)\frac{13}{18B_0^8} - (9 - \nu)\frac{17}{18B_0^{11}} \\
 &- (11 - \nu)\frac{37}{27B_0^{14}} - (13 - \nu)\frac{1205}{567B_0^{17}} - \dots \\
 &= (1 - \nu)\frac{\sigma_0}{k},
 \end{aligned} \tag{3.27}$$

where

$$k = \frac{1}{4} \left(Ep^2 \left(\frac{r}{t} \right)^2 \right)^{1/3}. \tag{3.28}$$

The central deflection of the membrane is given by equation (3.19), as before. Equation (3.27) may seem to be only a small change compared to equation (3.18), but this change has significant implications. Firstly, in order to determine the deflection of the membrane, all its properties like the Young's modulus E and the initial stress σ_0 have to be known a priori. More precisely, equation (3.22) becomes

$$h = \left(\frac{pr^4}{Et} \right)^{1/3} \cdot A_{h_0} \left(\nu, \frac{\sigma_0}{k} \right). \tag{3.29}$$

Since the purpose of Bulge Test experiments is to determine the Young's modulus E and the initial tension σ_0 , Campbell's equation (3.29) is not suited for their evaluation. Even if all the properties are known, equation (3.27) has to be solved for every pressure p which makes the analysis a very time-consuming task. Therefore, this approach is not suited for the evaluation of Bulge Test experiments. However, it is useful to compare the exact solution to the sum of the limits equation (3.26) in order to estimate the error of the latter equation. This approach shall be pursued in the following. A general formula for the

relation p_{sum}/p as a function of the deflection height h was found to be

$$\frac{p_{\text{sum}}}{p} = \left(A_{h_0} \left(\nu, \frac{\sigma_0}{k} \right) \right)^3 \cdot \left(K(\nu) + \frac{4\sigma_0 r^2}{Eh^2} \right), \quad (3.30)$$

where $K(\nu)$ denotes the factor derived through equations (3.18) and (3.24), i.e. for $\sigma_0 = 0$, while $A_{h_0} \left(\nu, \frac{\sigma_0}{k} \right)$ is obtained by equation (3.27). Since the right hand side of equation (3.27) converges to 0 as $p \rightarrow \infty$,

$$\left(A_{h_0} \left(\nu, \frac{\sigma_0}{k} \right) \right)^3 \rightarrow (K(\nu))^{-1} \text{ as } p \rightarrow \infty. \quad (3.31)$$

Moreover, $h \rightarrow \infty$ as $p \rightarrow \infty$ and therefore

$$\frac{4\sigma_0 r^2}{Eh^2} \rightarrow 0 \text{ as } p \rightarrow \infty. \quad (3.32)$$

This proves that in the limit of large deflections, p_{sum}/p converges to 1 and hence the error of the approximation p_{sum} converges to 0 as $p \rightarrow \infty$. In order to further investigate the error of p_{sum} , it is useful to express p_{sum}/p as a function of the pressure p instead of the height h . This yields

$$\begin{aligned} \frac{p_{\text{sum}}}{p} &= A_{h_0} \left(\nu, \frac{\sigma_0}{k} \right) \left[K(\nu) \left(A_{h_0} \left(\nu, \frac{\sigma_0}{k} \right) \right)^2 + \frac{4\sigma_0}{(Ep^2)^{1/3}} \left(\frac{t}{r} \right)^{2/3} \right] \\ &= A_{h_0} \left(\nu, \frac{\sigma_0}{k} \right) \left[K(\nu) \left(A_{h_0} \left(\nu, \frac{\sigma_0}{k} \right) \right)^2 + \frac{\sigma_0}{k} \right], \end{aligned} \quad (3.33)$$

where k is again defined by equation (3.28). Equation (3.33) shows that for a fixed Poisson's ratio ν , the error p_{sum}/p only depends on the ratio σ_0/k .

In order to calculate the error and to illustrate the above findings, exact pressure-deflection curves were calculated for exemplary samples with typical parameters. These results were compared to the pressure-deflection curves obtained by equation (3.26). This was done in the following way: For given

3. Theory of Bulge Test and Nanoindentation

parameters p , t , r , E , σ_0 and ν , the deflection height h was obtained by solving equation (3.27) (see Appendix A for the corresponding mathematical source code) and using equation (3.22). The calculated height was then used in equation (3.26) to obtain p_{sum} . With this procedure, both the exact pressure p and the approximated pressure p_{sum} required to achieve a given height were calculated. Applying this calculation to different pressures p gave two force-deflection curves, the exact and the approximated curve. An exemplary pressure-deflection curve for a typical freestanding TPT-CNM with the parameters $t = 2$ nm, $r = 8$ μm , $E = 10$ GPa, $\sigma_0 = 20$ MPa and $\nu = 0.35$ is shown in figure 3.5. It can be seen that in contrast to Beams's equation (3.15), equation (3.26) agrees very well with the exact solution.

In order to further explore the error of equation (3.26), the relative error $\frac{p_{\text{sum}}}{p} - 1$ was calculated. To this end, the above mentioned exemplary TPT-CNM was taken as a starting point. For each of its parameters σ_0 , E , r and t , a series of calculations was performed where all parameters except the examined parameter were fixed to the value stated above. The relative error $\frac{p_{\text{sum}}}{p} - 1$ was plotted as a function of the deflection height h as it would be done in a pressure-deflection curve. The results are shown in figure 3.6. The figure showing the error as a function of the membrane thickness t is not shown because any thickness t yields the same error curve. The reason for this will be explained below.

It can be seen that the relative error approaches zero for small and large deflections and is maximally 1.635%. Furthermore, as long as the Poisson's ratio ν is fixed, the maximal error is independent of the other parameters. This finding may seem surprising, but it is explained by equation (3.33), where the error only depends on ν and σ_0/k . In the case of $\nu = 0.35$, the error has its maximum at $\sigma_0/k = 0.985$. Hence, speaking of $\frac{p_{\text{sum}}}{p}$ as a function of the

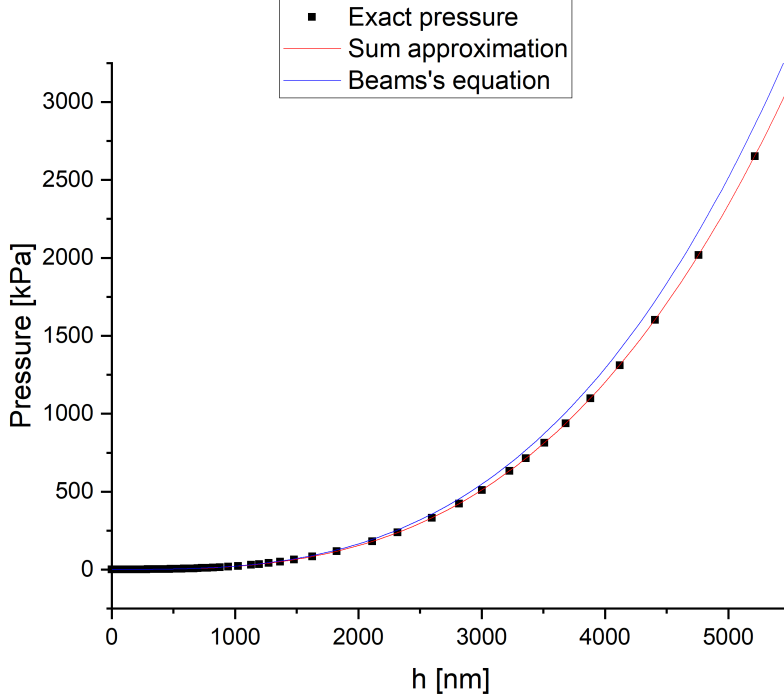


Figure 3.5.: Comparison of Beams's formula and the sum of the limits formula with the exact solution for an exemplary CNM.

pressure p , $\frac{p_{\text{sum}}}{p}$ is equal for constant

$$\frac{\sigma_0}{k} = 4\sigma_0 \left(Ep^2 \left(\frac{r}{t} \right)^2 \right)^{-1/3} \quad (3.34)$$

or put in a different way

$$p_{\text{max}} \propto \sigma_0^{3/2} \cdot E^{-1/2} \cdot \frac{t}{r}, \quad (3.35)$$

where p_{max} denotes the pressure at which the error $\frac{p_{\text{sum}}}{p} - 1$ is maximal. In order to understand the error $\frac{p_{\text{sum}}}{p}$ as a function of the deflection height

3. Theory of Bulge Test and Nanoindentation

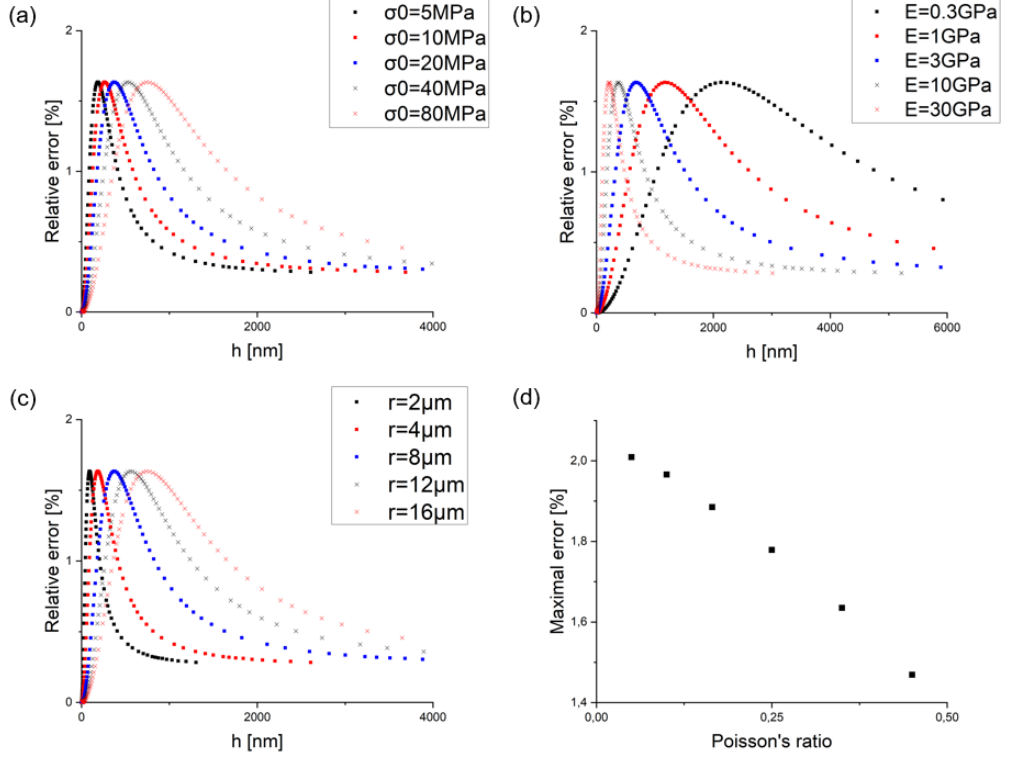


Figure 3.6.: (a) Error of the sum approximation compared to Campbell's solution as a function of the initial tension σ_0 . (b) Error of the sum approximation compared to Campbell's solution as a function of the Young's modulus E . (c) Error of the sum approximation compared to Campbell's solution as a function of the membrane radius r . The parameters which are not examined in each figure are fixed to $t = 2$ nm, $r = 8$ μm , $E = 10$ GPa, $\sigma_0 = 20$ MPa and $\nu = 0.35$. (d) Maximum error of the sum approximation compared to Campbell's solution as a function of the Poisson's ratio ν .

h , equation (3.29) is needed. Since the deflection height h scales with $p^{1/3}$, $\frac{p_{\text{sum}}}{p}(h)$ depends only on σ_0 , E and r . The deflection height h_{max} at which the error $\frac{p_{\text{sum}}}{p} - 1$ is maximal is proportional to

$$h_{\text{max}} \propto \sigma_0^{1/2} \cdot E^{-1/2} \cdot r. \quad (3.36)$$

These relationships are nicely illustrated by figure 3.6 (a), (b) and (c). Moreover, equation (3.36) explains why $\frac{p_{\text{sum}}}{p}(h)$ is independent of the membrane thickness t .

The last parameter to be investigated is the Poisson's ratio ν . In order to determine its influence, the maximal error of $\frac{p_{\text{sum}}}{p} - 1$ was calculated for different values of ν with the same method as above. The results are shown in figure 3.6 (d). It can be seen that the maximal error decreases with the Poisson's ratio ν and does not exceed 2.1% even for unusually small values of ν . This shows that equation (3.26) indeed is a good approximation to the exact solution for all possible parameters.

With these results, it can be concluded as an interim summary that Campbell's description of a uniformly loaded membrane can be approximated by equation (3.26) with a relative error of less than 2.1%. As stated in equation (3.8), the only difference of Beams's equation (3.15) compared to the sum of the limits equation is the factor C_2 which depends on the Poisson's ratio. Comparison of table 3.24 with $C_2/(1 - \nu)$ yields that Beams's equation exhibits a relative error of up to 12% in the case of $\nu = 0.5$ which has to be added to the deflection dependent error. The accuracy of Beams's model increases with a decreasing value of ν . However, it has to be kept in mind that Campbell's approach requires the assumption of a uniformly lateral load which is not needed in Beams's description of the Bulge Test. The impact of the uniformly lateral load assumption shall be explored in the next section. Moreover, the impact of the assumption of infinitesimal strains shall be studied which is needed in both Campbell's and Beams's works.

3.4.6. Impact of the Assumption of a Uniformly Lateral Load

When the membrane is subjected to a high pressure, the membrane is not only deflected in z-direction but there is also a radial deflection component. This effect was investigated by W.B. Fichter [47]. As Hencky's problem, this work is

3. Theory of Bulge Test and Nanoindentation

restricted to the case of no initial tension. However, since the case of no initial tension is equivalent to the limit of large deflections, it can be assumed that the radial deflections for initially tensioned membranes will be approximately identical to those of membranes without initial tension due to the high pressure.

In order to solve the uniform pressure problem, Fichter also uses Hencky's approach. The lateral equilibrium condition remains unchanged, but the radial equilibrium condition is adapted according to the load caused by the uniform pressure. As in the case of membranes with an initial tension, Hencky's approach of expressing stresses and deflection as a power series still works, but it does not yield a general formula for the pressure-deflection relationship. Therefore, Fichter's results are not very practical for the data analysis of Bulge Test experiments. However, they give a good estimation of the error one makes by assuming a uniform lateral load for case of the large deflection limit.

Since the radial component of the load is increasing with the deflection of the membrane, the relative difference between Hencky's and Fichter's models increases with the deflection as well. Dimensionless pressure-deflection curves for $\nu = 0.2$, $\nu = 0.3$ and $\nu = 0.4$ are shown in figure 3.7(a).

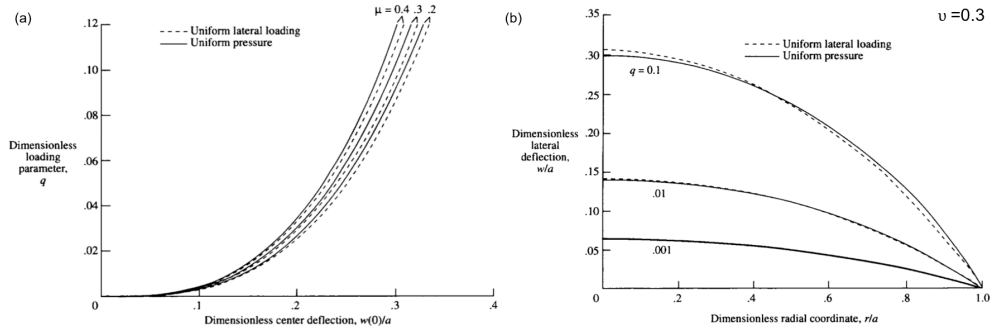


Figure 3.7.: (a) Comparison of the load-deflection curves of the uniform lateral load and uniform pressure model. (b) Comparison of the membrane shape of the uniform lateral load and uniform pressure model for $\nu = 0.3$ [47].

The dimensionless loading parameter q is defined as $q = pr/Et$. With this

definition, Hencky's law (3.23) becomes

$$q = K(\nu) \left(\frac{h}{r} \right)^3. \quad (3.37)$$

Figure 3.7 (a) yields two important observations. Firstly, it can be observed that the error caused by the assumption of a uniform lateral load increases with the Poisson's ratio ν . Secondly, it is shown that as expected, the two models agree quite well for small deflections while the difference increases for larger deflections. The maximal dimensionless deflection in the Bulge Test experiments of the present work is usually around $h/r = 0.1$ which corresponds to dimensionless pressure of $q = 0.003$ to $q = 0.004$, depending on the Poisson's ratio ν . It can be seen that for these small values of q , both solutions are in good agreement. The procedure for computing the exact error caused by the uniform lateral load assumption is described in [47]. However, it is a complicated task which would go beyond the scope of this work. A more detailed comparison between the different scenarios is given in the next section, where the finite strains are taken into account as well.

3.4.7. The Influence of Finite Strains

In [36], the behavior of a circular membrane under uniform pressure was also examined by a finite elements simulation. In this simulation, no simplifying assumptions are needed. An exemplary membrane with parameters $E_{2D} = 311488 \text{ Pa m}$, $\nu = 0.34$ and $r = 0.1425 \text{ m}$ is simulated at pressures of 100 kPa, 250 kPa and 400 kPa. The corresponding dimensionless pressures are $q = 0.0458$, $q = 0.114$ respectively $q = 0.183$. Figure 3.8 (a) shows the central deflection of the membrane at 250 kPa according to Hencky's theory, Fichter's theory and the simulation. It can be seen that compared to the simulation, Hencky's model overestimates the central deflection by about 0.9%. For a fixed height this means that the pressure is underestimated by 2.7%. This

3. Theory of Bulge Test and Nanoindentation

underestimation is the result of both assumptions of a uniformly lateral load (2) and infinitesimal strains (3) together.

The error induced by neglecting the finite strains does not necessarily compensate parts of the error induced by the assumption of a uniformly lateral load, as it is shown in figure 3.8 (b). In the example of $p = 100$ kPa which corresponds to $q = 0.046$, the assumptions (2) and (3) together lead to an overestimation of the central deflection and hence to an underestimation of the required pressure for a given height. It was estimated from figures 3.7 and 3.8 that the pressure at $q = 0.046$ is underestimated by up to 6% in Hencky's model.

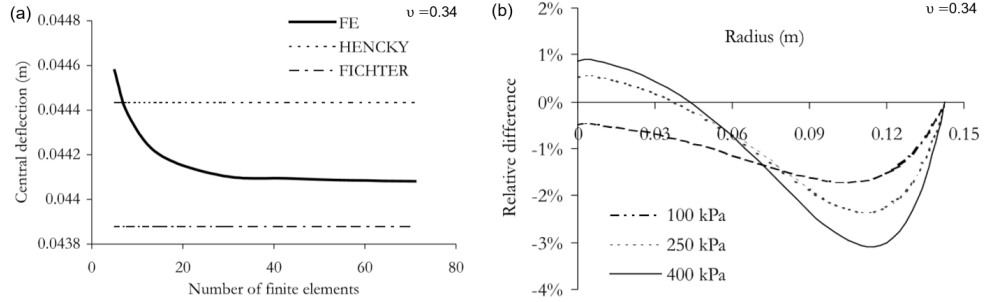


Figure 3.8.: (a) Comparison of the central deflections achieved by Hencky, Fichter and the FES simulation for a dimensionless pressure of $q = 0.114$. (b) Relative difference of the finite elements simulation compared to Fichter's solution as a function of the radial position in the membrane. For the purpose of this analysis, only the center of the membrane, $r = 0$ is relevant. Since the central deflection in Fichter's model is lower than in Hencky's model, the errors due to assumptions (3) and (4) add up in the case of $p = 100$ kPa ($q = 0.046$) and partially compensate in the cases of $p = 250$ kPa ($q = 0.114$) and $p = 400$ kPa ($q = 0.183$) [36]. Reproduced with permission.

There is no data for values of q other than 0.046, 0.114 and 0.183. Estimating the error due to assumptions (2) and (3) in the ranges which are not covered is a difficult task. Since the maximal dimensionless pressure used in the present work is around $q = 0.004$, the small values of q are of particular importance. As

both effects, the radial deflection and the finite strains are only of significance at high pressures, it is reasonable to assume that the error for small values of q is much smaller than the above calculated value for higher dimensionless pressures. This intuitive argument is supported by a Bulge Test experiment by Koenig et al. [48]. In their experiment, it was found that the shape of a pressurized graphene membrane is in good agreement with the shape predicted by Hencky's solution. The experiment was performed at a dimensionless pressure of $q = 0.0027$. Since the shape is a good indicator of the accuracy of the central deflection, as it is shown in figure 3.7(b), this finding indicates that for $q = 0.0027$ the underestimation of the pressure p required to achieve a certain deflection h due to assumptions (2) and (3) is much smaller than at higher values of q . Therefore, in the pressure range of $q \leq 0.005$, a maximal error of 4% seems reasonable.

However, it should be kept in mind that assumptions (2) and (3) may induce a significant underestimation of the required pressure at higher dimensionless pressures q .

3.4.8. The Influence of Bending Stiffness

So far, all calculations were based on the assumption that the bending stress can be neglected. Whether or not this is true depends mainly on the ratio of the thickness of the membrane compared to the central deflection. In order to estimate the influence of the bending stiffness, it is useful to know the behavior of a uniformly loaded film in the plate regime, i.e. a film where the bending stiffness is dominating and the stretching can be neglected.

The pressure-deflection relationship in this scenario was derived by Timoshenko [50]

$$p_{\text{plate}} = \frac{16}{3(1 - \nu^2)} \cdot \frac{Et^3}{r^4} h. \quad (3.38)$$

3. Theory of Bulge Test and Nanoindentation

With the help of equation (3.38), it can be easily calculated whether or not the bending stiffness needs to be considered. When the bending stiffness is significant, Hohlfelder [12] suggests to add the term p_{plate} to the pressure-deflection relationship. This approach leads to

$$p_{\text{sum}}(h) = \frac{4t\sigma_0}{r^2}h + \frac{Et}{r^4}h^3 \left(K(\nu) + \frac{16}{3(1-\nu^2)} \left(\frac{t}{h} \right)^2 \right). \quad (3.39)$$

The idea behind equation (3.39) is the same as for the sum of the limits approach. More precisely, the pressure required for both deformations bending and stretching together to stay at an equilibrium is assumed to be the sum of both individual contributions. Since this assumption was fairly accurate in the case of the sum of the limits equation, it is reasonable to assume that the error of this assumption is small in the case of the bending stiffness, too. Moreover, usually the term attributed to the bending stiffness is much smaller than the term attributed to the stretching. In this case, the term attributed to the bending stiffness can be thought of as a first order perturbation correction.

Another advantage of equation (3.39) is that by comparison of the terms $K(\nu)$ and $\frac{16}{3(1-\nu^2)} \left(\frac{t}{h} \right)^2$ it can be easily seen whether the bending stiffness is significant or not. For a typical CNM with a thickness of $t = 2$ nm, the contribution of the bending stiffness to the required pressure is far less than 0.1%. Therefore, it can be neglected.

3.4.9. Conclusions

In this section, the sum of the limits formula was derived. In order to establish its pressure-deflection relationship, four assumptions (1) to (4) were needed. The error induced by each assumption was estimated with the help of the works shown in table 3.4.

Firstly, it was assumed that the exact solution including the initial tension can be expressed as the sum of the small deflection limit and the large deflection

Table 3.4.: Summary of the theoretic descriptions of a pressurized membrane needed for quantification of the error in the sum of the limits approach

Author	Method	Initial stress included	Type of load
Hencky	analytic	no	uniformly lateral
Campbell	analytic	yes	uniformly lateral
Fichter	analytic	no	uniform pressure
Bouzidi et al.	Finite element simulation	no	uniform pressure
Timoshenko	analytic description of a uniformly loaded plate	no	uniformly lateral

limit. It was shown that the error of this approximation is an overestimation of the required pressure and that the error converges to zero in the limits of $h \rightarrow 0$ and $h \rightarrow \infty$. Moreover, it was shown that the maximum of the error does not exceed 2.1% under any circumstances. For CNMs, the Poisson's ratio is assumed to be $\nu = 0.35$ [51]. This means that the maximum error is 1.635%. For usual Bulge Test experiments, this maximal error is in the range of the maximum applied pressure.

Secondly, for the calculation of the large deflection limit, a uniform lateral load and infinitesimal strains were assumed. Both assumptions are quite accurate for small dimensionless pressures $q = pr/Et$. However, for large dimensionless pressures, the error of these assumptions becomes the dominant error. It was shown exemplarily that for $q = 0.046$ both effects together lead to an underestimation of the required pressure of ca. 6% and for $q = 0.114$ both effects together lead to an underestimation of the required pressure of 2.7%. In the typical range of Bulge Test experiments, $q \leq 0.005$, the maximum error

3. Theory of Bulge Test and Nanoindentation

due to both effects was assumed to be 4%.

Lastly, it was assumed that the bending stiffness can be neglected. It was shown that this is true for the membranes investigated in this work. In case that the bending stiffness needs to be considered, it was suggested to use equation (3.39).

In the evaluation of Bulge Test experiments, an overestimation of the required pressure p by a constant factor c leads to an underestimation of Young's modulus and initial tension by the factor c and vice versa. It can therefore be concluded that the error of Young's modulus and initial tension due to the evaluation with the sum of the limits method is in the range of +2.1% / - 3.8%, as long as the dimensionless pressure q does not exceed 0.005.

To sum up, the sum of the limits equation (3.26) shall be compared to the four other theories mentioned in table 3.1. Of particular interest is the comparison to Beams's equation since it has been used widely in the literature. As already stated, the small deflections term of all five equations is identical. This implies that the data analysis with all methods yields an identical initial tension. However, depending on the factor C_2 in equation (3.8), different results for the Young's modulus are obtained. The function $C_2(\nu)$ for all five theories is shown in figure 3.9. The finite elements simulation by Small shows the best agreement with the sum of the limits equation while the two analytic models by Beams and Lin show a decent discrepancy. Pan's model is in a good agreement for large values of the Poisson's ratio. The sum of the limits approach and Beams's model almost agree for small values of ν while for large values of ν the constant C_2 in Beams's model is up to 12% higher than in the sum of the limits model. This means that in Beams's model the Young's modulus is underestimated by 12% compared to the sum of the limits model. For CNMs, the relative deviation between both models is 7%.

The main advantage of the sum of the limits approach compared to the other methods is the quantification of the impact of its underlying assumptions. This

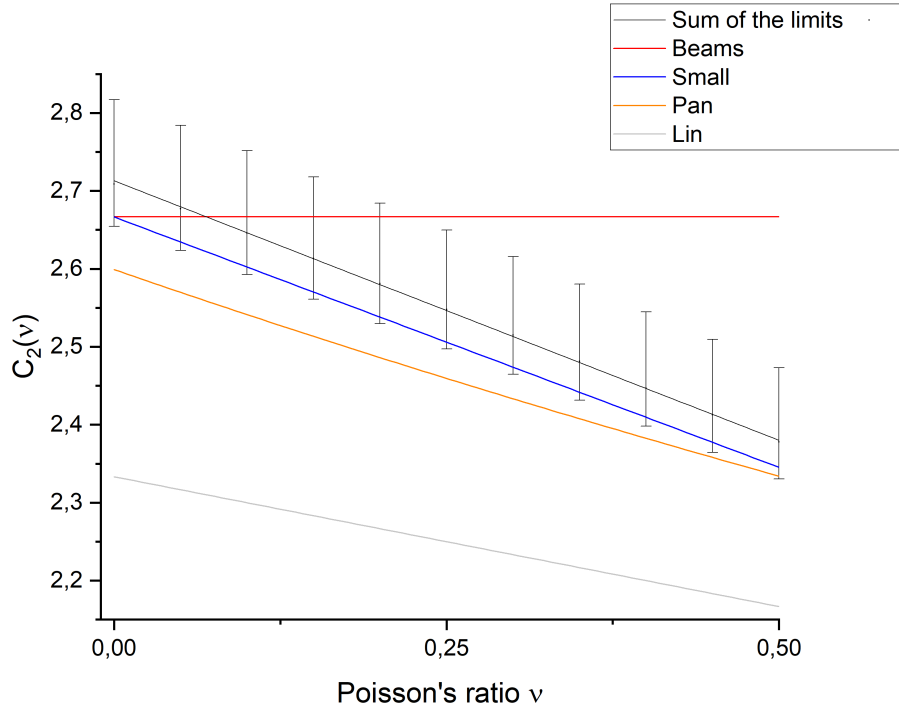


Figure 3.9.: Comparison of the pre factor C_2 in the most common theoretic descriptions of a pressurized membrane.

quantification is not possible for the other approaches. Moreover, the data analysis with the sum of the limits model is as simple as with Beams's formula. Therefore, the use of the sum of the limits model is advisable.

3.5. Nanoindentation Theory

Nanoindentation was originally a means to determine the Young's modulus and the hardness of films supported on a solid substrate. To this end, so called nanoindenters with sharp tips were used to record a load vs. indentation

3. Theory of Bulge Test and Nanoindentation

depth curve [25]. With the increasing ability to fabricate films with a thickness of only several nm, the same principle was extended to nanoindentation on freestanding membranes by Espinosa et al. [10]. This allows to extract the mechanical properties of the membrane without being influenced by the supporting substrate which is particularly important for 2D materials. A popular tool to conduct nanoindentation on freestanding membranes is the atomic force microscope (AFM) because it allows a precise measurement of load and membrane displacement. Moreover, the AFM also allows a very precise positioning of the indenting tip, which is crucial when small membranes are investigated.

As well as for the Bulge Test, the main task for a theoretical description of a nanoindentation experiment is to find the load-deflection relationship. However, in the case of nanoindentation, the load is not achieved by a pressure but by the force F exerted by the indenter.

Also as for the Bulge Test, the best way to approach a theoretical description of nanoindentation on freestanding membranes is to start with the two limiting cases: The small indentation limit and the large indentation limit. The large deflection limit is again equivalent to the case of no initial tension, $\sigma_0 = 0$. However, the description of nanoindentation is more complex than the Bulge Test since there is an additional parameter. This is the size of the indenter, which is the AFM-tip in the case of AFM-nanoindentation. In the general case, this additional parameter makes it impossible to give a general solution as for the Bulge Test. There exists only one purely analytical solution for the special case of point indentation, i.e. $r_{\text{indenter}} = 0$, no initial tension, i.e. $\sigma_0 = 0$ and $\nu = 1/3$.⁴ The solution to this problem was found by E. Schwerin in 1929 [52].

$$F = \frac{\pi}{3} \frac{Et}{r^2} h^3. \quad (3.40)$$

Of course, this result is not sufficient for the evaluation of nanoindentation

⁴In the case of $\nu \neq 1/3$, the resulting equations can be derived analytically but need to be solved numerically [13].

experiments. An extensive analysis of the behavior of thin freestanding membranes in an indentation experiment is given by D. Vella and B. Davidovitch [13]. In this section, the findings of Vella and Davidovitch which are relevant to the present work shall be presented. Additionally, the tip correction factor α_{tip} will be defined and analyzed.

In order to derive the force-deflection relationship, it is useful to employ the dimensionless deflection

$$\tilde{\delta} = \frac{h}{r} \left(\frac{E}{\sigma_0} \right)^{1/2} \quad (3.41)$$

and the dimensionless force

$$\tilde{F} = \frac{E^{1/2} F}{\sigma_0^{3/2} t r}. \quad (3.42)$$

With these definitions, equation (3.40) reduces to

$$\tilde{F} = \frac{\pi}{3} \tilde{\delta}^3. \quad (3.43)$$

3.5.1. Large Deflection Limit

For point indentation, i.e. $r_{\text{indenter}} = 0$, Vella and Davidovitch find that equation (3.40) can be generalized to arbitrary values of ν by solving the Föppl-von Kármán equations for each value of ν . Unfortunately, for all $\nu \neq 1/3$, a part of the solving process has to be performed numerically. However, the force-deflection relationship can be expressed as

$$\tilde{F} = \alpha(\nu) \tilde{\delta}^3, \quad (3.44)$$

where $\alpha(\nu)$ can be approximated as

$$\alpha(\nu) = 0.867 + 0.2773\nu + 0.805\nu^2. \quad (3.45)$$

3. Theory of Bulge Test and Nanoindentation

The error of this approximation is less than 0.7% for all $0 \leq \nu \leq 1/2$. Another extension of equation (3.40) is to keep $\nu = 1/3$ fixed but to allow $r_{\text{indenter}} > 0$. For the sake of simplicity, the indenter is assumed to have the shape of a disk, for example achieved by a cylindrical indenter. It is useful to define the dimensionless indenter size as

$$\rho_{\text{in}} = r_{\text{indenter}}/r. \quad (3.46)$$

With this definition, the force-deflection relationship becomes

$$\tilde{F} = \frac{\pi}{3} \left(1 - \rho_{\text{in}}^{2/3}\right)^{-3} \tilde{\delta}^3, \quad (3.47)$$

which is valid for $\nu = 1/3$ and all $\rho_{\text{in}} < 1$. It can be seen that in the limit of $\rho \rightarrow 0$, equation (3.47) coincides with equation (3.40) which makes it a more general version of Schwerin's classical solution. In the limit of $\rho \rightarrow 1$, the force \tilde{F} diverges, $\tilde{F} \rightarrow \infty$, since the clamped edges are stretched infinitely. In practice of course, an indenter with the size of the membrane would rupture the membrane.

When both parameters $\nu \neq 1/3$ and $r_{\text{indenter}} > 0$ are allowed, the effect of ρ_{in} can only be treated by perturbation theory. Vella and Davidovitch find that for $0 < \rho_{\text{in}} \ll 1$

$$\tilde{F} \approx \left(\alpha(\nu) + \frac{6}{(2\pi(1+\nu))^{1/3}} \cdot \alpha(\nu)^{4/3} \rho_{\text{in}}^{2/3} \right) \tilde{\delta}^3, \quad (3.48)$$

where $\alpha(\nu)$ is approximated by equation (3.45). As in the case of point indentation, it is also possible to determine $\alpha(\nu)$ exactly. However, this has again to be done numerically for every value of the Poisson's ratio ν . Therefore, equation (3.45) shall be used here.

These results of Vella and Davidovitch shall now be used for an estimation of the accuracy of equation (3.48) when the tip cannot be approximated by

a point indenter. To this end, it is useful to define the tip correction factor α_{tip} as the force that is needed to achieve a certain deflection with a tip of the radius r_{indenter} divided by the force which would be needed to achieve the same deflection via point indentation:

$$\alpha_{\text{tip}} = \alpha_{\text{tip}}(\nu, \rho_{\text{in}}) = \tilde{F}_{\rho_{\text{in}}} / \tilde{F}_{\rho_{\text{in}}=0}. \quad (3.49)$$

In the case of $\nu = 1/3$, the exact tip correction factor is given by

$$\alpha_{\text{tip}} = \left(1 - \rho_{\text{in}}^{2/3}\right)^{-3}, \quad (3.50)$$

while the perturbation theory yields

$$\alpha_{\text{tip}} = 1 + \frac{6}{(2\pi(1 + \nu))^{1/3}} \cdot \alpha(\nu)^{1/3} \rho_{\text{in}}^{2/3}. \quad (3.51)$$

As stated above, the exact tip correction factor α_{tip} is only known for $\nu = 1/3$. However, the evaluation of equation (3.51) for different values of the Poisson's ratio ν shows that the tip correction factor α_{tip} is almost independent of ν . This result is illustrated by figure 3.10, where the approximative results for $\nu = 0.165$, $\nu = 1/3$ and $\nu = 0.5$ are shown together with the exact result for $\nu = 1/3$. It can be seen that for an indenter size as small as $\rho_{\text{in}} = 0.05$ the tip correction factor α_{tip} calculated by perturbation theory is already underestimated by 10% compared to the exact calculation. On the other hand, the relative difference between the tip correction factors calculated by perturbation theory for $\nu = 1/3$ and $\nu = 0.5$ at $\rho_{\text{in}} = 0.35$ is only 0.45% and the relative difference between $\nu = 0.165$ and $\nu = 0.5$ at $\rho_{\text{in}} = 0.35$ is only 0.06%. At smaller values of ρ_{in} , the relative errors are even smaller. These results suggest that for any value of ν , the tip correction factor can be approximated as

$$\alpha_{\text{tip}}(\rho_{\text{in}}, \nu) \approx \alpha_{\text{tip}}(\rho_{\text{in}}, \nu = 1/3) \quad (3.52)$$

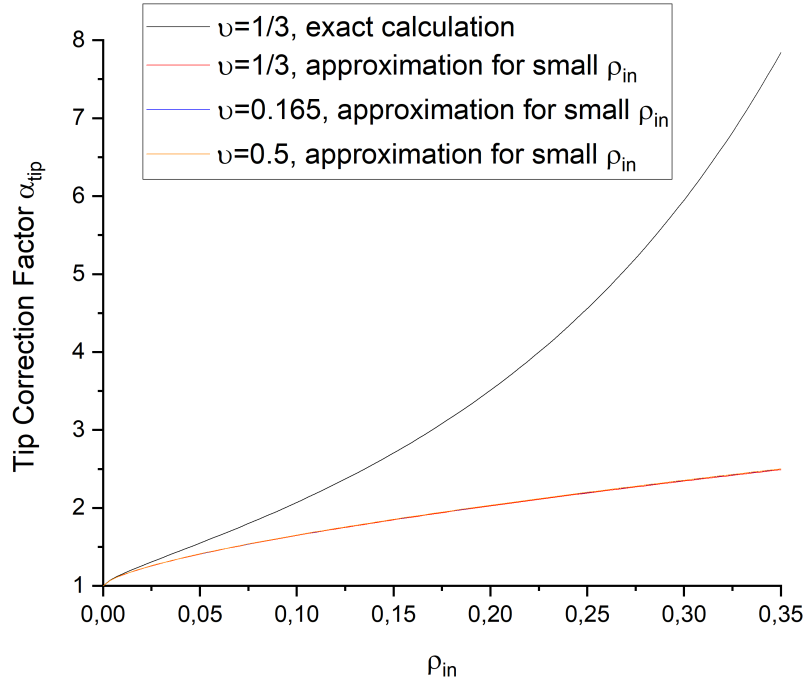


Figure 3.10.: Comparison of the exact solution for α_{tip} as a function of the indenter radius ρ_{in} with the results achieved by perturbation theory. The three latter results almost coincide and cannot be distinguished by their graphs.

which shall be abbreviated as $\alpha_{tip}(\rho_{in})$ in the following. Of course, it is not certain if the results in the exact calculation are as robust against changes of the Poisson's ratio ν as the results achieved by perturbation theory. However, it is safe to assume that the indenter size ρ_{in} is by far the dominant parameter for the determination of α_{tip} . Therefore, it is much better to employ the exact solution for the tip correction factor α_{tip} and to neglect the Poisson's ratio ν than to employ the tip correction factor achieved by perturbation theory.

As a conclusion of the above results, it can be stated that the best approxi-

mation for the general case of the large deflection limit is given by the product of equations (3.44) and the tip correction factor $\alpha_{\text{tip}}(\rho_{\text{in}})$:

$$\tilde{F} = \alpha(\nu) \left(1 - \rho_{\text{in}}^{2/3}\right)^{-3} \tilde{\delta}^3 \quad (3.53)$$

or put in non-dimensionless terms

$$F = \alpha(\nu) \left(1 - \left(\frac{r_{\text{indenter}}}{r}\right)^{2/3}\right)^{-3} \frac{Et}{r^2} h^3. \quad (3.54)$$

3.5.2. Small Deflection Limit

In the limit of small indentations, $\tilde{\delta} \ll 1$, the two cases of point indentation and finite indenter size behave fundamentally different. Vella and Davidovitch find that the case of point indentation leads to a nonlinear behavior, where the dimensionless deflection is described as

$$\tilde{\delta} = \frac{\tilde{F}}{2\pi} \ln(8\pi/\tilde{F}). \quad (3.55)$$

With a finite indenter size, the force-deflection relationship can be derived under the assumption that the stress in the deflected membrane is approximately unchanged by the indentation, i.e. $\sigma \approx \sigma_0$. In this case, the force-deflection relationship is given by [53]

$$\tilde{F} = \frac{2\pi}{\ln(1/\rho_{\text{in}})} \tilde{\delta}. \quad (3.56)$$

However, depending on ρ_{in} , equation (3.56) is only valid for very small deflections $\tilde{\delta}$. More precisely, there is a function $\tilde{\delta}_*(\rho_{\text{in}})$ such that equation (3.56) only holds if $\tilde{\delta} \leq \tilde{\delta}_*(\rho_{\text{in}})$. Moreover, with decreasing indenter size, equation (3.56) holds for ever smaller deflections, i.e. $\tilde{\delta}_*(\rho_{\text{in}}) \rightarrow 0$ as $\rho_{\text{in}} \rightarrow 0$. Under experimental conditions however, where the indenter size ρ_{in} is significantly greater than zero, equation (3.56) is the best way to describe the linear regime

3. Theory of Bulge Test and Nanoindentation

of the membranes response to the deflecting force. In [53], its non-dimensionless form

$$F = \frac{2\pi\sigma_0 t}{\ln(1/\rho_{in})} h \quad (3.57)$$

was used to determine the initial tension of many different materials via force-deflection measurements.

3.5.3. Intermediate Range

Equations (3.53) and (3.56) give a force-deflection relationship of the large respectively small deflection limit which is valid for any indenter size ρ_{in} . In order to gain a general force-deflection relationship for all deflections, it is common to add the small and the large deflection limit, as it was done to describe the Bulge Test,

$$\tilde{F}_{sum} = \frac{2\pi}{\ln(1/\rho_{in})} \tilde{\delta} + \alpha(\nu) \cdot \alpha_{tip}(\rho_{in}) \tilde{\delta}^3. \quad (3.58)$$

Since it is not feasible to give a general description of the behavior of a membrane subjected to an indentation, this sum of the limits approach will be pursued here as well. However, one should be aware that in the case of nanoindentation, the error induced by this approach is significantly larger than in the case of the Bulge Test.

Vella and Davidovich analyze the relative error due to the sum approach for $\nu = 1/3$ and $\rho_{in} = 10^{-2}$, $\rho_{in} = 10^{-3}$ and $\rho_{in} = 10^{-4}$ by comparing the sum formula to the numerically determined exact solution. The results are shown in figure 3.11(a). It can be seen that for $\rho_{in} = 10^{-4}$, the relative error in the intermediate regime can reach up to 50%. Moreover, the error is very large for a broad range of $\tilde{\delta}$. However, the error can be reduced by using a relatively large indenter, $\rho_{in} \geq 0.01$. This finding may seem surprising but it can be explained the fact equation (3.56) becomes accurate for a greater range

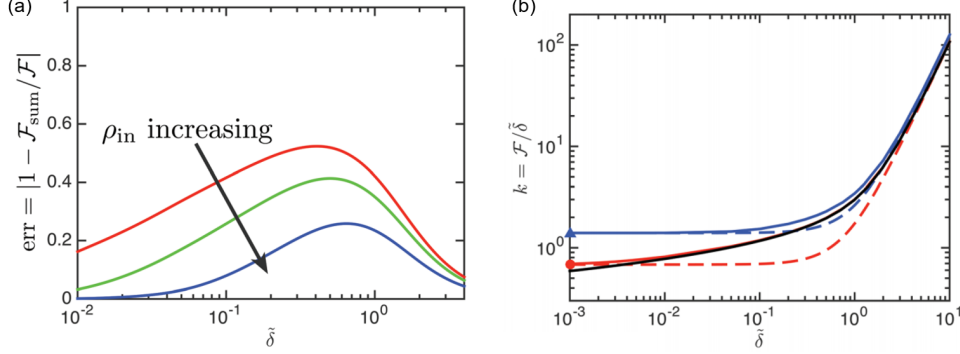


Figure 3.11.: Results of the numerically determined force indentation curves in [13] achieved for $\nu = 1/3$. (a) The relative error of the sum of the limits approximation as a function of $\tilde{\delta}$ for $\rho_{\text{in}} = 10^{-4}$ (red), $\rho_{\text{in}} = 10^{-3}$ (green) and $\rho_{\text{in}} = 10^{-2}$ (blue). (b) Comparison of the stiffness $k = \tilde{F}/\tilde{\delta}$ according to numerical calculation (solid curves) with the sum approximation \tilde{F}_{sum} (dashed curves). Black indicates a point indenter, red indicates $\rho_{\text{in}} = 10^{-4}$ and blue indicates $\rho_{\text{in}} = 10^{-2}$. Reproduced with permission.

of deflections when the indenter size increases. The approach to utilize a large indenter was chosen here and will be discussed in detail in section 6.1. Figure 3.11(b) shows an interesting property of the sum of the limits approximation. In the case of indentation, the sum approximation leads to an underestimation of the required force in the intermediate range. This is contrary to the Bulge Test scenario, where the force was slightly overestimated by the sum of the limits formula.

3.5.4. Conclusions

In the case of nanoindentation, the force-deflection relationship cannot be determined as precisely as in the case of the Bulge Test. Nevertheless, when a large indenter with $\rho_{\text{in}} \geq 0.01$ is used, the sum of the limits formula

$$F_{\text{sum}} = \frac{2\pi\sigma_0 t}{\ln(1/\rho_{\text{in}})} h + \alpha(\nu) \left(1 - \rho_{\text{in}}^{2/3}\right)^{-3} \frac{Et}{r^2} h^3 \quad (3.59)$$

3. Theory of Bulge Test and Nanoindentation

gives a satisfying result. It shall be noted that some experimental works, e.g. [34] and [54] use an expression of the form

$$F_{\text{simplified}} = \pi\sigma_0 th + f(\nu)\frac{Et}{r^2}h^3, \quad (3.60)$$

where the relative size of the indenter ρ_{in} is neglected. However, such a simplified expression leads to inaccuracies in the data analysis. More precisely, the omission of the tip correction factor $(1 - \rho_{\text{in}}^{2/3})^{-3}$ of the cubic term leads to the error shown in figure 3.10. This error becomes very large at large indenter sizes. On the other hand, the omission of the logarithmic correction factor $2/\ln(1/\rho_{\text{in}})$ of the linear term leads to an error which becomes very large at small indenter sizes. Therefore, the use of equation (3.59) shall be recommended no matter which indenter size is used.

As it was done for the Bulge Test in the previous section, all assumptions which were needed for equation (3.59) shall now be recapitulated. Five assumptions were used.

- (1) The pressure in the intermediate regime between small deflection limit and large deflection limit is correctly captured by the superposition of the two limits.
- (2) The tip correction factor α_{tip} in the large deflection limit derived for $\nu = 1/3$ can be used for $\nu \neq 1/3$ as well.
- (3) The indenter has a cylindrical shape.
- (4) The strains in the pressurized membrane are infinitesimal.
- (5) The bending stress can be neglected.

In the case of a relatively large indenter, $\rho_{\text{in}} = 0.01$, assumption (1) leads to an underestimation of the required force of up to 20%. This is the main theoretical error of equation (3.59). However, it can be assumed that the error decreases when an even larger indenter is used.

The error induced by assumption (2) cannot be safely quantified. However, figure 3.10 shows that the relative difference between the tip correction factors α_{tip} calculated by perturbation theory for $\nu = 0.165$, $\nu = 1/3$ and $\nu = 0.5$ is negligible. It is therefore a reasonable assumption that the exact tip correction factor for $\nu \neq 1/3$ can be approximated by the tip correction factor for $\nu = 1/3$.

The influence of the shape of the indenter was extensively discussed in [55] in the context of hardness measurements by AFM nanoindentation. In the case of force-deflection measurements, a non cylindrical indenter leads to a relative indenter size which is a function of the indentation depth. When an AFM tip is used as the indenter, the best approximation to its shape is usually a pyramid. In order to adapt equation (3.59) to an AFM tip, the pyramid can be approximated by a cone. Then, equation (3.59) can be modified by using a relative indenter size according to the deflection height dependent contact area of the tip with the membrane. However, when an AFM tip is used to measure multiple membranes, the radius of its contact area will increase by time. Hence, the tip size can only be approximated. In practice, the uncertainty of the tip size is much larger than the change in the contact radius induced by different deflection heights. Therefore, it is reasonable to neglect the shape of the indenter. The determination of the tip size will be discussed in more detail in chapter 6.

Since the theoretical description of the nanoindentation experiment is more complex than the Bulge Test, there is no study on the influence of finite strains. However, it seems reasonable that error due to assumption (4) is similar to the same error in the case of the Bulge Test which was shown in figure 3.8(b) for three different pressures. Hence it can be assumed that the error of the deflection h as a function of the force F_{sum} is in the range of $\pm 1\%$. Put as the error of the force as a function of the deflection height this implies an error of $\pm 3\%$.

The bending stiffness can be treated in the same way as in the case of the Bulge Test. Assuming $\rho_{\text{in}} \ll 1$, the force-deflection relationship in the plate

3. Theory of Bulge Test and Nanoindentation

regime, i.e. when the bending stiffness is the dominant term, is [35, 54]

$$F_{\text{bending}} = \frac{4\pi t^3 E}{3(1-\nu^2)r^2} h. \quad (3.61)$$

If necessary, this term can be added to equation (3.59) to obtain the force-deflection relationship for thick membranes.

$$F_{\text{sum}} = \left(\frac{2\pi\sigma_0 t}{\ln(1/\rho_{\text{in}})} + \frac{4\pi t^3 E}{3(1-\nu^2)r^2} \right) h + \alpha(\nu) \left(1 - \rho_{\text{in}}^{2/3}\right)^{-3} \frac{Et}{r^2} h^3. \quad (3.62)$$

However, in the same way as for the Bulge Test, the relationship of the force attributed to the bending stiffness scales with the factor t^2/h^2 compared to the force attributed to the large deflection limit. In the case of CNMs, the error induced through omission of the bending stiffness is again less than 0.1%. Therefore, it can be neglected in the evaluation of nanoindentation experiments as well.

As a conclusion of the above results, it can be said that for a relative indenter size of $\rho_{\text{in}} = 0.01$, the maximal error of the force F needed to achieve a certain deflection h in equation (3.59) can be estimated to be +5%/−25%. However, extrapolating the trend in figure 3.11(a), it seems reasonable to assume that a large indenter size in the range of $0.01 \leq \rho_{\text{in}} \leq 0.1$ leads to a further reduction of the error. Therefore, equation (3.59) is a good compromise between the precision of the theoretical description and the practical feasibility of the data evaluation.

3.6. 2D modulus

When the Young's modulus or the initial tension of thin membranes are investigated via Bulge Test or nanoindentation, the data analysis requires the

knowledge of the exact membrane thickness. However, the determination of the thickness of 2D materials is a very difficult task. In [20], the thickness of CNMs was investigated by Scanning Transmission Ion Microscopy (STIM), X-ray Photoelectron Spectroscopy (XPS) and Energy Filtered Transmission Electron Microscope (EFTEM). The thickness of TPT-CNMs was determined to be 1.2 nm before the transfer process and 2.1 nm to 2.2 nm afterwards. The reason for this effect is that the transfer process may leave organic residues on the membrane which lead to an increased thickness. This also implies that the membrane thickness may vary from membrane to membrane.

The thickness of graphene is often assumed to be the graphite interlayer distance of $d = 0.335$ nm [56]. The experimentally determined thickness of mechanically exfoliated graphene ranges from 0.4 nm to 1.2 nm [57]. For CVD graphene, which is used in the present work, a thickness of 1 nm was reported [58]. However, it has to be kept in mind that the graphene membranes used here need to be transferred before investigation which leads to a further increase of the membrane thickness.

The determination of the Young's modulus and initial tension using the equations (3.26) and (3.59) requires the knowledge of the membrane thickness. Therefore, the uncertainty about the membrane thickness causes an uncertainty in the determination of the Young's modulus and the initial tension.

For this reason, it is useful to define the two dimensional Young's modulus E_{2D} and the two dimensional initial tension σ_{2D}^0 as

$$E_{2D} = Et \tag{3.63}$$

and

$$\sigma_{2D}^0 = \sigma_0 t \tag{3.64}$$

Both, 2D modulus and 2D initial tension can be determined by Bulge Test and nanoindentation experiments without the knowledge of the membrane

3. Theory of Bulge Test and Nanoindentation

thickness. Moreover, since the resistance of the membrane against pressure or force is proportional to its thickness, these quantities reflect the membranes response to the applied pressure or force. Therefore, it is natural to put the main focus on the 2D modulus and the 2D initial tension when Bulge Test and nanoindentation experiments are conducted.

4. Methods

4.1. Atomic Force Microscopy (AFM)

The atomic force microscope (AFM) is a scanning probe microscope (SPM) which is based on the interaction of a sharp tip with the investigated sample. It was invented in 1985/86 by Gerd Binnig, Calvin Quate and Christoph Gerber at IBM. Under perfect conditions, the AFM can reach atomic resolution [59, 60]. In general, the AFM consists of a sharp tip which is mounted on an elastic cantilever. A focused laser beam is aligned onto the cantilever and reflected into a photo detector. During the scanning process, the cantilever bends due to the interactions of the tip with the sample. The long ranged attractive forces consist of the Van der Waals forces and capillary forces which scale with the sixth power of the distance r^6 between tip and a solid sample. The short ranged repulsive forces are due to the Pauli exclusion principle and Coulomb interactions. The simplest way to describe the overlap of both attractive and repulsive forces between the tip and a solid sample is by the Lennard-Jones potential

$$V(r) = \frac{C_1}{r^{12}} - \frac{C_2}{r^6}, \quad (4.1)$$

where the constants C_1 and C_2 depend on the properties of tip and sample.

The deflection of the cantilever is measured by the position of the laser beam on the photo detector and is used as a measure of the attractive or repulsive force between sample and tip. There are three main operating modes of the

AFM [61]:

1. In contact mode, the tip is kept in a repulsive interaction with the sample. The most common operation mode is the constant force mode. In this mode, the cantilever is bent to a preset set point and the height of the cantilever is constantly adjusted such that the set point is maintained. This causes the tip to follow the topography of the sample. In the more seldom used constant height mode, the cantilever is kept at a constant height independent of the sample and the amount of the repulsive force is used as a measure of the sample topography. In order to avoid damaging the sample due to the constant scratching, contact mode requires cantilevers with a soft spring constant of around 0.1 N/m [62].

2. In intermittent contact mode (usually referred to as tapping mode), the cantilever is excited to oscillate at or near its fundamental resonance frequency. The feedback parameter is the amplitude of the oscillation. When the tip approaches the sample, it periodically touches the surface which leads to a decrease in the amplitude. The height of the cantilever is permanently adjusted such that the oscillation amplitude is kept at the set point. This reveals again the topography of the sample. Tapping mode cantilevers usually have a spring constant of around 10 N/m.

3. In non-contact mode, the cantilever oscillates at a small distance, usually in the Å or nm range, from the sample. There are again two modes of operation. In the amplitude modulation, the force between sample and tip is measured by a change in the amplitude of the oscillation. In the frequency modulation, the force between sample and tip is measured by a change in frequency. Non-contact mode cantilevers usually have a spring constant of around 40 N/m.

In the present work, contact mode and tapping mode were used. All experiments were conducted on a NT-MDT NTEGRA PNL system equipped with the software Nova 1324. The deflection of the cantilever was measured through an electric signal in the photo detector in the unit of nA. The height of the sample was adjusted by a piezo tube in the sample stage. The images were processed with Gwyddion 2.55.

4.1.1. Force Curve

The AFM cannot only be used to image a sample by scanning but it also provides the possibility to analyze the properties of single positions of the sample via spectroscopy. This is achieved by a force curve. To this end, the tip is retracted from the sample and then pressed against it until a preset force is reached (load). Subsequently, it is retracted again until the starting height is reached. For both curves, load and unload, a cantilever deflection vs. cantilever height diagram is recorded. From the cantilever deflection, the force between sample and tip can be calculated. An exemplary force curve on a three layer CVD graphene membrane is shown in figure 4.1.

Force curves are usually performed in contact mode, but also possible in tapping mode. They are a common tool to conduct nanoindentation experiments [63].

4.1.2. AFM Bulge Test and Nanoindentation

The AFM can be used to conduct both Bulge Test and nanoindentation experiments. With the right setup, both experiments can be performed subsequently. This is a great advantage of the AFM compared to other Bulge Testing and nanoindentation methods. More details about the experimental aspects of Bulge Test and nanoindentation are given in chapter 5.

4.2. Helium Ion Microscopy (HIM)

The helium ion microscope (HIM) is a focused ion beam (FIB) system which uses the noble gas helium for imaging. To this end, a focused beam of helium ions scans over the sample. When hitting the sample, the helium ions generate secondary electrons. These secondary electrons are detected and used to generate an image of the sample with a resolution of up to 0.25 nm [64, 65]. When the sample is insulating, it will charge due to the deposition of the ions. This

4. Methods

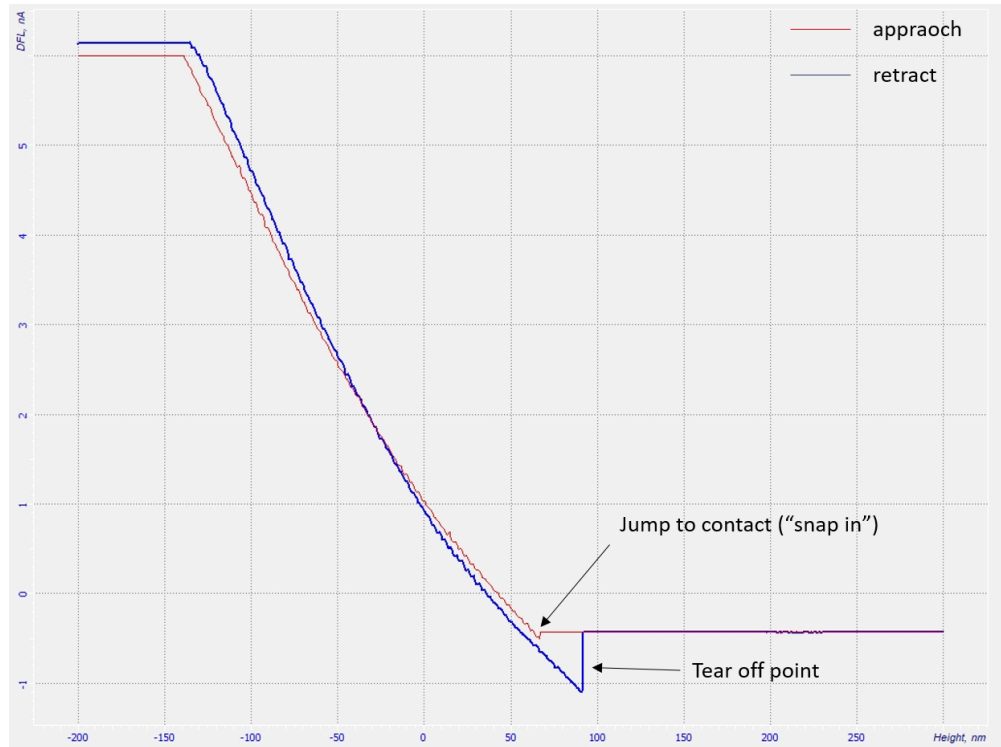


Figure 4.1.: Image of a force curve performed on a three layer CVD graphene membrane. When the target deflection signal of 6 nA was reached at the height of -130 nm, there was no further lowering of the cantilever. Due to the attractive forces between the sample and the tip, the tip jumps into contact with the membrane from a distance of 5 to 10 nm. For the same reason, the membrane is significantly pulled up during the unload process before it loses contact to the tip.

positive charging can be compensated with an electron flood gun [66]. For the imaging of very thin samples such as for example CNMs, it is often advantageous to operate the HIM in transmission mode. In this mode, the secondary electrons are generated by a polished metal surface below the sample instead of the sample itself [67]. A detailed description of helium ion microscopy is given

in [68].

HIM images were recorded on a Orion Plus helium ion microscope from Zeiss by Michael Westphal and Daniel Emmrich.

4.3. X-ray Photoelectron Spectroscopy (XPS)

X-ray photoelectron spectroscopy is a tool to identify the chemical composition of a thin film by analyzing the binding energy of its electrons. XPS is based on the photoelectric effect. The sample is irradiated with monochromatic X-rays which leads to the emission of photo electrons. The kinetic energy of the emitted photo electrons E_k is measured by a hemispherical analyzer. The electron binding energy E_b is calculated as [69]

$$E_b = h\nu - E_k - \Phi, \quad (4.2)$$

where $h\nu$ is the energy of the irradiating photons and Φ is the work function of the spectrometer. The intensity of electrons is measured as a function of the binding energy. Each peak in the spectrum can be associated with an element and its chemical configuration [70]. The occurrence of the element associated with the peak can be quantified by the intensity of the peak.

XPS can also be used to determine the thickness of a thin film. To that end, the intensity of a peak associated with the substrate of the film is compared to the intensity of the same peak from a reference sample. Electrons can only contribute to the characteristic peak in the spectrum if they did not undergo an inelastic collision before leaving the sample and reaching the vacuum. The intensity of contributing electrons as a function of the depth d of their emission is given by the Beer-Lambert relationship [69]

$$I = I_0 \exp[-d/(\lambda_{\text{IMFP}} \cos \theta)], \quad (4.3)$$

where the inelastic mean free path λ_{IMFP} describes the average distance after

which the number of electrons without inelastic collision reduced to $1/e$ of the original value. The inelastic path depends on the investigated sample. For BPT- and TPT-CNMs, it was estimated to be $\lambda_{\text{IMFP}} = 32 \text{ \AA}$ [71]. The tilt angle of the sample is denoted by θ . Since CNMs usually have a gold substrate, comparison of the $Au4f_{7/2}$ peak of the CNM with the same peak of a sputtered gold sample yields the of the CNM.

4.4. Sader Method for the Determination of the Spring Constant of the Cantilever

The Sader method [72] is a technique to determine the spring constant of rectangular cantilevers. It is valid for cantilevers with $L \gg b \gg t$, where L , b and t are the cantilevers length, width and thickness, respectively. For standard cantilevers, this condition is usually satisfied. The Sader method is based on two observations. Firstly, the spring constant of a cantilever can be calculated by

$$k = 0.2427\rho_c Lbt \cdot \omega_{\text{vac}}^2, \quad (4.4)$$

where ρ_c is the mass density of the cantilever. However, since the thickness of a cantilever is hard to determine, equation (4.4) by itself is not very helpful for the cantilever calibration. The second observation is that there is a frequency shift between the fundamental resonance frequency in vacuum ω_{vac} and the fundamental resonance frequency in a fluid ω_f . Both frequencies are related by

$$\omega_{\text{vac}} = \omega_f \left(1 + \frac{\pi\rho_f b}{4\rho_c t} \Gamma_r(\omega_f) \right)^{1/2}, \quad (4.5)$$

where ρ_f is the mass density of the fluid. The product $\rho_c t$ is the areal mass

4.4. Sader Method for the Determination of the Spring Constant of the Cantilever

density of the cantilever and is given by

$$\rho_c t = \frac{\pi \rho_f b}{4} (Q_f \Gamma_i(\omega_f) - \Gamma_r(\omega_f)) \quad (4.6)$$

Γ_r and Γ_i denote the real and the imaginary part of the hydrodynamic function Γ which describes the total hydrodynamic force per unit length normalized by the force per unit length required to excite a cylindrical beam with an identical cross section as the cantilever beam to the same amplitude and frequency [73]. A detailed derivation of the hydrodynamic function can be found in [74]. Q_f denotes the quality factor of the cantilever in the fluid. Equation (4.6) is valid for $Q_f \gg 1$ which is usually satisfied when the measurements are performed in air.

Substitution of equation (4.5) and (4.6) into equation (4.4) yields

$$k = 0.1906 \rho_f b^2 L Q_f \Gamma_i(\omega_f) \omega_f^2 \quad (4.7)$$

which can be used for the cantilever calibration. A remarkable feature of equation (4.7) is that the cantilever thickness is not needed for its calibration. Moreover, the determination of ω_f and Q_f are performed in the fluid, for example in air. Therefore, no properties of the cantilever in vacuum are required.

Cantilevers were calibrated with the mathematica notebook provided in [75]. Length and width of the cantilever were determined in an optical microscope (Olympus BX51 equipped with an Olympus C-5060 camera). The fundamental resonance frequency of the cantilever was determined in the AFM. The quality factor was calculated by $q = f/\Delta f$, where Δf is the full width of the peak at the maximum amplitude divided by $\sqrt{2}$ [76].

5. Experimental

5.1. Sample Preparation

5.1.1. SAM Preparation

SAMs were prepared from solution. To this end, a substrate of 300nm Au(111) on mica (from Georg Albert Physical vapor Deposition) was cleaned in an ozone cleaner (UVOH 150 LAB by FHR Anlagenbau) for 3 minutes in order to remove organic contamination from the substrate. Subsequently, the substrate was rinsed with ethanol and blown dry with nitrogen.

The flask was cleaned with piranha solution (7 parts of H₂SO₄ with 3 parts of H₂O₂). The substrate was immersed into 10 ml of dry and degassed N,N-dimethylformamide (DMF) and a small amount of TPT molecules was added. The flask was put under a nitrogen atmosphere and sealed. After that it was heated to 70 °C and left for 24 h under constant stirring. After the formation of the SAM, samples were taken out of the flask, rinsed with DMF and ethanol and blown dry with nitrogen. The samples were stored under argon atmosphere.

TPT-CNMs from SAMs grown on silver were prepared by Linh Le Hoang and ODT-CNMs were prepared by Raphael Dalpke.

5.1.2. Electron Irradiation

The formation of CNMs was achieved by electron induced cross linking in a home built floodgun. To this end, the SAMs were mounted onto a sample stage, contacted with clamps and put into high vacuum $p < 3 \cdot 10^{-7}$ mbar. The

irradiation took place at an electron energy of 100 eV. In [77], the effect of the electron dose was investigated by measuring the Young's modulus of samples which were irradiated with different electron doses. The Young's modulus increases with the electron dose and shows a saturation at 50 mC/cm². From this result it was concluded that the cross linking shows a saturation at 50 mC/cm², too. Therefore, the SAMs in the present work were irradiated with a dose of 50 mC/cm².

5.1.3. Sample Transfer

Bulge Test and nanoindentation experiments require freestanding samples. To this end, samples were transferred onto a Si₃N₄/Si substrate with a circular hole in the center (Silson Ltd.). A schematic illustration of the sample on the substrate is shown in figure 5.1.

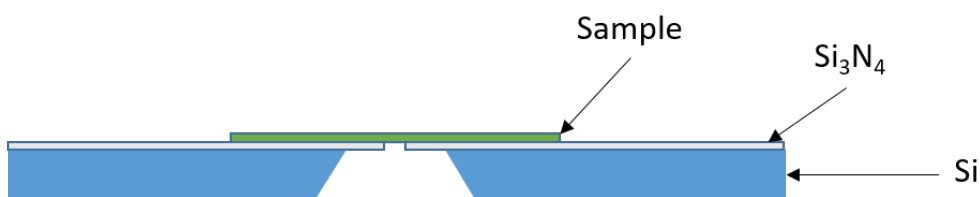


Figure 5.1.: Schematic diagram of the sample on the Si₃N₄/Si substrate after the transfer. The substrate consists of 500 nm of silicon nitride on top of 200 μ m of silicon. Over the small circular hole of the silicon nitride layer, the sample is freestanding.

The transfer of the CNMs onto the Si₃N₄/Si substrate was achieved in the following way. First, a protective double layer of Polymethyl methacrylate (PMMA) was spin coated onto the CNM on the gold on mica substrate. Two different photoresists were used: PMMA 50K (AR-P 639.04) and PMMA 950K (AR-P 679.04, Allresist GmbH; 50K respectively 950K refer to the molar mass) solved in n-butyl acetate ethyl lactate. Each resist was spin coated for thirty seconds at 4000 revolutions per minute. After each spin coating step, the

sample was annealed to 90 °C for five minutes in order to evaporate the solvent. Secondly, the CNM on gold, stabilized by PMMA, was detached from the mica substrate. To this end, the edges of sample were narrowly cut. Subsequently, the sample was placed on top of an iodine solution with the relation of 1:4:40 I₂ : KI : H₂O by weight for 10 minutes in order to etch the gold at the edge of the sample. Then the gold was separated from the mica by repeatedly carefully dipping the sample into millipore water. When the mica substrate was completely detached, the gold/CNM/PMMA sample was left floating on the water surface. The sample was transferred back onto the iodine solution with the help of a silicon wafer piece. When the gold was completely dissolved, the sample was transferred onto millipore water for one minute and then onto potassium iodide dissolved in water (1:10 by weight) for 10 minutes in order to dissolve iodine residues. The CNM/PMMA sample was again washed on a fresh millipore water surface. From this surface, it was carefully caught with the target Si₃N₄/Si substrate. The sample was dried by annealing to 50 °C for 15 minutes.

5.1.4. Critical Point Drying

After the sample transfer, the protective PMMA layer was removed in a critical point dryer (autosamdri-815, Tousimis Research Corporation). To this end, the sample was placed in a chamber which was then carefully filled with acetone. After waiting for one hour, the acetone was slowly replaced by CO₂ (UN 1013, Linde AG) at the critical point of liquid and gas. Subsequently, the CO₂ was released in the gas phase. The advantage of this procedure is that the capillary forces are avoided which would occur if the liquid acetone was removed.

5.1.5. CVD Graphene

For this experiment, CVD graphene prepared on copper was used which was supplied by Duisburg University. In order to perform Bulge Test and nanoin-

5. Experimental

dentation experiments, the graphene was transferred from the copper foil to a $\text{Si}_3\text{N}_4/\text{Si}$ substrate with a hole of a well defined size over which the graphene is free standing after the transfer.

The transfer process was performed according to the protocol of Annika Willunat [78] with only some slight modifications. First, a protective double layer of PMMA was spin coated onto the graphene on the top side of the copper. To that end, the copper foil was taped onto a heat resistant copy foil in order to avoid PMMA on the sides and on the back of the sample. This is necessary since a PMMA on the back side would disturb the etching process in the next steps. The PMMA was spin coated in the same way as described above for CNMs. Due to the vapor deposition there is also a graphene layer on the back side of the copper foil. Before the copper can be etched, this back-side graphene has to be removed. To that end, the sample was treated for 45 seconds with an O_2 -plasma etch which operates at 0.1 mbar, 25 to 40 keV, 1 mA and 500 Hz. The plasma dose was kept as low as possible as the plasma also slowly removes the protective PMMA layer. Thus, an unnecessary long exposure to the plasma increases the likelihood of creating defects during the transfer process. The copper was etched in an ammonium persulfate solution (3.5 g $(\text{NH}_4)_2\text{S}_2\text{O}_8$ per 100 ml H_2O) for about one day. To remove the copper residuals, the graphene/PMMA sample was first transferred into distilled water for 5 minutes and then into a fresh ammonium persulfate solution for 2 hours. In order to avoid mechanical damage of the sample through contact with the SiO_2/Si transfer substrate, a thin water layer was kept between sample and substrate during the transfer steps. To that end, the substrate is treated in the UV/ozone-cleaner for 3 minutes which makes it hydrophilic. Then the swimming sample was caught by positioning the transfer substrate under the sample and carefully lifted up. After the copper was fully etched, the sample was transferred into distilled water again for washing away the ammonium persulfate. Then it was transferred into another beaker of distilled water, where it was caught with the target substrate. In the case of single layer graphene,

the $\text{Si}_3\text{N}_4/\text{Si}$ substrate was used to catch the graphene/PMMA sample in the same horizontal way as with the transfer substrate. To avoid water enclosures, the sample was baked at 50 °C for one day. For the preparation of multi layer graphene, the graphene/PMMA was carefully caught with another copper/graphene foil. This yields a sample consisting of two layers of graphene on copper. As above, the sample was baked at 50 °C for one day. The whole transfer process was then repeated. When the desired number of layers was reached, there was a final transfer onto the $\text{Si}_3\text{N}_4/\text{Si}$ substrate as described above. In the end, the PMMA was dissolved in acetone in the critical point drier in the same way as for CNMs.

After preparation, all membranes were investigated in an optical microscope (Olympus BX51 equipped with a Olympus C-5060 camera) in order to verify their quality.

5.2. Execution of Bulge Test and Nanoindentation

5.2.1. Cantilever Choice

In order to precisely determine the membrane's deflection, Bulge Test experiments need to be performed in contact mode. The same is true for nanoindentation experiments. However, before the start of the experiment, the central point of the membrane needs to be determined. In order to minimize the risk of rupturing the membrane, this is best done in tapping mode. Since it is not possible to change the cantilever between the scan and the experiments, the cantilever needs to be suited for all these applications. As described in chapter 4, this requires a compromise in the choice of the spring constant. However, since Bulge Test and nanoindentation are spectroscopic methods, they have different requirements for the spring constant than an image in contact mode. The cantilever's spring constant for nanoindentation should be roughly in the same range or one order of magnitude smaller than the 2D modulus of the material

under investigation. The Bulge Test can be executed with any spring constant. Therefore, cantilevers with a spring constant of 6.3 to 9.3 N/m (All-In-One-Al, Budget Sensors) were chosen for the experiments. The cantilevers were calibrated with the Sader method. The fundamental resonance frequency of the cantilevers was in the range of 128 N/m to 150 N/m and the quality factor was between 250 and 395.

5.2.2. Substrate and Optimal Membrane Diameter

Si₃N₄/Si substrates are available with different hole sizes, for example ca. 4.5 μm or ca. 16 μm. Depending on the type of membrane and experiment, substrates with the small hole diameter or substrates with the larger hole diameter are suited best for the experiments. In general, small membranes have a better yield of intact membranes after the transfer process and particularly the critical point drying. For example, single layer CVD graphene was only possible to prepare when the membrane diameter was 5 μm or smaller. But also TPT and ODT membranes have a better yield when the membrane diameter is small. On the other hand, when the membranes are small, the relative uncertainties in the experiment are larger as it will be shown in section 6.4. This effect is particularly large in the case of the nanoindentation experiment, but it also exists for the Bulge Test.

There is however one exception to this rule. A larger relative indenter size allows a better theoretical description of the nanoindentation experiment as discussed in chapter 3. Therefore, when the theoretical uncertainty is the limiting factor in the precision of the results, a small membrane radius is favorable. But since in the present experiments, the experimental uncertainties were much larger than the theoretical uncertainties, a membrane diameter of 16 μm is best. Therefore, hole sizes were chosen preferably large under the condition that the membrane was stable enough to be transferred onto the substrate with a good yield.

5.2.3. Experimental Setup

In order to perform Bulge Test experiments, a controllable pressure difference is required. To this end, the sample was mounted on a home built pressure cell, where the pressure difference was achieved by a uniform nitrogen flow. The pressurized nitrogen was provided by a gas cylinder (Linde Gas) and the pressure difference was controlled via the valve of the gas cylinder. The pressure was detected with a pressure transducer (HCX001D6V, Sensortechncis) which gives a voltage as the output signal. The voltage was measured with a digital multimeter (VC840, Voltcraft). Each increment of 1 mV corresponds to a pressure difference of 25 Pa. A schematic diagram of the experimental setup is shown in figure 5.2(a). Each sample was glued onto a plexiglass holder using epoxy glue. The edges of the sample were tightly sealed in order to avoid a nitrogen leakage. The plexiglass holder with the sample was screwed onto the pressure cell. An image of a sample mounted onto the sample holder is shown in figure 5.2(b). The holder was connected to the nitrogen tubes and mounted into the AFM. The carbon tape on the left side of figure 5.2(b) was used to ground the sample to the potential of the AFM when nonconductive samples were investigated.

For both, imaging of the samples as well as Bulge Test and nanoindentation experiments, the sense height signal of the AFM was used. The signal was calibrated with a grating set (Calibration grating set TGS1, NT-MDT) by Christopher David Kaiser.

5.2.4. Determination of the Central Point of the Membrane

For Bulge Test and nanoindentation experiments it is crucial to know the central point of the membrane. The most precise way for its determination is by taking an image of the membrane. However, except for multi layer samples of graphene, this involves a high risk of rupturing the membrane and was therefore avoided. Instead, the membrane was imaged in tapping mode from bottom to

5. Experimental

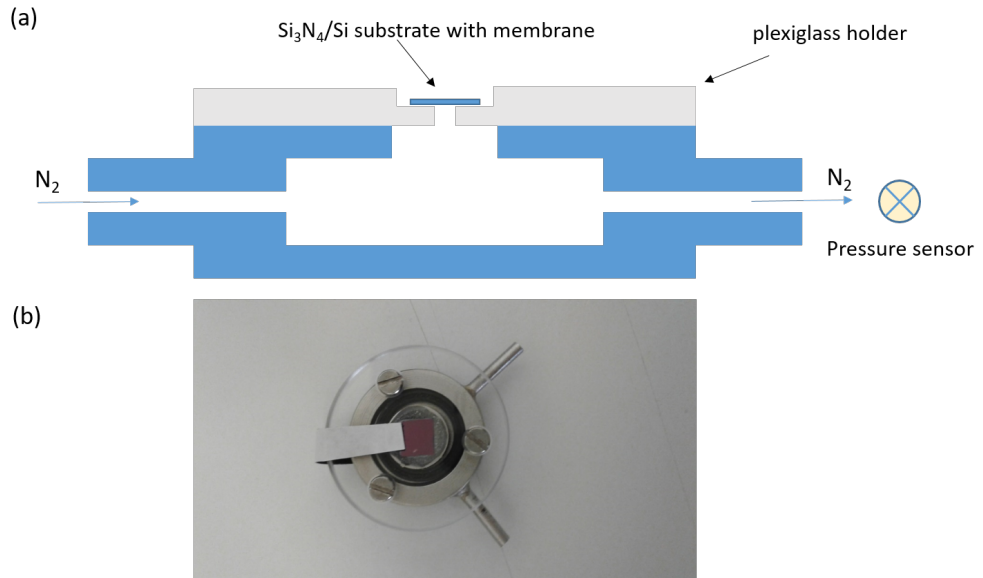


Figure 5.2.: (a) Schematic drawing of the experimental setup used for the Bulge Test and nanoindentation experiments. (b) Image of a sample mounted on the sample holder. One of the tubes on the right side was connected to a nitrogen gas cylinder while the second connection leads to a pressure transducer.

top until the edge of the membrane was reached. Then, the scan was stopped manually. A typical image is shown in figure 5.3. Since the diameter of the membrane was already known from the optical microscope, the knowledge of the bottom edge of the membrane was sufficient to determine its central point with an accuracy of 200 nm and the risk of rupturing the membrane was minimized. Depending on the sample, the images were recorded at a feedback gain value of 0.1 to 0.35.

Nanoindentation experiments have a significant risk of damaging the membrane. Therefore, Bulge Test experiments were carried out first.

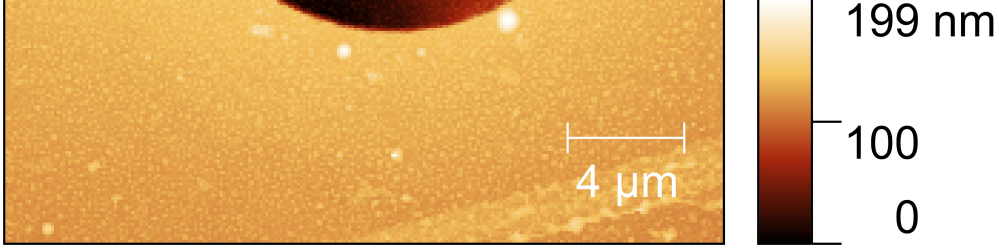


Figure 5.3.: Image of a three layer graphene sample (sample number 6) recorded in tapping mode. The image was stopped when the bottom edge of the membrane was reached.

5.2.5. Execution of the Bulge Test Experiment

When the sample is subjected to a pressure p , not only the membrane deflects but also the part of the Si_3N_4 layer which is not supported by silicon slightly gains in height. Since this effect does not reflect the membrane's properties, the height increase of the Si_3N_4 has to be corrected. Therefore, the membrane deflection in the Bulge Test experiment was determined in the following way. With no applied pressure, the height of the central point $O_{p=0}$ and a reference point $A_{p=0}$ were measured. The difference $D = O_{p=0} - A_{p=0}$ was defined to be the difference corresponding to a deflection of zero. For any applied pressure p , the deflection was determined by the difference

$$h = O_p - A_p - D. \quad (5.1)$$

In this way, the deflection was measured by the height difference between the central point of the membrane and the Si_3N_4 layer. In order to verify the validity of this method, a double layer graphene membrane was scanned in tapping mode at 0 and 10 kPa pressure difference. The images are shown in figure 5.4. The deflection obtained by the right image was in good agreement with the deflection determined by the method explained above. It shall be noted that a tapping mode image of a bulged membrane is only possible with

5. Experimental

very stable membranes such as multi layer graphene. A drawback of these kind of samples is that there are residues from the transfer process caught between the layers which cannot be removed. This will be discussed in more detail in chapter 6.

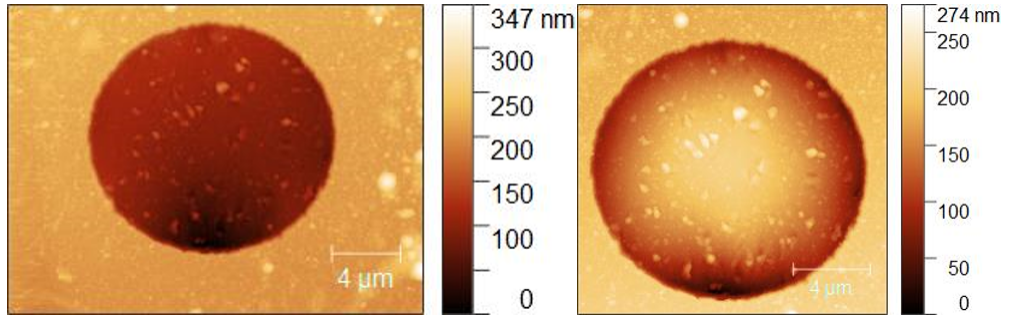


Figure 5.4.: AFM image (tapping mode) of a double layer graphene sample (sample number 3) recorded with no applied pressure (left) and at 10 kPa pressure difference (right).

The principle of the Bulge Test experiment is to adjust the pressure p and then measure both heights O_p and A_p . The so-called load curve is started at $p = 0$ and repeated until the maximum pressure is reached. The unload curve reverses this process. In order to precisely determine the height O_p , it has to be avoided that the membrane is deflected downwards by the tip during the measurement. To this end, the setpoint of the deflection was chosen to be only 0.04 nA above the deflection of the cantilever retracted from the sample. The feedback gain value was reduced to 0.1. Hence, when the tip approached the sample, it exerted almost no force on the membrane and thus the step height of the tip can be neglected. It has to be noted that there is an offset of 0.1 nA in the Nova 1324 software between the deflection setpoint and the true deflection of the cantilever in contact with the sample. For instance, when the setpoint is a deflection value of 0.3 nA, the cantilever deflection in contact is 0.4 nA according to the Nova software. This offset has to be considered when the setpoint is chosen. Moreover, the deflection of the retracted cantilever

slightly changes over time. Therefore, the setpoint was adapted to the current deflection before each height measurement.

The membrane was loaded with increasing pressure until the maximum pressure, which is given by the highest pressure that the membrane can safely withstand, was reached. For TPT, the maximum pressure was calculated assuming that TPT has a similar ultimate tensile strength to BPT obtained in [77]. For all other membranes, the maximum pressure was estimated based on its structure and thickness. When the maximum pressure is reached, it is possible to inverse the whole process and to decrease the load which is applied on the membrane. This is called the unload curve. An example of a load and unload curve is shown in figure 5.5. It can be seen that there is a hysteresis between both curves. After being exposed to a high pressure, the membrane deflects slightly more at a given pressure p , i.e. the membrane is more elastic. If the membrane is loaded again immediately after the first cycle, the increased elasticity persists. However, after a relaxation time of 30 minutes to an hour, the loading curve follows again its original path. Since the unloading curve does not reflect the membrane's original elastic properties, the data of the unloading curve were not considered for the determination of the Young's modulus in the present work. The hysteresis was studied in detail in [77] and [51].

5.2.6. Execution of the Nanoindentation Experiment

The nanoindentation experiment can be conducted after the Bulge Test experiment is finished. In order to investigate the membrane in its relaxed state, a short break between both experiments was taken. The nanoindentation experiment is carried out by recording a force curve at the center of the membrane. In order to acquire more data, it is useful to record multiple subsequent force curves. However, each force curve should be taken at a slightly different position in order to reduce the risk of rupturing the membrane. Therefore, usually five force curves were recorded; one at the central point and four with a distance

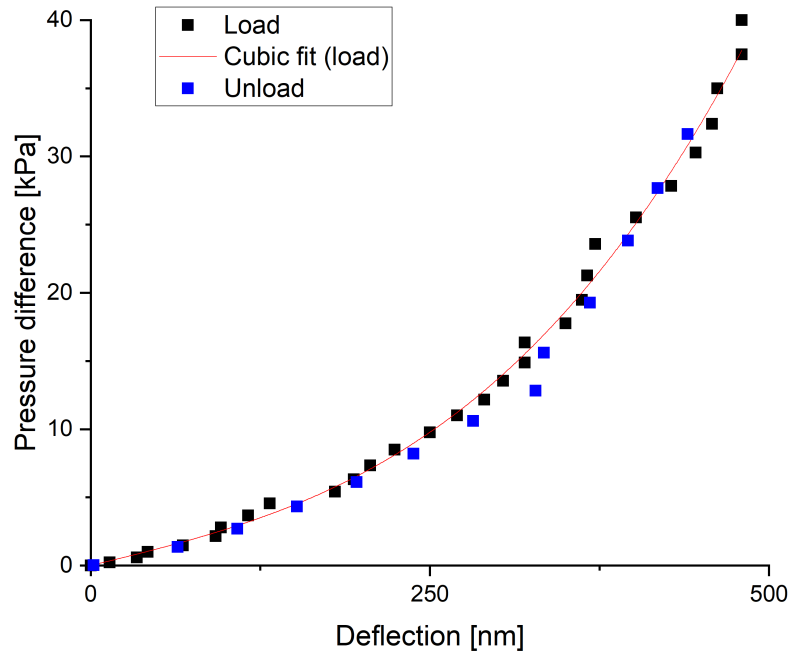


Figure 5.5.: Exemplary load and unload curve of a double layer graphene membrane in a Bulge Test experiment.

of ca. 400 nm from the central point to the left, right, top and bottom.

The data analysis requires a reference force curve in order to calibrate the photo detector output as a function of the bending of the cantilever. This is achieved by a force curve on the $\text{Si}_3\text{N}_4/\text{Si}$ substrate since the substrate does not change its height during the force curve. Therefore, the height change exclusively results in a bending of the cantilever. This reference force curve was recorded at the end of the experiment.

As in the case of the Bulge Test, only the approach curve is considered for the determination of the Young's modulus.

5.2.7. Data Analysis

The Bulge Test experiment yields a pressure vs. deflection curve. The recorded curves were fit with a cubic function of the form $p = k_1h + k_2h^3$, where k_1 and k_2 are the free parameters of the fit. According to formula (3.26),

$$k_1 = \frac{4t\sigma_0}{r^2} \quad (5.2)$$

and

$$k_2 = \frac{K(\nu)Et}{r^4}. \quad (5.3)$$

These fit parameters were used to determine the initial tension and the Young's modulus of the membrane.

The force curve in the nanoindentation experiment yields a photo detector current vs. cantilever height curve. This curve is converted into a force vs. deflection curve with the help of a reference force curve on the rigid substrate. An exemplary reference force curve is shown in figure 5.6. Since the substrate is rigid, the whole height decrease of the cantilever converts into its bending as soon as tip and sample are in contact. Hence, by multiplication with the slope of the fit curve, the photo detector current yields the cantilever bending in nm. Multiplication with the spring constant of the cantilever k gives the force F between tip and sample.

The membrane deflection was obtained from the cantilever height signal in the following way [34]. The equilibrium point $F/k = h = 0$ is the point where the cantilever deflection after contact to the membrane reaches the same value as in retracted state as shown exemplary in figure 5.7. From this point on, the membrane deflection h is calculated from the change in cantilever height $\Delta z = z - z_{\text{equilibrium}}$ by

$$h = \Delta z - F/k. \quad (5.4)$$

This correction is needed due to the fact that a change in cantilever height in

5. Experimental



Figure 5.6.: Reference force curve recorded on the substrate. The slope of the blue curve was used to determine the cantilever bending per change in the photo detector signal.

direction of the membrane leads to the deflection of the membrane but also to an increase in the cantilever bending in the opposite direction of the membrane. Therefore, in order to calculate the membrane deflection, the cantilever bending has to be subtracted from the change in height Δz .

After extracting the force vs. deflection curve, the data was fit with a cubic function of the form $F = k_1h + k_2h^3$ as in the case of the Bulge Test. According

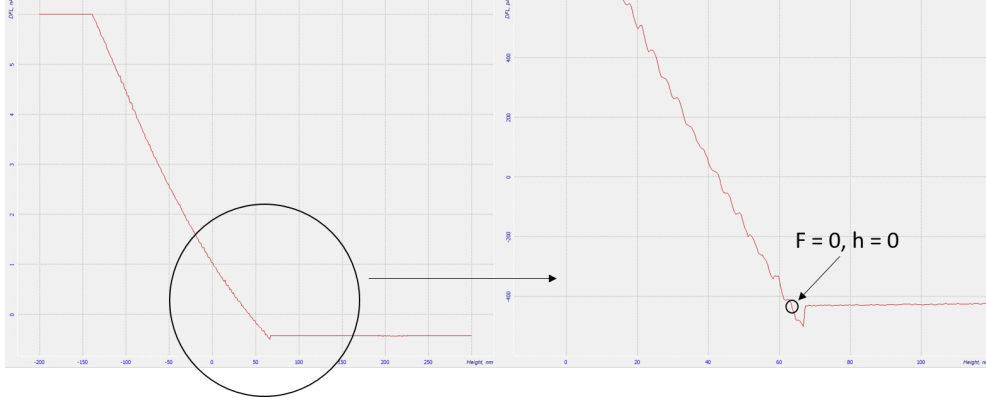


Figure 5.7.: Approach curve from figure 4.1. The right hand side shows a magnification of the area around the snap in point. At the marked point, the cantilever is not bent. Hence the force between tip and sample F as well as the membrane deflection h are equal to zero.

to formula (3.59), k_1 and k_2 are described by

$$k_1 = \frac{2\pi\sigma_0 t}{\ln(1/\rho_{in})} \quad (5.5)$$

and

$$k_2 = \frac{\alpha(\nu)Et}{(1 - \rho_{in}^{2/3})^3 r^2}. \quad (5.6)$$

These fit parameters were again used to determine the initial tension and the Young's modulus of the membrane. The Poisson's ratio was assumed to be $\nu = 0.165$ for graphene [34] and $\nu = 0.35$ for all CNMs [51]. For the data analysis, OriginPro 2019b was used. For unknown reasons, some of the pressure vs. deflection as well as force vs. deflection curves did not satisfy a cubic formula. These data were not considered for the analysis.

6. Results

6.1. Determination of the AFM Tip Radius

As discussed in chapter 3, the analysis of nanoindentation experiments requires the knowledge of the contact area between the AFM tip and the membrane. However, even with the simplifying assumptions discussed above, the determination of the AFM tip size during the experiment is a nontrivial task because the size of the tip changes while it is used. For the experiments of the present work, the AFM tips were typically used for four to eight Bulge Test or nanoindentation experiments. Before each experiment, at least part of the membrane was imaged in tapping mode in order to find the central point of the membrane. Therefore, the AFM tips were in a different condition depending on the amount of time they were already used. As a first approach to estimate the size of the tip, a new cantilever and a used cantilever after its last experiment were imaged by helium ion microscopy. The results are shown in figure 6.1.

It can be seen that the used tip has a larger tip radius by the factor of 30 compared to the new tip. It is not possible to reconstruct the true size of the tip during the experiment. Moreover, it is not clear whether the dirt particles which are attached to the tip contribute to the contact area or not. However, for two reasons it seems likely that the diameter of the tip is in the order of magnitude of $d_{\max} = 1.48 \mu\text{m}$. Firstly, as stated above, the membrane was imaged before the first Bulge Test or nanoindentation experiment. Moreover, as explained in the experimental section, Bulge Tests were always carried out before the nanoindentation experiment was conducted. Therefore, even a new

6. Results

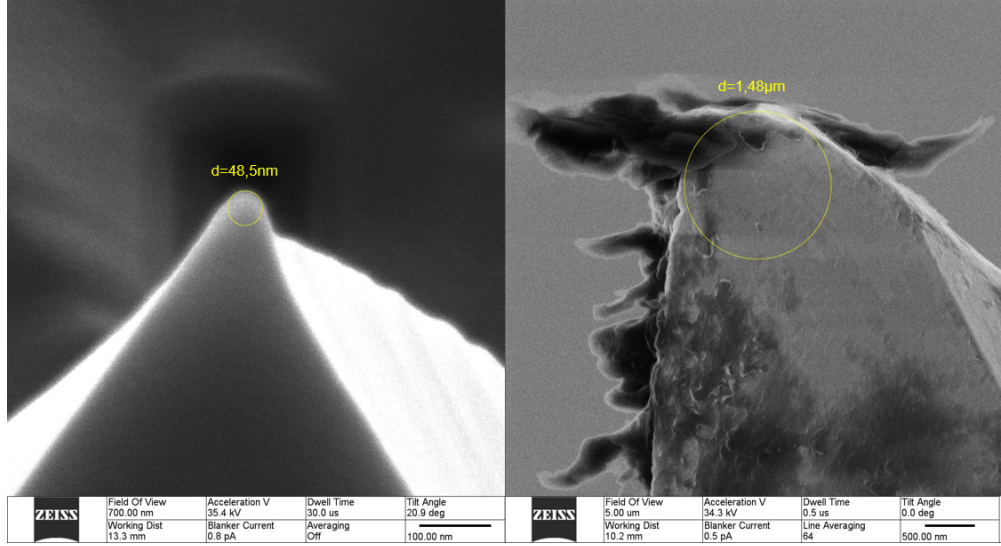


Figure 6.1.: HIM image of a new AFM tip (left) and a used AFM tip after its last experiment (right). Each tip was fit with a sphere in order to estimate its size.

tip was already used significantly when the nanoindentation took place. Secondly, when the tip diameter is small, small changes at its surface lead to a large increase of the tip diameter. In contrast, when the tip diameter is already large, large changes at its surface are needed for a further increase of the tip diameter. Therefore, it can be assumed that the diameter of the sphere increased rapidly when the tip was new, while the increase slowed down with time.

In order to verify the hypothesis $d \approx d_{\max}$, a series of calibration experiments was conducted. The idea of the experiments was to compare the results achieved by nanoindentation to the results achieved by the Bulge Test for different membrane radii. When the membrane radius is small, the ratio $\rho_{\text{in}} = r_{\text{indenter}}/r_{\text{membrane}}$ increases and hence the tip correction factor α_{tip} depends strongly on the indenter radius. On the other hand, for large membrane radii, the dependence of the tip correction factor on the indenter radius

is smaller. Therefore, if both methods agree for large membrane radii, it is shown that they generally yield consistent results. If the results of Bulge Test and nanoindentation additionally agree for small membrane radii as well, the assumed tip size is likely to be true.

6.1.1. Calibration Measurements on CVD Graphene

Due to its highly ordered structure, pristine graphene is perfectly suited for Bulge Test experiments as well as nanoindentation experiments. Moreover, since graphene is electrically conductive, it is ensured that no static electric fields influence the measurement. Therefore, CVD graphene was chosen for the calibration experiments. To this end, seven CVD graphene samples were prepared with different membrane diameters. An overview of the samples is shown in table 6.1.

Table 6.1.: List of CVD graphene samples

Sample number	Number of layers	Membrane diameter [μm]
1	1	4.5
2	1	4.5
3	2	14.1
4	2	16.2
5	3	14.1
6	3	16.3
7	3	16.0

Despite their small membrane diameter, the single layer membranes were very fragile and ruptured quickly. The double and triple layer membranes on the other hand were very stable and endured many experiments.

The results of samples number 1 and 2 are shown in figure 6.2. It can be seen that the results for Bulge Test and nanoindentation show a fairly good

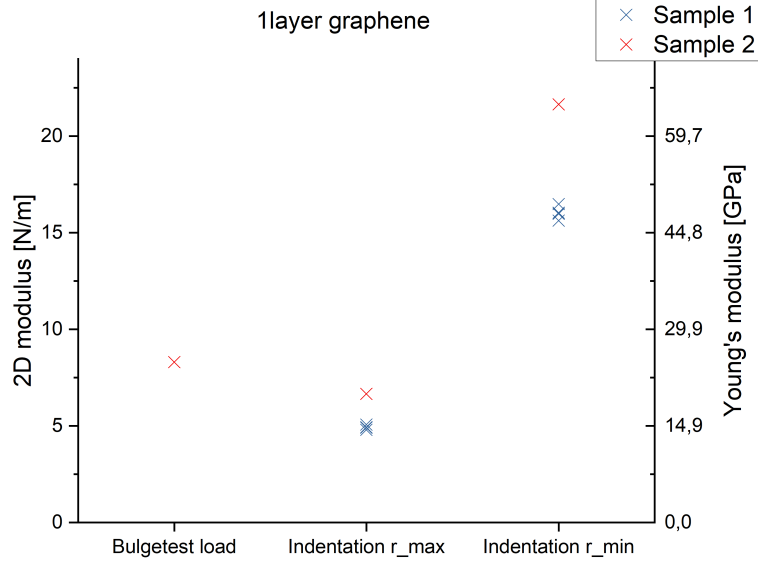


Figure 6.2.: Bulge Test and nanoindentation results for samples number 1 and 2. Each cross represents one experiment. The left scale shows the 2D modulus of the measurement while the right scale shows the corresponding Young's modulus of the measurement assuming a thickness of $t = 0.335$ nm [56]. An assumed indenter radius of $r_{\min} = 24.25$ nm leads to a tip correction factor of $\alpha_{\text{tip}} = 1.16$ while an assumed indenter radius of $r_{\max} = 740$ nm leads to a tip correction factor of $\alpha_{\text{tip}} = 6.96$.

agreement under the assumption that $r_{\text{tip}} = r_{\max} = 740$ nm while the results yielded by $r_{\text{tip}} = r_{\min} = 24.25$ nm are not consistent. The best agreement would be reached for a radius of $r_{\text{tip}} \approx 600$ nm. The total thickness t of the membrane is of course greater than 0.335 nm. However, it is safe to assume that the carbon residues on the membrane do not contribute as much to the total 2D modulus of the graphene-residues composite as the graphene layer does. For the estimation of the Young's modulus of the graphene it is therefore natural to assume the thickness t to be the thickness of the graphene layer, i.e.

$t = 0.335$ nm.

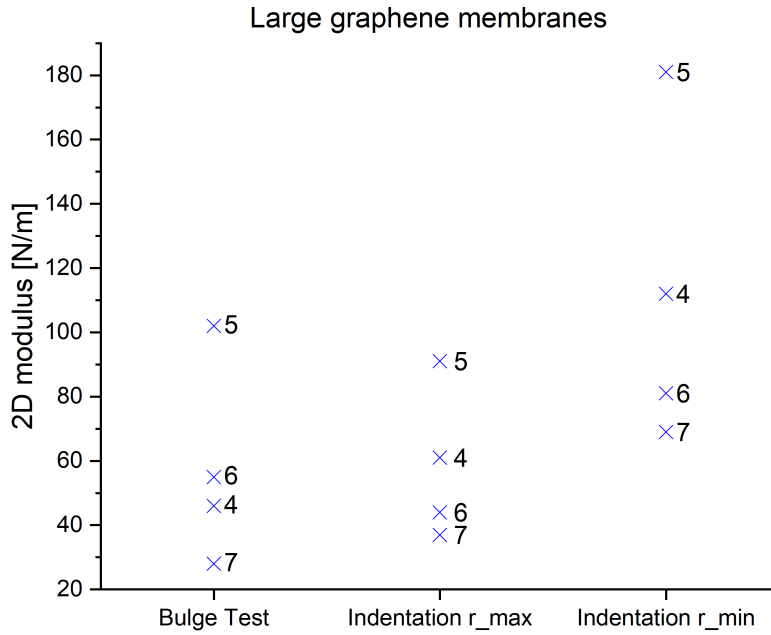


Figure 6.3.: Bulge Test and nanoindentation results for samples number 4 to 7. Each cross represents the averaged results of the sample number it is indicated with. An assumed indenter radius of $r_{\max} = 740$ nm leads to a tip correction factor of $\alpha_{\text{tip}} = 1.97/2.13/1.97/1.99$ for samples number 4 to 7 while an assumed indenter radius of $r_{\min} = 24.25$ nm leads to a tip correction factor of $\alpha_{\text{tip}} = 1.07$ for all samples. Since the thickness of the double and triple layer samples is unknown due to carbon residues between the layers, no corresponding Young's modulus can be calculated for these samples.

The results for the graphene samples with a large membrane diameter, samples number 4 to 7, are shown in figure 6.3. The Bulge Test results for sample number 3 were unrealistically high. This is most likely due to the particles which can be seen in figure 5.4 which hindered the deflection. Therefore, sam-

6. Results

ple number 3 was not considered for the analysis. For samples number 4 to 7, the results for Bulge Test and nanoindentation show a fairly good agreement under the assumption that $r_{\text{tip}} = r_{\text{max}} = 740$ nm while the results yielded by $r_{\text{tip}} = r_{\text{min}} = 24.25$ nm are not consistent. These results show that the approximation $r_{\text{tip}} \approx r_{\text{max}} = 740$ nm is a reasonable assumption for both membrane sizes. Therefore, this value was chosen to be used for the evaluation of the nanoindentation experiments in this work.

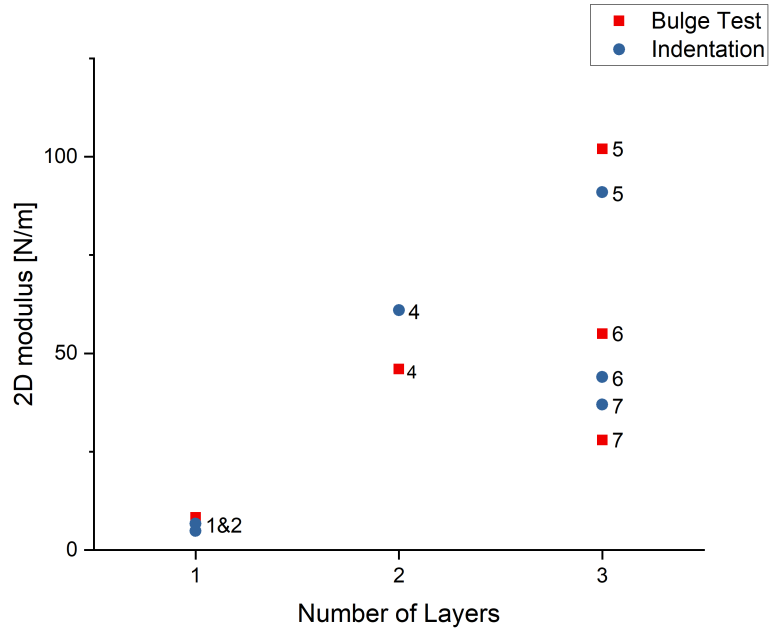


Figure 6.4.: Summary of the averaged results for all CVD graphene samples. The number next to each measured 2D modulus indicates the sample number. The indentation experiments were evaluated using the tip size of $r_{\text{max}} = 740$ nm.

In order to show that there is no systematic error due to this assumption, all results for CVD graphene are summarized in figure 6.4 again by taking the

average of the individual measurements. The results are sorted by the number of layers. It can be seen that under the assumption of $r = r_{max}$ the results for Bulge Test and nanoindentation agree within the range of $\pm 25\%$.

Nevertheless, one has to be aware of the fact that there remains some uncertainty regarding the true contact area between the AFM tip and the membrane during the experiments. A quantification of the uncertainty will be calculated in section 6.4. On the other hand, the fact that a large indenter size was used, reduces the impact of the error due to the sum of the limits approach as it was shown in figure 3.11.

6.1.2. Quantitative Analysis and Discussion

The main purpose of the above experiments was to determine the contact radius of the AFM tip. Nevertheless, a quantitative analysis of the results gives valuable insights into the dependency of the modulus on the preparation method of the sample. The first observation is that the 2D modulus of the single layer graphene is in the range of $E_{2D} = 5 \text{ N/m}$ to $E_{2D} = 8 \text{ N/m}$. The relative uncertainty of 2D modulus is $\Delta E_{2D}/E_{2D} \approx \pm 40\%$ in the case of the Bulge Test and $\Delta E_{2D}/E_{2D} = +110\% / -70\%$ in the case of nanoindentation (see section 6.4). From this result, the 2D modulus for the double layer and triple layer graphene would be expected to be twice respectively three times as high. However, as it is shown in figure 6.4, the 2D modulus of the double layer and triple layer graphene is much higher than 16 N/m respectively 24 N/m. These results are explained by the fact that there are carbon residues¹ from the transfer process trapped between the graphene layers as it was already seen in figure 5.4. These contaminations contribute to the 2D modulus of the membrane. In order to visualize the residues, sample number 5 was imaged by HIM. The image is shown in figure 6.5. It can be seen that the membrane is

¹Besides the carbon residues, a small amount of copper from the copper foil also remains in the sample. However, investigation by Energy-dispersive X-ray spectroscopy (EDX) showed that the amount of copper in the sample is below 1%.

6. Results

very inhomogeneous and hardly distinguishable from the supported graphene. For this reason, the exact value of the measured modulus is only meaningful for the single layer graphene samples.

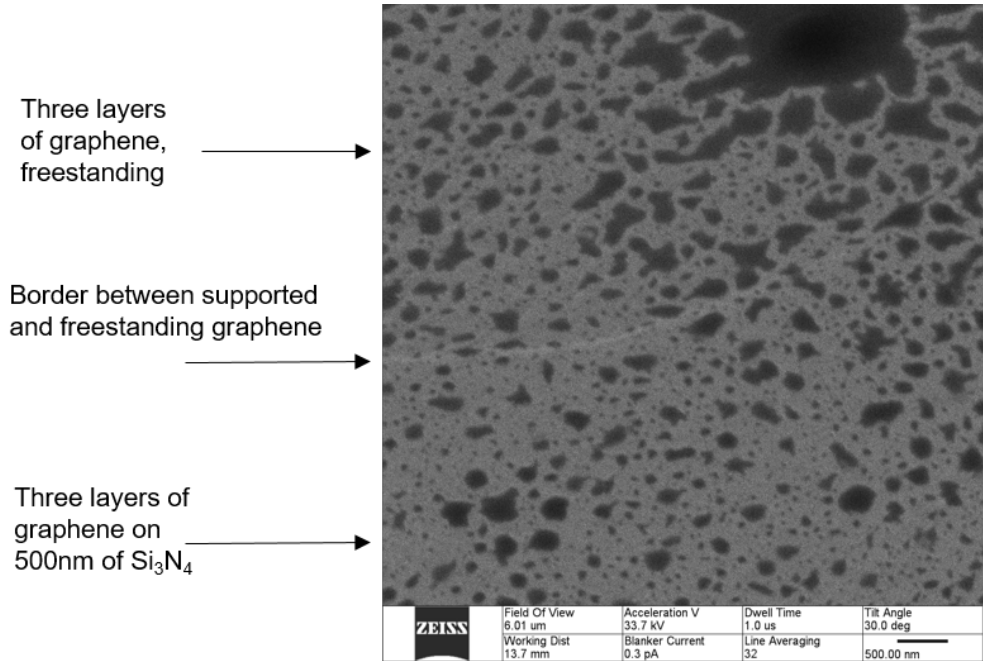


Figure 6.5.: HIM image of CVD graphene sample number 5.

An AFM image of sample number 1 (single layer graphene) is shown in figure 6.6. It can be seen that there are no residues as there were present in the case of multiple layers, for instance shown in figure 5.4 for the case of sample number 3. This is reasonable since both sides of the graphene are in contact with acetone when the PMMA is removed after the transfer. Therefore, organic residues are removed.

The 2D modulus of $E_{2D} = 5$ N/m to $E_{2D} = 8$ N/m is significantly lower than the 2D modulus measured in comparable experiments in the literature

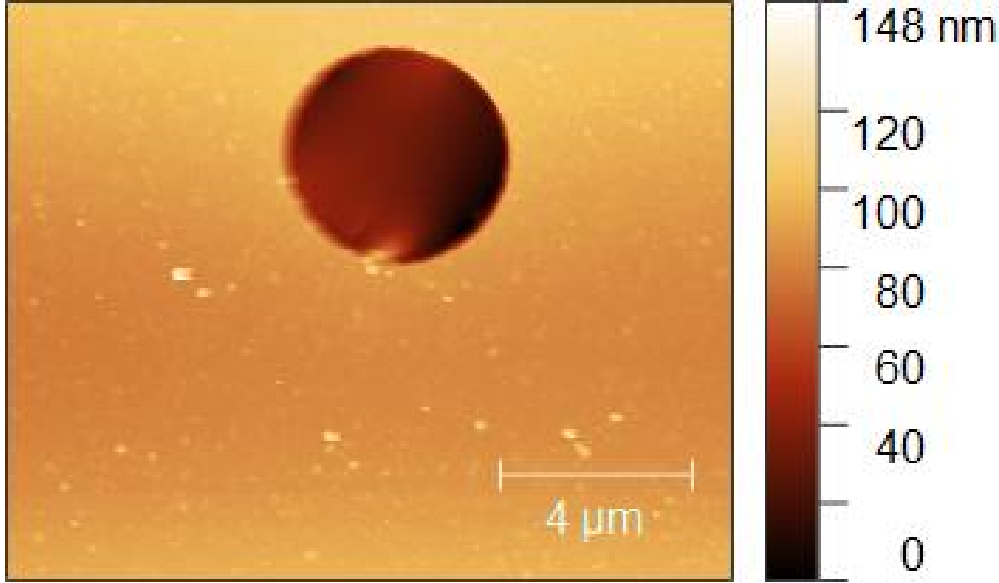


Figure 6.6.: AFM image (tapping mode) of sample number 1.

[79, 80]. In theory, CVD graphene can be as strong as exfoliated graphene [81, 82]. In practice, as shown in the literature, 2D modulus and tensile strength of CVD graphene strongly depend on its preparation and particularly its transfer method. For instance, a transfer with PMMA as a protective layer lead to a 2D modulus of $E_{2D} = 55 \text{ N/m}$ [79]. In that experiment, the PMMA was removed by annealing the sample to 300 °C to 350 °C for 3 to 4 hours. On the other hand, a transfer with poly dimethylsiloxane (PDMS) as a protective layer lead to a 2D modulus of $E_{2D} = 328 \text{ N/m}$ [80]. The PDMS was removed carefully after annealing the sample to 100 °C for 10 minutes. The 2D modulus achieved by this transfer method is almost as much as the 2D modulus of pristine graphene, $E_{2D} = 340 \text{ N/m}$ [34]. It is believed that the high temperatures of up to 350 °C induce small defects which weaken the CVD graphene.

There are two possible explanations for the low 2D modulus measured here.

Firstly, after the transfer, the supporting PMMA is removed by acetone in the critical point dryer. It is not unusual that membranes rupture during this final preparation step, especially thin membranes such as single layer graphene. Therefore, it seems plausible that the critical point drying creates small defects in the membrane which reduce the 2D modulus. A second explanation is that during the preparation process, there are many transfers of the sample between different beakers, for instance from the ammonium persulfate solution to water. The transfers are performed with the help of a SiO₂/Si wafer and carried out very carefully as described in chapter 5. Nevertheless, the transfers may mechanically induce small defects in the graphene sample.

The above results confirm that the preparation method has a large influence on the 2D modulus of a material.

6.2. 2D Modulus and Young's Modulus of Different CNMs

The material of interest in this work are CNMs. Six kinds of CNMs were investigated: 1,1',4',1''-Terphenyl-4-thiol (TPT) from SAMs grown on Au substrates and Ag substrates, 1-Octadecanethiol (ODT), PVBP (Polyvinylbiphenyl)-CNMs, annealed TPT and annealed PVBP-CNMs. In the most cases, nanoindentation leads to the rupture of TPT and ODT membranes. Therefore, only few nanoindentation experiments were conducted on these kinds of CNMs. All other materials were examined by both methods.

6.2.1. TPT

TPT is a CNM which has a high potential for applications. It has been used for rapid water permeation [4] as well as all carbon capacitors [7]. Its structure is amorphous with an average pore size of 0.7 nm [4]. Chemical composition and thickness of TPT were investigated by XPS in [18], see figure 6.7. The

sulfur doublet located at 162.0 eV validates the presence of sulfur gold bonds. The thickness of the TPT-CNM was determined to be 12 Å. The mechanical properties of TPT were already examined in [51]. Here, these results shall be expanded to the question whether TPT-CNMs from SAMs grown on an Ag substrate have a significantly different modulus than TPT-CNMs from SAMs grown on Au.

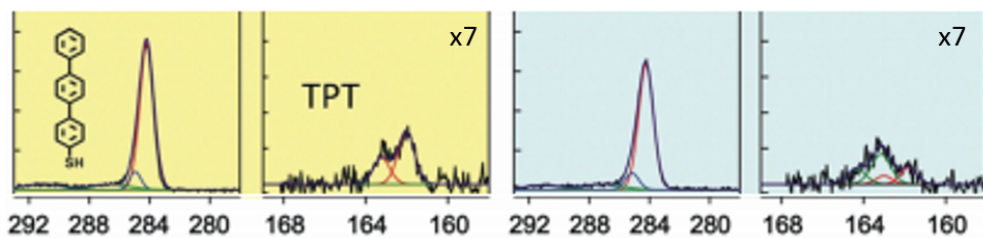


Figure 6.7.: XPS spectra of TPT. The images on the left show the C1s and the S2p peak of the TPT SAM while the images on the right show the carbon C1s and the sulfur S2p peak of the CNM [18].

TPT samples were prepared with a membrane diameter of 15 μm to 16.2 μm . Five membranes were successfully measured by the Bulge Test. The results are shown in figure 6.8. It can be seen that there is no significant difference between the two substrates. The 2D modulus for TPT is in the range of 4.3 N/m to 6.5 N/m which corresponds to a Young's modulus of 3.5 GPa to 5.4 GPa. The uncertainty of each individual measurement is up to $\Delta E/E = \pm 50\%$, see section 6.4. The results found earlier in [51] (supporting information) are a Young's modulus of 7.4 GPa to 8.7 GPa and thus slightly outside the confidence interval. There are many possible explanations for this discrepancy. As it was seen in the case of CVD graphene, small defects may lead to a large decrease of the modulus. Such small defects may for instance be induced by terraces in the Au substrate or mechanically through contact with the silicon wafer during the transfer process. Moreover, small differences

6. Results

in the electron irradiation may also lead to slight differences in the structure of the CNM. In the case of CVD graphene, different methods to proceed the sample transfer in [79] and [80] led to a factor of 7 between the resulting moduli. Therefore, the factor of approximately 1.8 which was found here does not need to be contradictory. However, it should be kept in mind that the 2D modulus of TPT strongly depends on the preparation conditions as well.

Compared to CNMs from other precursor molecules, TPT exhibits a similar but comparably low Young's modulus. A detailed study of CNMs from different precursor molecules was conducted in [51].

It was also tried to characterize TPT by nanoindentation. However, only one membrane was successfully measured while four membranes ruptured during the first force curve. The 2D modulus of the measured membrane was found to be 6.5 N/m which is in a reasonable agreement with the Bulge Test results. Unfortunately, the data of the Bulge Test experiment of the successfully measured membrane did not follow a cubic curve and the membrane ruptured before a second Bulge Test experiment was performed. The rupture of the membranes usually did not occur in one distinct moment. Instead, the membrane partially gave in which resulted in a flawed force curve. Only one rupturing event occurred in a distinct moment. The force curve of the distinct rupture and an exemplary force curve of a partial rupture are shown in figure 6.9. The distinct rupturing event occurred at a force of 102 nN. The maximum stress that the membrane can withstand could in theory be increased with a larger indenter radius. However, since the tip radii used for the present experiments already were very large, there is not much space for a further increase. Moreover, since TPT is insulating, static charges between tip and membrane may damage the sample as well. Therefore, a high risk of a membrane rupture during indentation can hardly be avoided for TPT-CNMs. Nevertheless, if nanoindentation experiments on TPT are desired, the yield of successful experiments can probably be increased by using smaller membrane radii.

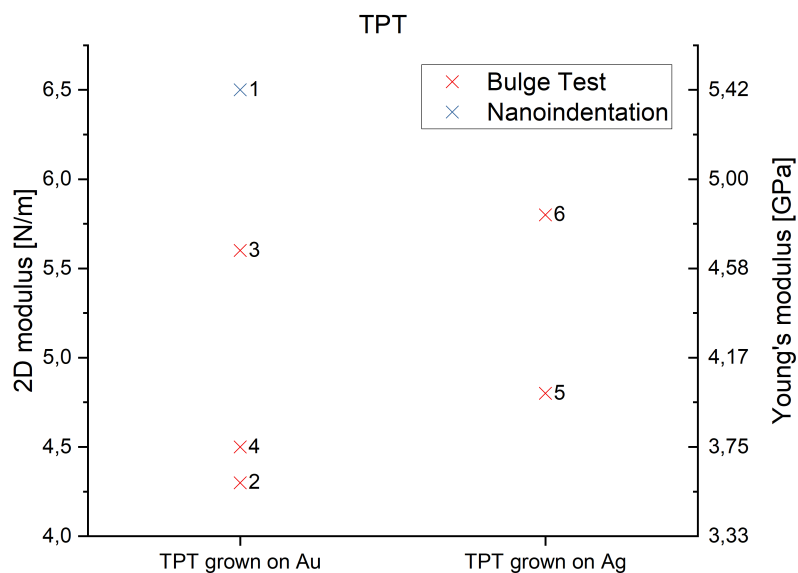


Figure 6.8.: Bulge Test and nanoindentation results for TPT-CNMs from SAMs grown on silver and gold. Each cross represents one membrane indicated with its sample number. Sample number 1 was measured by nanoindentation while samples number 2 to 6 were measured by the Bulge Test. The left scale shows the 2D modulus of the membrane while the right scale shows the corresponding Young's modulus assuming a thickness of $t = 1.2$ nm.

6.2.2. ODT

As stated in chapter 2, the standard precursor molecules for CNMs are aromatic molecules. However, it is also possible to form CNMs from alkanethiols, provided the alkyl chain possesses a sufficient number of carbon atoms [83]. Aliphatic systems do not cross-link as effectively as aromatic systems. Therefore, the destructive processes of the electron irradiation such as decomposition and desorption are more relevant compared to the formation of CNMs from aro-

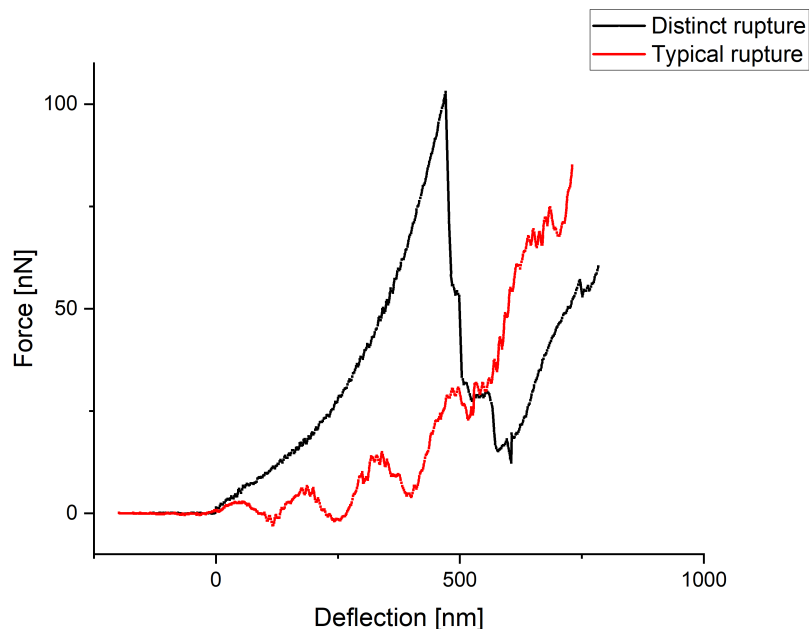


Figure 6.9.: Force vs. deflection curve of two rupturing TPT membranes.

matic precursor molecules. This effect is illustrated by the XPS spectra shown in figure 6.10(i). It can be seen that there is a significant loss of intensity in the carbon signal between SAM and CNM. This loss of intensity is much higher for ODT than in the case of TPT. The higher loss of carbon atoms implies that CNMs from alkanethiols form a less dense network than CNMs from aromatic precursor molecules. This finding is also confirmed by the pore distribution shown in figure 6.10(ii). The average pore size of an ODT-CNMs was found to be 22 Å and thus more than three times as large as the average pore size of a TPT-CNMs. The standard deviation of the pore size was found to be 7 Å. The thickness of ODT-CNMs was also investigated by XPS [83]. It was found to be $t = 11$ Å.

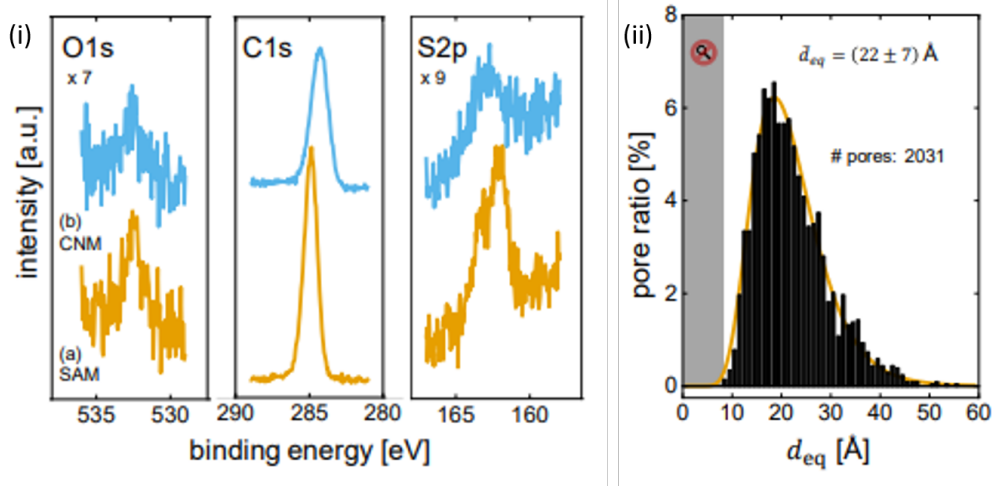


Figure 6.10.: (i) XPS spectra of an ODT-SAM (a) and an ODT-CNM (b) in the regions of oxygen, carbon and sulfur. (ii) Pore distribution of ODT determined by transmission electron microscopy (TEM) [83]. Reproduced with permission.

The loosely connected structure of ODT compared to TPT suggests that CNMs from alkanethiols have a decreased 2D modulus compared to CNMs from aromatic precursor molecules such as TPT. Moreover, the reduced stability leads to a lower yield of intact membranes after the transfer. Therefore, ODT membranes were prepared with a membrane diameter of 6.3 μm to 7.4 μm with one exception of $d = 15.6 \mu\text{m}$ (sample number 3).

8 ODT-CNMs were successfully investigated by the Bulge Test. The results are shown in table 6.2. It can be seen that the distribution of the 2D modulus of the different membranes covers two orders of magnitude. This is a particularly wide distribution. When the pressure applied during the experiment, some membranes exhibited a nitrogen flow through the membrane which led to an upwards deflection of the AFM cantilever when it was in a retracted state from the membrane. In the case of CNMs from aromatic precursor molecules, this would be an unambiguous sign of a defect CNM. However, an investiga-

6. Results

tion in the HIM after the experiment revealed that the ODT-CNMs with a nitrogen stream were still intact and had no defects which were visible in the HIM. This is an indication of large pores. Therefore, it seems likely that the membranes which exhibit a nitrogen stream detectable by the AFM cantilever are slightly more porous than membranes which do not exhibit a detectable nitrogen stream. Given that the pore size distribution shown in figure 6.10(ii) is very wide, the existence of a sufficient or not sufficient nitrogen stream to affect the AFM cantilever may be a purely statistical effect. However, it may also be induced by tiny differences in the intensity or duration of the electron irradiation which lead to a more or less porous membrane.

Table 6.2.: Bulge Test results on ODT

Sample number	2D modulus [N/m] Cycle 1	2D modulus [N/m] Cycle 2	Cantilever deflected by a nitrogen stream
1	1.3	0.7	No (first cycle) Yes (second cycle)
2	0.14		Yes
3	0.71		Yes
4	1.2	2	No
5	3.7	6.4	No
6	0.1		Yes
7	0.07	1.8	Yes
8	2.7	1.2	No

A further indication that the nitrogen stream is caused by large pores is the fact that the membranes with a detectable nitrogen stream exhibit a significantly smaller 2D modulus than the membranes without a detectable nitrogen stream. The distribution of the 2D modulus separated by measurements with or without nitrogen stream are shown in figure 6.11. Since large pores lead to

a reduction in the 2D modulus, it is reasonable to assume that the pores are the cause of both effects.

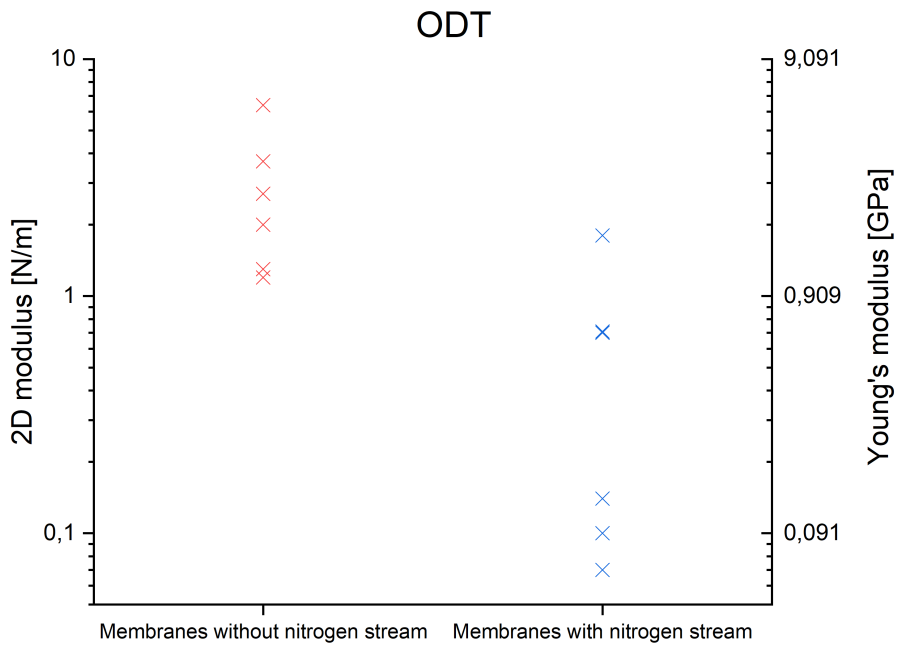


Figure 6.11.: Bulge Test results for ODT. Each cross represents one Bulge Test experiment. The left scale shows the 2D modulus of the membrane while the right scale shows the corresponding Young's modulus assuming a thickness of $t = 1.1$ nm.

A second remarkable feature of the ODT-CNMs is the fact that the 2D modulus results of a membrane showed significant deviations for the two different cycles. This effect is particularly striking in the case of sample number 7. Both cycles were recorded consecutively. The raw data are shown in figure 6.12. The pressure vs. deflection curve of the second cycle shows some noise at

6. Results

higher pressures. This is very common for membranes which exhibit a nitrogen stream. Besides that, both cycles show reasonable data and there is no reason to doubt the correctness of one of the two cycles. A possible explanation for the different behavior of the two cycles is that the ODT membranes have different regions which possess more or less cross links between the individual ODT molecules. Regions with less cross links deflect more than regions with more cross links. However, since all measurements are recorded at the center of the membrane, more or less strongly cross linked regions are required to be located within a maximal distance of 200 nm. Therefore, this effect seems plausible to explain the deviations for samples number 1, 4, 5 and 8. But they are not an explanation for the huge difference shown in figure 6.12.

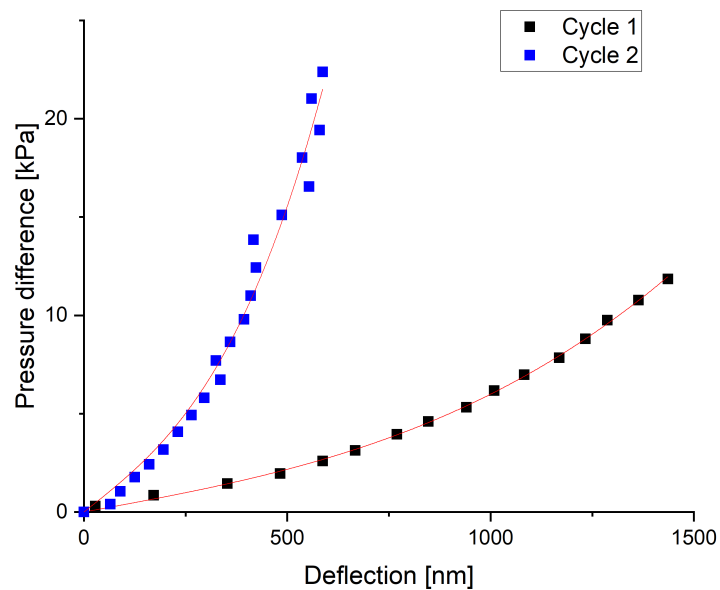


Figure 6.12.: Pressure vs. deflection curves of sample number 7, cycles 1 and 2.

The most likely explanation is that the deflection in the second cycle was hindered by an outer factor. This may for instance be a particle deposited on the membrane. Since ODT is an insulating material, static charges between the tip and the membrane occur. These static charges may support the deposition of a particle which was adhered to the tip. In theory, the deflection during the first cycle could also be facilitated. But the only effect which facilitates the deflection are defects in the membrane. If the first cycle was influenced by defects, the same would be true for the second cycle. Therefore, a hindered deflection in the second cycle is the most likely explanation for the observed deviation.

It was also tried to characterize ODT by nanoindentation. Again, only one membrane, sample number 1, was successfully measured. The resulting force curve is shown in figure 6.13. The resulting 2D modulus is 2.4 N/m which is in a reasonable agreement with the Bulge Test result of the first cycle. As stated in table 6.2, sample number 1 only exhibited a nitrogen flow during the second Bulge Test cycle. Since the indentation experiment was carried out between the two cycles, it seems likely that it induced small defects in the membrane.

Three ODT-CNMs were ruptured by nanoindentation. Therefore, it can be concluded that as for TPT, nanoindentation experiments on ODT-CNMs imply a high risk of rupturing the membrane.

6.2.3. Pyrolyzed TPT

From the point of view of energy minimization, the amorphous structure of CNMs is only a local minimum. Therefore, when provided with energy through annealing, CNMs change their structure and transform into nanocrystalline graphene [23, 84]. Nanocrystalline graphene is a conductive membrane with a graphitic structure and a thickness similar to the original CNM. In an earlier study on BPT-CNMs, it was found that this process, which is called pyrolysis, increases the Young's modulus of BPT from 12 GPa to up to 48 GPa [85] which

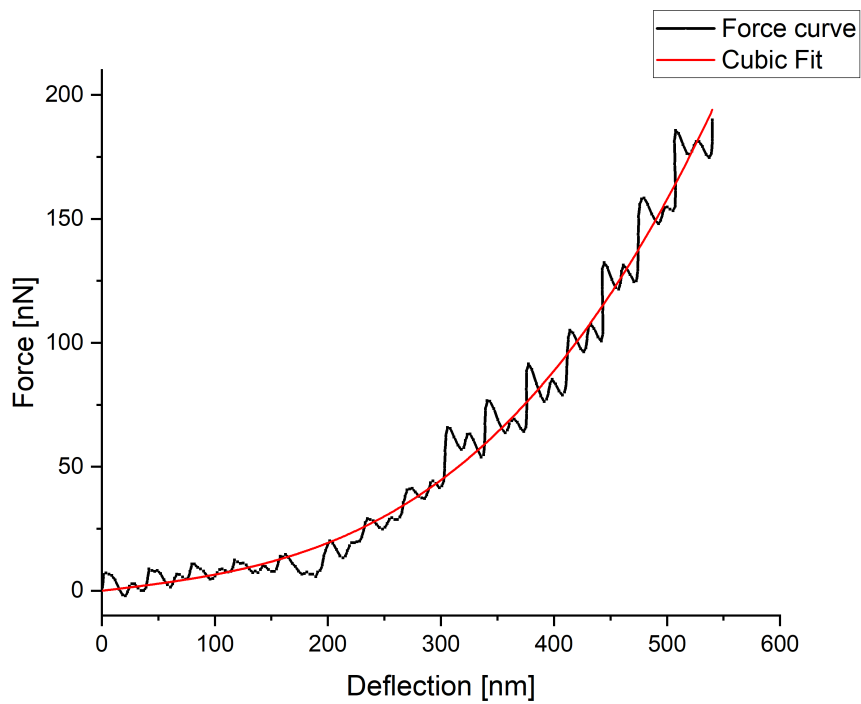


Figure 6.13.: Force curve recorded on ODT sample number 1.

is similar to the Young's modulus of graphite. The annealing temperature required for the conversion was in the range of 800 K to 1000 K.

In order to compare the effect of pyrolysis on TPT to that on BPT, TPT-CNMs were annealed to 700 °C to form nanocrystalline graphene. Unfortunately, only one membrane was successfully measured. The results are shown in figure 6.14. The results are in the range of 21 N/m to 34 N/m. Since there is a slight loss of material during the pyrolysis, the thickness of the resulting membrane was assumed to be $t = 1$ nm. The corresponding Young's modulus is in a reasonable agreement with the results for BPT from [23]. This suggests

that the graphitic structure of the pyrolyzed membrane is independent of the length of the precursor molecule.

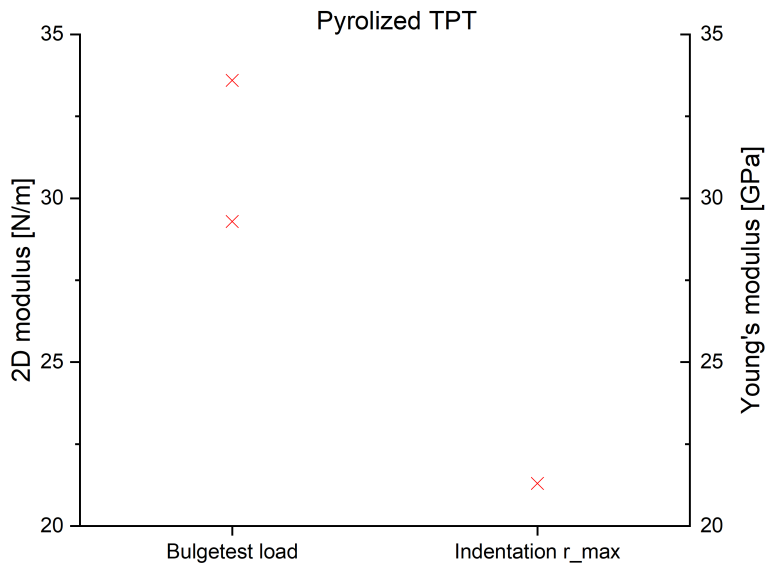


Figure 6.14.: Bulge Test and nanoindentation results for pyrolyzed TPT. Each cross represents one measurement. The left scale shows the 2D modulus of the membrane while the right scale shows the corresponding Young's modulus assuming a thickness of $t = 1$ nm.

6.2.4. PVBP and Pyrolyzed PVBP

PVBP is a new kind of CNM with a thickness of about 10 nm. The increased thickness implies that PVBP-CNMs can be transferred without the stabilizing PMMA layer. This is a great advantage for many applications, for instance the investigation of electric properties [7, 86]. Therefore, it is of interest to

6. Results

investigate the 2D modulus of PVBP as well as pyrolyzed PVBP. To this end, samples were provided by the company CNM Technologies. Two samples were successfully measured. The results are shown in figure 6.15.

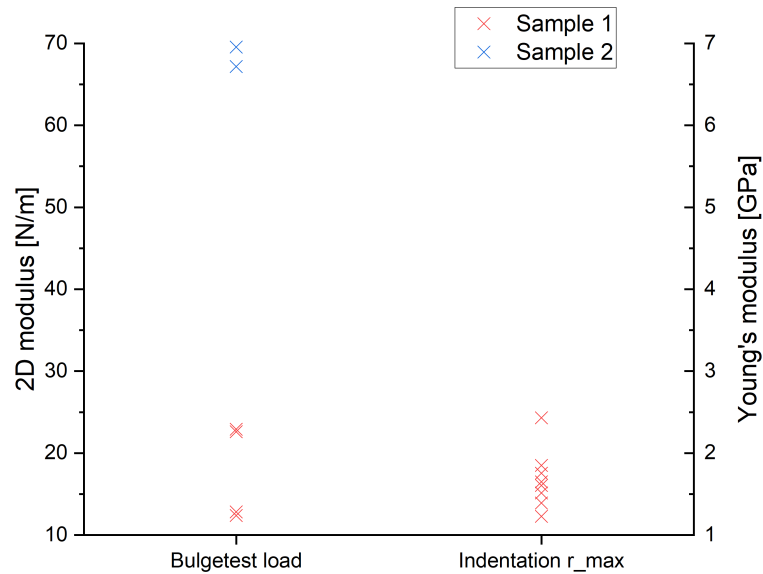


Figure 6.15.: Bulge Test and nanoindentation results for PVBP. Each cross represents one experiment. The left scale shows the 2D modulus of the membrane while the right scale shows the corresponding Young's modulus assuming a thickness of $t = 10$ nm.

It can be seen that both membranes exhibit a significantly different 2D modulus. A possible explanation for the large spread lies in the thickness of PVBP of 10 nm. This makes PVBP thick enough to form cross-links in z-direction as well but still very thin such that the number of cross-links in z-direction may have a relatively large influence on the 2D modulus. Hence, the fact that PVBP is a very thin material but nevertheless consists of multiple atomic lay-

ers gives more options for statistical differences between individual membranes. Moreover, the thickness of each individual membrane may slightly vary which also opens the possibility of statistical differences.

Apart the large range of individual moduli, it can be seen the PVBP has a similar Young's modulus to TPT. This meets the expectation since the atomic structure of PVBP-CNMs and TPT-CNMs are very similar with the main difference that the thickness of the PVBP membrane is much higher. For a more detailed study on PVBP, the measurement of more samples will be required.

In the same way as TPT, PBVP-CNMs can be transformed into a membrane with a graphitic structure through annealing. In order to investigate the effect of pyrolysis on PVBP, PVBP-CNMs were annealed to 1100 °C. Two membranes were successfully measured. The results are shown in figure 6.16.

It can be seen that, as expected, pyrolysis significantly increases the 2D modulus and the Young's modulus of the membrane. The 2D modulus of pyrolyzed PBVP is the highest of the CNMs known to the author. This is due to its graphitic structure combined with the thickness of approximately $t = 8$ nm after the pyrolysis. The Young's modulus of pyrolyzed PBVP is slightly lower than the Young's modulus of pyrolyzed TPT.

Figures 6.15 and 6.16 show that both materials, PVBP and pyrolyzed PVBP are suited for nanoindentation experiments. This is a further advantage of PVBP.

6.3. Initial Tension

The data acquired during Bulge Test and nanoindentation also enable the calculation of the initial tension and 2D initial tension of the membranes. However, while the Young's modulus of a membrane is a property which depends only on the material, the initial tension also depends on the transfer process. In particular, the position of the membrane when it comes in contact with its

6. Results

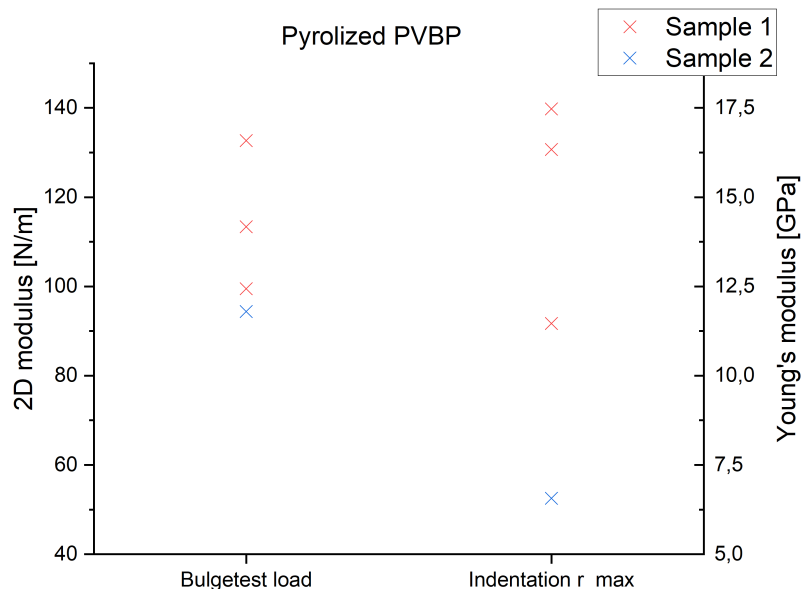


Figure 6.16.: Bulge Test and nanoindentation results for pyrolized PVBP. Each cross represents one experiment. The left scale shows the 2D modulus of the membrane while the right scale shows the corresponding Young's modulus assuming a thickness of $t = 8$ nm.

final substrate as well as heating and cooling steps during the transfer have a large influence on the initial tension. Therefore, two membranes of the same material may have a completely different initial tension. This observation was used in [39] to compare the initial tension determined by the Bulge Test with the initial tension determined by the wrinkles of the membranes in their optical images. However, the optical analysis requires membranes with a lateral size of at least 100 μm . When the membranes are smaller, the value of the initial tension after the transfer process does not have a high significance. Nevertheless, for the sake of completeness, the results obtained for the initial tension

shall be given in the following.

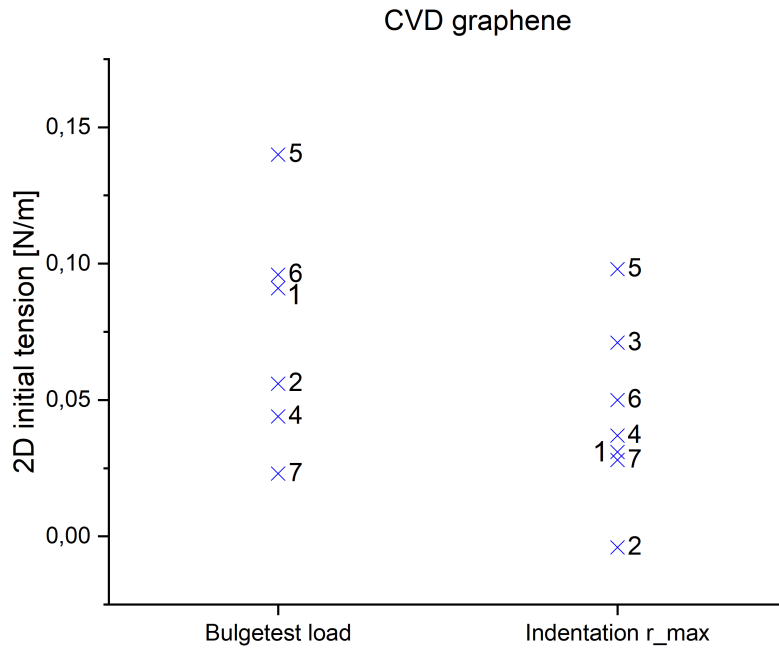


Figure 6.17.: Initial tension of CVD graphene membranes number 1 to 7. Each cross represents the averaged results of the indicated membrane.

The 2D initial tension of graphene membranes number 1 to 7 is shown in figure 6.17. It can be seen that the results obtained by Bulge Test and nanoindentation are only in a very rough agreement. In order to investigate this discrepancy, it is useful to consider the standard deviation of the measurements conducted on each membrane. The results are shown in table 6.3. Since there was only one successful Bulge Test experiment for most membranes, the values obtained for the Bulge Test are not very meaningful. Nevertheless, it

6. Results

can be seen that the standard deviation is very high, i.e. the value obtained as the initial tension is not reproducible. In the case of indentation however, except for membranes number 4 and 7, the standard deviation is reasonable. This is an indication that the initial tension determined by nanoindentation is more reliable than the initial tension determined by the Bulge Test. This might be due to the fact that the determination of the membrane deflection during the indentation is more precise than during the Bulge Test. The force curve used for nanoindentation is taken within few seconds and the deflection height is given by the cantilever height which is automatically determined by the piezo crystal in the AFM. Each deflection value during the Bulge Test has to be determined manually and between each data point there is a time difference of around one minute. Therefore, small changes in the room temperature for example may slightly influence the membrane deflection.

The linear contribution to the force or pressure is the minor term and therefore prone to small deviations in the determined deflection. Hence, the determination of the initial tension is a challenging task, particularly with the Bulge Test.

Table 6.3.: Standard deviation of the initial tension of the CVD graphene membranes and the number of experiments for each sample

Sample number	Standard deviation by Bulge Test [N/m]	n	Standard deviation by indentation [N/m]	n
1	/	1	0.002	4
2	/	1	/	1
3	/	0	0.012	10
4	/	1	0.035	6
5	0.056	3	0.008	14
6	0.036	2	0.012	9
7	/	1	0.031	10

A very high standard deviation was also found for the initial tension determined by the Bulge Test for ODT membranes. The 2D initial tension ranges from 0.013 N/m (sample number 2) to 0.068 N/m (sample number 1). Every membrane was measured once or twice and the standard deviation is up to 0.041 N/m (samples number 1 and 5). The 2D initial tension of TPT membranes ranges from 0 (sample number 4) to 0.083 N/m (sample number 5). The initial tension found for pyrolyzed TPT, PVBP and pyrolyzed PVBP is in the same range (between 0 and 0.066 N/m).

In the case that further investigations on the initial tension are desired, it shall be recommended to utilize the nanoindentation method if possible. However, it shall be stressed again that the initial tension is not primarily a material property. Thus, the value of the initial tension after the transfer process does not have a high significance and it is not possible to compare these results to the results obtained in other experiments.

6.4. Uncertainty Estimation

6.4.1. Bulge Test

The determination of the 2D modulus and the Young's modulus of a membrane through the Bulge Test is subjected to systematic errors as well as statistic errors. The systematic error in the determination of the 2D modulus and the Young's modulus by the Bulge Test is composed of two contributions: The uncertainty in the theoretical description as well as the uncertainty in the Poisson's ratio ν . As stated in equation (5.3), the 2D modulus was calculated by

$$E_{2D} = \frac{k_2 r^4}{K(\nu)}. \quad (6.1)$$

For a given value of the Poisson's ratio ν , the error of $K(\nu)$ is the error in the

6. Results

theoretical description. It was already determined to be $\Delta K(\nu)_{\text{theory}}/K(\nu) = +4\% / -2.1\%$ in chapter 3. However, for both CNMs and graphene, there is also an uncertainty in the exact value of ν . For both materials, a relative uncertainty in the Poisson's ratio of $\Delta\nu/\nu = 20\%$ is assumed. This leads to an error of $\Delta K(\nu)/K(\nu) \approx 10\%$ in the case of CNMs and $\Delta K(\nu)/K(\nu) \approx 1.5\%$ in the case of graphene.

The error of the membrane radius is assumed to be $\Delta r \approx 0.1 \mu\text{m}$. The relative error depends on the membrane size. For the smallest membrane radii of $r = 2.25 \mu\text{m}$, the relative error amounts $\Delta r/r \approx 4.4\%$.

The error of the fitting constant k_2 is composed of the uncertainties of the height determination by the AFM, the error of the pressure determination by the pressure transducer and the uncertainty of the fitting. These errors sum up to an uncertainty of $\Delta k_2/k_2 \approx 15\%$ [76].

Besides these systematic errors, there is also a random error in the response of the membrane to the pressure. This error is due to the fact that a membrane may exhibit a significantly different pressure vs. deflection curve in different measurement cycles. These differences may be due to slight changes in the membrane structure during the previous measurement, small particles on the membrane or different ambient conditions. The error due to the uncertain response of the membrane also contributes to the error of the fitting constant k_2 . The results of the 2D modulus of the same membrane measured on two different days can vary up to 30%, in rare cases even more. Therefore, it is assumed that $\Delta k_{2,\text{ambient}}/k_2 \approx 30\%$. All errors are summarized in table 6.4.

All of the errors listed in table 6.4 are independent. The resulting relative error $\Delta E_{2\text{D}}$ is individual for each membrane due to the different membrane radii and the differences between CNMs and graphene. It was calculated as

$$\Delta E_{2\text{D}} = \sqrt{(\Delta K(v))^2 + (\Delta K(\nu)_{\text{theory}})^2 + (4\Delta r/r)^2 + (\Delta k_2)^2 + (\Delta k_{2,\text{ambient}})^2}. \quad (6.2)$$

Table 6.4.: Uncertainties in the determination of the 2D modulus by the Bulge Test

Error component	Error description	Error estimation
$K(\nu)_{\text{theory}}$	Uncertainty in the theoretical description	+4% / - 2.1%
Poisson's ratio ν	Uncertainty in the value of the Poisson's ratio	20%
Radius r	Uncertainty in the membrane radius	0.1 μm
k_2	Uncertainty in the determination of height and pressure	15%
$k_{2,\text{ambient}}$	Deviations in the membrane response due to ambient conditions	30%

Depending on the membrane, the uncertainty ranges from $\Delta E_{2D}/E_{2D} \approx 34\%$ to $\Delta E_{2D}/E_{2D} \approx 38\%$. A detailed overview of ΔE_{2D} for each type of membrane is given in table 6.6 at the end of this section.

The uncertainty of the Young's modulus is composed of the uncertainty of the 2D modulus and the uncertainty of the membrane thickness Δt . It is estimated to be $\Delta t = 10\%$. Additionally to the membrane itself, the carbon residues on top of the membrane also contribute to the pressure required to deflect the membrane. Since, in the case of single layer membranes, their contribution is assumed to be much smaller than the contribution of the membrane, it was neglected in the calculation of the Young's modulus. This leads to an overestimation of the Young's modulus. Therefore, the error done by neglecting the residues is assumed to be $\Delta E_{\text{residues}}/E = 0 / -20\%$. Due to the asymmetry of $\Delta E_{\text{residues}}$, the total error of ΔE has to be estimated. An uncertainty of up to $\Delta E/E = +40\% / -50\%$ seems reasonable. A detailed overview of ΔE is also given in table 6.6 at the end of this section.

6.4.2. Nanoindentation

In the same way as for the Bulge Test, the nanoindentation experiment is subjected to systematic as well as statistic errors. According to equation (5.6), the 2D modulus was calculated as

$$E_{2D} = \frac{k_2 r^2}{\alpha_{\text{tip}} \alpha(\nu)} = \frac{k_2 r^2 \left(1 - (r_{\text{indenter}}/r)^{2/3}\right)^3}{\alpha(\nu)}. \quad (6.3)$$

The error in the theoretic description of the nanoindentation experiment was already calculated to be $\Delta F(h)/F(h) = +5\% / -25\%$ in chapter 3. An underestimation of the required force leads to an overestimation in the calculated 2D modulus and vice versa. Therefore, the relative error of E_{2D} due to the theoretic description is $+33\% / -5\%$.

The uncertainty in the value of the Poisson's ratio is again $\Delta\nu/\nu = 20\%$. This leads to an error of $\Delta\alpha(\nu)/\alpha(\nu) \approx 6\%$ in the case of CNMs and $\Delta\alpha(\nu)/\alpha(\nu) \approx 2\%$ in the case of graphene.

The error of the membrane radius is again assumed to be $\Delta r \approx 0.1 \mu\text{m}$. The error of the fitting constant k_2 is composed of the uncertainties in the determination of height and cantilever deflection by the AFM and the uncertainty of the fitting. These errors are again assumed to sum up to an uncertainty of $\Delta k_2/k - 2 \approx 15\%$.

There is a large uncertainty concerning the radius of the indenter. From the calibration experiments it was assumed that $r_{\text{indenter}} = 740 \text{ nm}$. However, when a new cantilever is used, the radius of the indenter might be significantly lower. Comparison of the results from Bulge Test and nanoindentation showed that the assumption $r_{\text{indenter}} = r_{\text{max}}$ yields a good agreement for new cantilevers as well as for used cantilevers. Only for the pyrolyzed TPT sample, where a new cantilever was used, there was a significant deviation between the two methods. This deviation might be explained by an overestimation of the tip radius. Therefore, the author estimates the indenter radius to lie in the range

$300 \text{ nm} \leq r_{\text{indenter}} \leq 1 \text{ }\mu\text{m}$.

For the large membranes with a diameter of $d \approx 16 \text{ }\mu\text{m}$, which were mostly used for the indentation experiments, the uncertainty in the indenter radius leads to an error of the tip correction factor $\Delta\alpha_{\text{tip}}/\alpha_{\text{tip}} \approx +19\%/-28\%$. Hence, the error of $E_{2\text{D}}$ due to the uncertainty in the indenter radius is $+39\%/-16\%$. For smaller membranes, the error becomes very large, for instance $+97\%/-65\%$ in the case of $d = 4.5 \text{ }\mu\text{m}$.

In the same way as for the Bulge Test, there is also a random error in the nanoindentation caused by the response of the membrane to the applied force. This uncertainty contributes again to the error in the fitting constant k_2 and is assumed to be $\Delta k_{2,\text{ambient}}/k_2 \approx 30\%$. All errors are summarized in table 6.5.

Table 6.5.: Uncertainties in the determination of the 2D modulus by nanoindentation

Error component	Error description	Error estimation
$\Delta E_{2\text{D, theory}}$	Uncertainty in the theoretical description	$+33\%/-5\%$
Poisson's ratio ν	Uncertainty in the value of the Poisson's ratio	20%
Radius r	Uncertainty in the membrane radius	0.1 μm
k_2	Uncertainty in the determination of height and pressure	15%
r_{indenter}	Uncertainty of the indenter radius	$300 \text{ nm} \leq r_{\text{indenter}} \leq 1 \text{ }\mu\text{m}$
$k_{2,\text{ambient}}$	Deviations in the membrane response due to ambient conditions	30%

In the case of nanoindentation, the errors are not independent since the error in the theoretic description and the uncertainty due to the indenter radius both

depend on the membrane size. Thus, the resulting relative error ΔE_{2D} has to be estimated. Since most of the occurring uncertainties in the nanoindentation experiment are independent, a quadratic addition of the errors is still useful in order to get a rough idea of the total error. To this end, the upper limit of the total confidence interval was approximated by using the upper limits of the confidence intervals in the formula

$$\begin{aligned} \Delta E_{2D} = & ((\Delta E_{2D, \text{theory}})^2 + (\Delta\alpha(\nu))^2 + (2\Delta r/r)^2 \\ & + (\Delta(1/\alpha_{\text{tip}}))^2 + (\Delta k_2)^2 + (\Delta k_{2, \text{ambient}})^2)^{1/2}. \end{aligned} \quad (6.4)$$

In order to estimate the accuracy of this approximation, it has to be remembered that the error in the theoretic description is relatively large for small values of ρ_{textin} and relatively small for large values of ρ_{textin} while the error in the estimation of the tip correction factor α_{tip} is large for a large values of ρ_{textin} and relatively small for small values of ρ_{textin} . Therefore, equation (6.4) leads to a slight overestimation of the error ΔE_{2D} . Thus, for the purpose of being on the safe side, the uncertainty of ΔE_{2D} was estimated by rounding up the result of equation (6.4). The lower limit of the confidence interval was calculated in the same way. The uncertainty of the Young's modulus was approximated in the same way as for the Bulge Test.

The resulting relative error ΔE_{2D} and ΔE for each type of membrane is given in table 6.6. It can be seen that the Bulge Test is significantly more precise than the nanoindentation experiment. The uncertainty in the Bulge Test is similar to previous works [76].

6.5. Summary of all Materials

In this chapter, CVD graphene and five kinds of CNMs were investigated. The graphene samples were mainly used for an indirect determination of the radius

Table 6.6.: Overview of all uncertainties

Samples	ΔE_{2D}	ΔE_{2D}	ΔE	ΔE
	Bulge Test	Indentation	Bulge Test	Indentation
Graphene 1,2	$\pm 38\%$	+110%/–70%	+40%/–50%	+110%–75%/
Graphene 3-7	$\pm 34\%$	+50%/–45%	+35%/–45%	$\pm 50\%$
TPT	$\pm 36\%$	+50%/–45%	+35%/–45%	$\pm 50\%$
ODT 3	$\pm 36\%$	-	+35%/–45%	-
ODT 1,2,4-7	$\pm 37\%$	+70%/–60%	+40%/–50%	$\pm 70\%$
Pyrolized TPT	$\pm 34\%$	+50%/–45%	+35%/–45%	$\pm 50\%$
PVBP	$\pm 36\%$	+50%/–45%	+35%/–45%	$\pm 50\%$
Pyrolized PVBP	$\pm 34\%$	+50%/–45%	+35%/–45%	$\pm 50\%$

of the AFM tip. Due to small defects induced during the transfer process, the graphene samples exhibited a significantly smaller 2D modulus than CVD graphene studied in comparable experiments in the literature [79, 80].

The examination of TPT showed that the modulus of TPT from SAMs grown on a silver substrate exhibits no noticeable difference compared to the well known TPT-CNMs from SAMs grown on a gold substrate. The Young's modulus was found to be approximately 50% smaller than in previous experiments [51] which is a significant deviation but not uncommon in the determination of the 2D modulus and Young's modulus.

Four new kinds of CNMs (ODT, pyrolized TPT, PVBP and pyrolized PVBP)

6. Results

were examined. A summary of the average 2D modulus and Young's modulus of all materials is given in table 6.7. The relative uncertainty is an estimation based on table 6.6 and the following observation: When different samples are in a good agreement, the measurement of multiple samples reduces the statistical errors and hence increases the accuracy. Therefore, the uncertainty is slightly smaller than average uncertainty of an individual membrane and method. On the other hand, if there is a significant deviation between different samples, the uncertainty of the average modulus of the material is larger than the uncertainty of the individual membranes due to an additional statistical influence. This applies to PVBP, where the thickness of the membrane is less reproducible than in the case of CNMs based on monolayers. ODT represents the extreme case of very large membrane to membrane deviations. In this case, no confidence interval can be given. Instead, a range of moduli is stated. A graphical summary of the Young's modulus is given in figure 6.18.

Table 6.7.: Summary of the 2D modulus and Young's modulus of the examined materials

Material	2D modulus [N/m]	Young's modulus [GPa]	Relative uncertainty
CVD graphene (after transfer)	6.6	19.8	+60%/ - 50%
TPT	5.3	4.4	$\pm 40\%$
ODT	0.07-6.4	0.06-5.8	/
Pyrolized TPT	28	28	$\pm 40\%$
PVBP	43	4.3	+100%/ - 60%
Pyrolized PVBP	106	13.3	$\pm 40\%$

All measured CNMs exhibit a Young's modulus which lies in the typical range for polymers [87]. After pyrolysis however, the Young's modulus becomes similar to the Young's modulus of graphite.

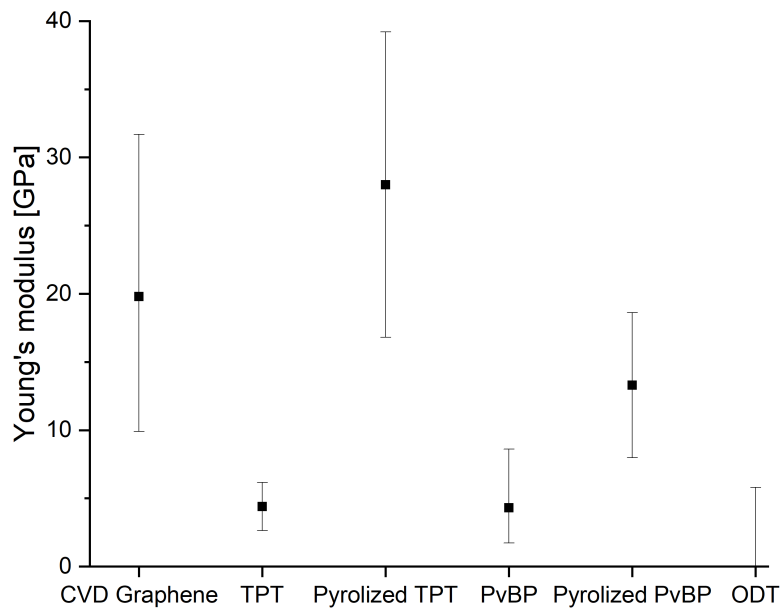


Figure 6.18.: Summary of the Young's modulus of the examined materials.

7. Conclusions of the Thesis

In the theoretical part of this work, a mathematical description of Bulge Test and nanoindentation was given. A pressure-deflection relationship and a force-deflection relationship were derived which describe the experiments as precisely as possible while at same time allowing a practicable data analysis. The accuracy of both formulas was estimated. In the case of the Bulge Test, the sum of the limits formula was shown to be significantly more precise than Beams's formula which is the most frequently used formula in the literature. Furthermore, it was shown that the error done by superposing the small deflection limit and the large deflection limit is very small while the error induced by the other required assumptions is more relevant. In the case of nanoindentation, it was shown that the tip correction factor α_{tip} needs to be considered for an exact description of the experiment. Moreover, an estimation of α_{tip} was given which is well suited for the evaluation of nanoindentation experiments. These findings are essential for the correct data analysis of Bulge Test and nanoindentation experiments.

In the experimental part of this work, it was demonstrated how Bulge Test and nanoindentation can be executed consecutively. The Bulge Test was found to be a reliable method which is suited for any kind of membrane. Nanoindentation was found to be suited for graphene and pyrolyzed samples as well as for PVBP while nanoindentation on TPT and ODT membranes entailed a high risk of rupturing the membrane. The analysis of nanoindentation experiments requires the knowledge of the radius of the AFM tip. The radius was

estimated by a combination of two methods. Firstly, a new cantilever and a used cantilever were imaged in the HIM. Secondly, the results of Bulge Test and nanoindentation were compared for different tip correction factors and different membrane sizes. With this method, a very high tip radius of $r_{\text{indenter}} = 740$ nm was determined. Due to the uncertainty of the indenter radius, the uncertainty of the 2D modulus determined by nanoindentation was found to be higher than the uncertainty of the 2D modulus determined by the Bulge Test. Nevertheless, the results of the nanoindentation experiment are a valuable contribution to the determination of the 2D modulus and Young's modulus. If more work with the nanoindentation method is desired, a detailed study on the tip radius during the experiment seems useful.

With these two methods, five different kinds of CNMs were examined. The 2D modulus of TPT was determined to lie in the range of $E_{2D} = 4.3$ N/m to $E_{2D} = 6.5$ N/m which corresponds to a Young's modulus of 3.5 GPa to 5.4 GPa. TPT-CNMs from SAMs grown on a gold substrate and TPT-CNMs from SAMs grown on a silver substrate showed no difference.

The 2D modulus of ODT-CNMs was shown to have a very broad distribution; it lies in the range of $E_{2D} = 0.07$ N/m to $E_{2D} = 6.4$ N/m which corresponds to a Young's modulus of 0.06 GPa to 5.8 GPa. The reason for this wide range is believed to be the wide distributions of pores with a pore size of up to 60 Å. The ODT-CNMs with a high 2D modulus seem to be less porous than the ODT-CNMs with a low 2D modulus since the latter allowed a significant nitrogen stream through the membrane when subjected to a pressure difference.

A new material called PVBP was investigated which is a CNM with a thickness of approximately 10 nm. It was shown that the 2D modulus of PVBP lies in the range of $E_{2D} = 12$ N/m to $E_{2D} = 70$ N/m. This increase in the 2D modulus of PVBP compared to TPT reflects the higher thickness of PVBP. The Young's modulus of PVBP is 1.2 GPa to 7 GPa and thus very similar to TPT. For a more detailed study on PVBP, the measurement of more samples

is necessary.

Pyrolysis was shown to increase the 2D modulus of the membrane by a factor of approximately 5 to 10. This increase applied to TPT as well as PVBP.

2D materials are still rather new and the understanding of their properties as well as their molecular structure is still in the process. The elastic properties of the membranes studied in the present thesis are one element in the big picture of the properties of these materials. The knowledge of the 2D modulus and the Young's modulus of these membranes will hopefully contribute to a fundamental understanding of the materials and also help in applying them in new technologies.

8. Bibliography

- [1] Novoselov, K. S., Geim, A. K., Morozov, S. V., Jiang, D., Zhang, Y., Dubonos, S. V., Grigorieva, I. V. & Firsov, A. A. Electric field effect in atomically thin carbon films. *science* **306**, 666–669. doi:10.1126/science.1102896 (2004).
- [2] Zhang, K., Feng, Y., Wang, F., Yang, Z. & Wang, J. Two dimensional hexagonal boron nitride (2D-hBN): synthesis, properties and applications. *Journal of Materials Chemistry C* **5**, 11992–12022. doi:https://doi.org/10.1039/C7TC04300G (2017).
- [3] Turchanin, A. & Götzhäuser, A. Carbon nanomembranes. *Advanced Materials* **28**, 6075–6103. doi:https://doi.org/10.1002/adma.201506058 (2016).
- [4] Yang, Y., Dementyev, P., Biere, N., Emmrich, D., Stohmann, P., Korzetz, R., Zhang, X., Beyer, A., Koch, S., Anselmetti, D., *et al.* Rapid water permeation through carbon nanomembranes with sub-nanometer channels. *ACS nano* **12**, 4695–4701 (2018).
- [5] Aghigh, A., Alizadeh, V., Wong, H. Y., Islam, M. S., Amin, N. & Zaman, M. Recent advances in utilization of graphene for filtration and desalination of water: a review. *Desalination* **365**, 389–397 (2015).
- [6] Chen, J., Li, C. & Shi, G. Graphene materials for electrochemical capacitors. *The journal of physical chemistry letters* **4**, 1244–1253 (2013).
- [7] Zhang, X., Marschewski, E., Penner, P., Weimann, T., Hinze, P., Beyer, A. & Götzhäuser, A. Large-area all-carbon nanocapacitors from graphene and carbon nanomembranes. *ACS nano* **12**, 10301–10309 (2018).

8. Bibliography

- [8] Zhang, X. & Beyer, A. Mechanics of free-standing inorganic and molecular 2D materials. *Nanoscale* **13**, 1443–1484 (2021).
- [9] Chen, K.-S. & Ou, K.-S. *Chapter 17. MEMS Residual Stress Characterization* doi:10.1016/B978-0-323-29965-7.00017-8 (Dec. 2015).
- [10] Espinosa, H., Prorok, B. & Fischer, M. A methodology for determining mechanical properties of freestanding thin films and MEMS materials. *Journal of the Mechanics and Physics of Solids* **51**, 47–67 (2003).
- [11] Hencky, H. Über den Spannungszustand in kreisrunden Platten mit verschwindender Biegesteifigkeit. *Z. Math. Phys.* **63**, 311–317 (1915).
- [12] Hohlfelder, R. J. *Bulge and blister testing of thin films and their interfaces* PhD thesis (Stanford University, Jan. 1999).
- [13] Vella, D. & Davidovitch, B. Indentation metrology of clamped, ultra-thin elastic sheets. *Soft Matter* **13**, 2264–2278 (2017).
- [14] Zhang, B. in *Physical Fundamentals of Nanomaterials* (ed Zhang, B.) 177–210 (William Andrew Publishing, Boston, 2018). 978-0-12-410417-4. doi:<https://doi.org/10.1016/B978-0-12-410417-4.00005-8>. <https://www.sciencedirect.com/science/article/pii/B9780124104174000058>.
- [15] Love, J. C., Estroff, L. A., Kriebel, J. K., Nuzzo, R. G. & Whitesides, G. M. Self-Assembled Monolayers of Thiolates on Metals as a Form of Nanotechnology. *Chemical Reviews* **105**. PMID: 15826011, 1103–1170. doi:10.1021/cr0300789. eprint: <https://doi.org/10.1021/cr0300789>. <https://doi.org/10.1021/cr0300789> (2005).
- [16] Götzhäuser, A., Geyer, W., Stadler, V., Eck, W., Grunze, M., Edinger, K., Weimann, T. & Hinze, P. Nanoscale patterning of self-assembled monolayers with electrons. *Journal of Vacuum Science & Technology B: Microelectronics and Nanometer Structures Processing, Measurement, and Phenomena* **18**, 3414–3418 (2000).

-
- [17] Eck, W., Küller, A., Grunze, M., Völkel, B. & Götzhäuser, A. Freestanding nanosheets from crosslinked biphenyl self-assembled monolayers. *Advanced Materials* **17**, 2583–2587 (2005).
- [18] Angelova, P., Vieker, H., Weber, N.-E., Matei, D., Reimer, O., Meier, I., Kurasch, S., Biskupek, J., Lorbach, D., Wunderlich, K., *et al.* A universal scheme to convert aromatic molecular monolayers into functional carbon nanomembranes. *ACS nano* **7**, 6489–6497 (2013).
- [19] Zheng, Z., Nottbohm, C. T., Turchanin, A., Muzik, H., Beyer, A., Heilemann, M., Sauer, M. & Götzhäuser, A. Janus nanomembranes: a generic platform for chemistry in two dimensions. *Angewandte Chemie International Edition* **49**, 8493–8497 (2010).
- [20] Emmrich, D. *Modifikation von Nanostrukturen mit Helium-Ionen* PhD thesis (Universität Bielefeld, 2020).
- [21] Naberezhnyi, D., Götzhäuser, A. & Dementyev, P. Water-Assisted Permeation of Gases in Carbon Nanomembranes. *The journal of physical chemistry letters* **10**, 5598–5601 (2019).
- [22] Yang, Y., Hillmann, R., Qi, Y., Korzetz, R., Biere, N., Emmrich, D., Westphal, M., Büker, B., Hütten, A., Beyer, A., *et al.* Ultrahigh Ionic Exclusion through Carbon Nanomembranes. *Advanced Materials* **32**, 1907850 (2020).
- [23] Turchanin, A., Weber, D., Bünenfeld, M., Kisielowski, C., Fistul, M. V., Efe-tov, K. B., Weimann, T., Stosch, R., Mayer, J. & Götzhauser, A. Conversion of self-assembled monolayers into nanocrystalline graphene: structure and electric transport. *ACS nano* **5**, 3896–3904 (2011).
- [24] Turchanin, A. & Götzhäuser, A. Carbon nanomembranes from self-assembled monolayers: Functional surfaces without bulk. *Progress in Surface Science* **87**, 108–162 (2012).

8. Bibliography

- [25] Poon, B., Rittel, D. & Ravichandran, G. An analysis of nanoindentation in linearly elastic solids. *International Journal of Solids and Structures* **45**, 6018–6033 (2008).
- [26] Beams, J. W. *Structure and Properties of Thin Films: Proceedings* edited by Neugebauer, C.A. (John Wiley and Sons, New York, 1959).
- [27] Martins, P., Delobelle, P., Malhaire, C., Brida, S. & Barbier, D. Bulge test and AFM point deflection method, two technics for the mechanical characterisation of very low stiffness freestanding films. *The European Physical Journal Applied Physics* **45**, 10501 (2009).
- [28] Malvern, L. E. *Introduction to the Mechanics of a Continuous Medium, Chapter 3 Monograph* (1969).
- [29] McGinty, B. *Continuum Mechanics* online (2021 (accessed May 19, 2021)). <http://www.continuummechanics.org/>.
- [30] *Stress in a continuum* online (2021 (accessed May 19, 2021)). https://commons.wikimedia.org/wiki/File:Stress_in_a_continuum.svg.
- [31] Lakes, R. Foam structures with a negative Poisson's ratio. *Science* **235**, 1038–1041 (1987).
- [32] *Polymer Database* online (2021 (accessed April 6, 2021)). <http://polymerdatabase.com/polymer%20physics/Poisson%20Table.html>.
- [33] *Advanced Mechanical Engineering Solutions* online (2021 (accessed April 6, 2021)). <https://amesweb.info/Materials/Poissons-Ratio-Metals.aspx>.
- [34] Lee, C., Wei, X., Kysar, J. W. & Hone, J. Measurement of the elastic properties and intrinsic strength of monolayer graphene. *science* **321**, 385–388 (2008).
- [35] Föppl, A. *Vorlesungen über technische Mechanik, Band 5* 1. Auflage, 45 (Teubner Verlag, Leipzig, 1907).

-
- [36] Bouzidi, R., Ravaut, Y. & Wielgosz, C. Finite elements for 2D problems of pressurized membranes. *Computers & structures* **81**, 2479–2490 (2003).
- [37] Komaragiri, U., Begley, M. R. & Simmonds, J. G. The Mechanical Response of Freestanding Circular Elastic Films Under Point and Pressure Loads. *Journal of Applied Mechanics* **72**, 203. doi:10.1115/1.1827246 (Jan. 2005).
- [38] Vlassak, J. & Nix, W. A new bulge test technique for the determination of Young's modulus and Poisson's ratio of thin films. *Journal of Materials Research* **7**, 3242–3249. doi:10.1557/JMR.1992.3242 (1992).
- [39] Schlicke, H., Leib, E. W., Petrov, A., Schröder, J. H. & Vossmeier, T. Elastic and Viscoelastic Properties of Cross-Linked Gold Nanoparticles Probed by AFM Bulge Tests. *The Journal of Physical Chemistry C* **118**, 4386–4395. doi:10.1021/jp4091969 (2014).
- [40] Hensel, A., Schröter, C. J., Schlicke, H., Schulz, N., Riekeberg, S., Trieu, H. K., Stierle, A., Noei, H., Weller, H. & Vossmeier, T. Elasticity of cross-linked titania nanocrystal assemblies probed by AFM-bulge tests. *Nanomaterials* **9**, 1230 (2019).
- [41] Messaoud, J., Michaud, J.-F., Certon, D., Camarda, M., Piluso, N., Laurent, C., Barcella, F. & Alquier, D. Investigation of the Young's Modulus and the Residual Stress of 4H-SiC Circular Membranes on 4H-SiC Substrates. *Micromachines* **10**, 801. doi:10.3390/mi10120801 (Nov. 2019).
- [42] Lin, P. *The in-situ measurement of mechanical properties of multi-layer coatings* PhD thesis (Massachusetts Institute of Technology, 1990).
- [43] Small, M. K. & Nix, W. Analysis of the accuracy of the bulge test in determining the mechanical properties of thin films. *J. Mater. Res* **7** (1992).
- [44] Pan, J. Y., Lin, P., Maseeh, F. & Senturia, S. D. *Verification of FEM analysis of load-deflection methods for measuring mechanical properties of thin films in IEEE 4th Technical Digest on Solid-State Sensor and Actuator Workshop* (1990), 70–73.

8. Bibliography

- [45] Senturia, S. D. *Microsystem design* 240–259 (Springer Science & Business Media, 2007).
- [46] Campbell, J. D. On the theory of initially tensioned circular membranes subjected to uniform pressure. *The Quarterly Journal of Mechanics and Applied Mathematics* **9**, 84–93 (1956).
- [47] Fichter, W. B. Some solutions for the large deflections of uniformly loaded circular membranes. *NASA Technical Paper 3658* (1997).
- [48] Koenig, S. P., Boddeti, N. G., Dunn, M. L. & Bunch, J. S. Ultrastrong adhesion of graphene membranes. *Nature nanotechnology* **6**, 543 (2011).
- [49] Sun, P., Yang, Q., Kuang, W., Stebunov, Y., Xiong, W., Yu, J., Nair, R., Katsnelson, M., Yuan, S., Grigorieva, I., *et al.* How permeable is the impermeable graphene? *arXiv preprint arXiv:1912.09220* (2019).
- [50] Timoshenko, S. P. & Woinowsky-Krieger, S. *Theory of plates and shells, Chapter 3* (McGraw-hill, 1959).
- [51] Zhang, X., Neumann, C., Angelova, P., Beyer, A. & Götzhäuser, A. Tailoring the mechanics of ultrathin carbon nanomembranes by molecular design. *Langmuir* **30**, 8221–8227. doi:<https://pubs.acs.org/doi/abs/10.1021/la501961d> (2014).
- [52] Schwerin, E. Über Spannungen und Formänderungen kreisringförmiger Membranen. *ZAMM - Journal of Applied Mathematics and Mechanics / Zeitschrift für Angewandte Mathematik und Mechanik* **9**, 482–483. doi:10.1002/zamm.19290090609. eprint: <https://onlinelibrary.wiley.com/doi/pdf/10.1002/zamm.19290090609>. <https://onlinelibrary.wiley.com/doi/abs/10.1002/zamm.19290090609> (1929).
- [53] Jennings, R. M., Taylor, J. F. & Farris, R. J. Determination of residual stress in coatings by a membrane deflection technique. *The Journal of Adhesion* **49**, 57–74 (1995).

-
- [54] Castellanos-Gomez, A., Singh, V., van der Zant, H. S. & Steele, G. A. Mechanics of freely-suspended ultrathin layered materials. *Annalen der Physik* **527**, 27–44 (2015).
- [55] Calabri, L., Pugno, N., Menozzi, C. & Valeri, S. AFM nanoindentation: tip shape and tip radius of curvature effect on the hardness measurement. *Journal of Physics: Condensed Matter* **20**, 474208 (2008).
- [56] Huang, Y., Wu, J. & Hwang, K.-C. Thickness of graphene and single-wall carbon nanotubes. *Physical review B* **74**, 245413 (2006).
- [57] Shearer, C. J., Slattery, A. D., Stapleton, A. J., Shapter, J. G. & Gibson, C. T. Accurate thickness measurement of graphene. *Nanotechnology* **27**, 125704 (2016).
- [58] Jung, W., Park, J., Yoon, T., Kim, T.-S., Kim, S. & Han, C.-S. Prevention of water permeation by strong adhesion between graphene and SiO₂ substrate. *Small* **10**, 1704–1711 (2014).
- [59] Binnig, G., Gerber, C., Stoll, E., Albrecht, T. & Quate, C. Atomic resolution with atomic force microscope. *EPL (Europhysics Letters)* **3**, 1281 (1987).
- [60] Microscopy, N. A. F. S. *Morita, R. Wiesendanger, and E. Meyer* 2002.
- [61] Haugstad, G. *Atomic force microscopy: understanding basic modes and advanced applications* (John Wiley & Sons, 2012).
- [62] Sheiko, S. & Magonov, S. in *Polymer Science: A Comprehensive Reference, 10 Volume Set* 559–605 (2012).
- [63] Eaton, P. & West, P. *Atomic force microscopy* (Oxford university press, 2010).
- [64] Ward, B., Notte, J. A. & Economou, N. Helium ion microscope: A new tool for nanoscale microscopy and metrology. *Journal of Vacuum Science & Technology B: Microelectronics and Nanometer Structures Processing, Measurement, and Phenomena* **24**, 2871–2874 (2006).

8. Bibliography

- [65] Hill, R., Notte, J. & Ward, B. The ALIS He ion source and its application to high resolution microscopy. *Physics Procedia* **1**, 135–141 (2008).
- [66] Hill, R. & Rahman, F. F. Advances in helium ion microscopy. *Nuclear Instruments and Methods in Physics Research Section A: Accelerators, Spectrometers, Detectors and Associated Equipment* **645**, 96–101 (2011).
- [67] Hall, A. R. In situ thickness assessment during ion milling of a free-standing membrane using transmission helium ion microscopy. *Microscopy and Microanalysis* **19**, 740 (2013).
- [68] Hlawacek, G. & Götzhäuser, A. *Helium ion microscopy* (Springer, 2016).
- [69] Watts, J. F. & Wolstenholme, J. An introduction to surface analysis by XPS and AES (2003).
- [70] Hofmann, S. *Auger- and X-ray photoelectron spectroscopy in materials science: a user-oriented guide* (Springer Science & Business Media, 2012).
- [71] Turchanin, A., Käfer, D., El-Desawy, M., Wöll, C., Witte, G. & Götzhäuser, A. Molecular mechanisms of electron-induced cross-linking in aromatic SAMs. *Langmuir* **25**, 7342–7352 (2009).
- [72] Sader, J. E., Chon, J. W. & Mulvaney, P. Calibration of rectangular atomic force microscope cantilevers. *Review of scientific instruments* **70**, 3967–3969 (1999).
- [73] Dufour, I., Lemaire, E., Caillard, B., Debéda, H., Lucat, C., Heinrich, S. M., Josse, F. & Brand, O. Effect of hydrodynamic force on microcantilever vibrations: Applications to liquid-phase chemical sensing. *Sensors and Actuators B: Chemical* **192**, 664–672 (2014).
- [74] Sader, J. E. Frequency response of cantilever beams immersed in viscous fluids with applications to the atomic force microscope. *Journal of applied physics* **84**, 64–76 (1998).

-
- [75] Sader, J. *Atomic Force Microscope Cantilevers (Calibration method of Sader)* online (2021 (accessed February 1, 2021)). <http://www.ampc.ms.unimelb.edu.au/afm/mathematica.html>.
- [76] Zhang, X. *Mechanical characterization of carbon nanosheets* PhD thesis (Universität Bielefeld, 2010).
- [77] Zhang, X., Beyer, A. & Götzhäuser, A. Mechanical characterization of carbon nanomembranes from self-assembled monolayers. *Beilstein Journal of Nanotechnology* **2**, 826–833 (2011).
- [78] Willunat, A. Herstellung und Charakterisierung von Graphen durch Niederdruck-CVD von Methan auf Kupfer (2012).
- [79] Ruiz-Vargas, C. S., Zhuang, H. L., Huang, P. Y., Van Der Zande, A. M., Garg, S., McEuen, P. L., Muller, D. A., Hennig, R. G. & Park, J. Softened elastic response and unzipping in chemical vapor deposition graphene membranes. *Nano letters* **11**, 2259–2263 (2011).
- [80] Lee, G.-H., Cooper, R. C., An, S. J., Lee, S., Van Der Zande, A., Petrone, N., Hammerberg, A. G., Lee, C., Crawford, B., Oliver, W., *et al.* High-strength chemical-vapor-deposited graphene and grain boundaries. *science* **340**, 1073–1076 (2013).
- [81] Wei, Y., Wu, J., Yin, H., Shi, X., Yang, R. & Dresselhaus, M. The nature of strength enhancement and weakening by pentagon–heptagon defects in graphene. *Nature materials* **11**, 759–763 (2012).
- [82] Grantab, R., Shenoy, V. B. & Ruoff, R. S. Anomalous strength characteristics of tilt grain boundaries in graphene. *Science* **330**, 946–948 (2010).
- [83] Dalpke, R. *Transport Behavior of Tailored Carbon Nanomembranes* PhD thesis (Universität Bielefeld, 2020).
- [84] Turchanin, A. Graphene Growth by Conversion of Aromatic Self-Assembled Monolayers. *Annalen der Physik* **529**, 1700168 (2017).

8. Bibliography

- [85] Turchanin, A., Beyer, A., Nottbohm, C. T., Zhang, X., Stosch, R., Sologubenko, A., Mayer, J., Hinze, P., Weimann, T. & Götzhäuser, A. One nanometer thin carbon nanosheets with tunable conductivity and stiffness. *Advanced Materials* **21**, 1233–1237 (2009).
- [86] Penner, P. *Untersuchung der elektrischen und dielektrischen Eigenschaften von Kohlenstoffnanomembrane und ihre Anwendung in Kohlenstoffnanokondensatoren* PhD thesis (Universität Bielefeld, 2018).
- [87] *The engineering tool box* online (2021 (accessed july 21, 2021)). https://www.engineeringtoolbox.com/young-modulus-d_417.html.

Declaration of Academic Honesty

I hereby declare that I have independently written the present dissertation and that none other than the quoted literature was used.

Bielefeld, September 7, 2021

Florian Paneff

Danksagung

Diese Dissertation ist das Ergebnis meiner Arbeit in der Forschungsgruppe Physik supramolekularer Systeme und Oberflächen an der Fakultät für Physik der Universität Bielefeld. Sie wäre jedoch nicht möglich gewesen ohne die Unterstützung vieler Menschen, bei denen ich mich im Folgenden bedanken möchte.

Zunächst gilt mein Dank Prof. Dr. Armin Gölhäuser dafür, dass er mir die Möglichkeit gab, in seiner Arbeitsgruppe zu promovieren und die Betreuung meiner Arbeit zu übernehmen. Die Besprechungen mit ihm brachten stets neue Ideen zu Tage und waren mir eine große Hilfe und Motivation. Des Weiteren möchte ich Prof. Dr. Jürgen Schnack für die Erstellung des Zweitgutachtens zu dieser Arbeit danken.

Ferner danke ich Dr. André Beyer und Dr. Xianghui Zhang dafür, dass ich an vielen ihrer Projekte mit den unterschiedlichsten Themen mitarbeiten durfte und dafür, dass sie jederzeit für die Diskussion der Daten und weitergehender Ideen offen waren.

Des Weiteren möchte ich Dr. Nikolaus Meyerbröker von der Firma CNM Technologies GmbH, Dr. Raphael Dalpke und Linh Le Hoang dafür danken, dass ich ihre Proben vermessen durfte, sowie Dr. Daniel Emmrich und Michael Westphal für die vielen aufschlussreichen Bilder am Helium-Ionen-Mikroskop.

Ebenfalls gilt mein Dank Professor Dr. Andreas Schönhals und Marcel

8. Bibliography

Gawek von der BAM Berlin für die dielektrischen Messungen und ihre Gastfreundschaft.

Zudem möchte ich Riko Korzetz für die detaillierte Korrektur meiner Arbeit und viele hilfreiche Diskussionen danken, sowie Dr. Paul Penner und Emanuel Marschewski für die vielen Hilfestellungen, die sie mir während der Anfangszeit meiner Arbeit gaben. Der gesamten Arbeitsgruppe D0 danke ich für die angenehme Arbeitsatmosphäre und die wunderschöne Zeit, die ich dort verbringen durfte.

Schließlich gilt mein Dank meinen Freunden und meiner Familie, die mich stets in jeglicher Hinsicht unterstützten, sich Probevorträge von mir anhörten und mir die Motivation und Energie für diese Arbeit gaben.

Euch und Ihnen allen mein herzlicher Dank!

A. Mathematica Source Code for the Bulge Test Theory

(1) Calculation of B_0 in the case of no initial tension.

```
clear[b]
v=0.35
f:=b(1-v)-1/b^2*(3-v)-(5-v)*2/(3*b^5)-(7-v)*13/(18*b^8)-(9-v)*17/(18*b^11)-(11-v)*37/(27*b^14)-(13-v)*1205/(567*b^17)
Plot[f,b,0,10]
x = FindRoot[f,b,1]
```

(2) Calculation of an array of values of B_0 as a function of the initial tension σ_0 . Every parameter is used for one value of the pressure p .

```
clear[b]
clear[y]
v=0.35
sigma=0, 0.005,0.006, 0.007, 0.008,0.009, 0.01,0.011, 0.012,0.013, 0.015,0.017,
0.02, 0.025, 0.03, 0.04, 0.05, 0.06, 0.07, 0.08, 0.09, 0.1, 0.12, 0.14, 0.16, 0.18,
0.2, 0.22, 0.24, 0.26, 0.28, 0.3,0.32,0.34, 0.36, 0.38, 0.4, 0.42, 0.44, 0.46,0.48,0.5,
0.53, 0.56,0.6,0.64,0.68,0.72,0.76,0.8, 0.85, 0.9,0.95,1,1.1, 1.15,1.2, 1.25, 1.3, 1.4,
1.5, 1.6, 1.7, 1.8, 1.9, 2, 2.2, 2.4, 2.6, 2.8, 3, 3.2, 3.4, 3.6, 3.8, 4, 4.3, 4.6, 5, 5.5,
6, 6.5, 7, 7.5, 8, 8.5, 9, 9.5, 10, 11, 12, 13, 14, 15, 16, 17, 18, 19, 20, 22, 24, 26,
28, 30, 32, 36, 40, 50, 60, 80
```

A. Mathematica Source Code for the Bulge Test Theory

```
y={}  
f:=b(1-v)-1/b^2*(3-v)-(5-v)*2/(3*b^5)-(7-v)*13/(18*b^8)-(9-v)*17/(18*b^11)-(11-v)*37/(27*b^14)-(13-v)*1205/(567*b^17)-sigma  
Plot[f,b,0,10]  
For[i=1,i<111,i++,x= FindRoot[Extract[f,i],b,1]; y=Append[y,x]]  
Print[y]
```